Measurement of the Standard Model $Z/\gamma^* \to e^+e^-$ Production Cross Section at $\sqrt{s} = 7$ TeV with the ATLAS Detector

Thesis submitted in accordance with the requirements of the University of Liverpool for the degree of Doctor in Philosophy

by

Sylwia Migas

THE UNIVERSITY *of* LIVERPOOL

Particle Physics Department

July 2013

This thesis is the result of my own work, except where explicit reference is made to the work of others, and has not been submitted for another qualification to this, or any, other university. The research was carried out in the Department of Physics, Faculty of Science and Engineering, and at CERN, Geneva, Switzerland. This thesis does not exceed the word limit for the respective Degree Committee.

Measurement of the Standard Model $Z/\gamma^* \to e^+e^-$ Production Cross Section at $\sqrt{s} = 7$ TeV with the ATLAS Detector

Sylwia Migas

Abstract

At the LHC, the process $Z/\gamma^* \to e^+e^-$ is investigated to test the Standard Model in a completely new kinematic range. This thesis describes Z/γ^* cross section measurements using proton-proton collisions recorded by the ATLAS detector in 2011. The data sample corresponds to an integrated luminosity of 4.64 fb^{-1}. The differential Z/γ^* cross section measurements are performed in the boson rapidity bins, and integrated over three m_Z ranges, covering a region of $46 < m_Z < 150$ $[GeV]$. Overall a good agreement is observed between the results and theoretical predictions based on a recent PDF sets determined by the CTEQ, MSTW, ABM, HERAPDF and NNPDF groups.

Contents

Acknowledgements

I thank the Science and Technology Facilities Council (STFC) for the financial support during this degree.

I would like to express my gratitude to my supervisors Dr. Uta Klein and Dr. Stephen Maxfield for their guidance and patience over the past years. The completion of the thesis would not have been possible without continuous support from Dr. Jan Kretzschmar. His expertise has guided me on numerous occasions.

My biggest thank you goes to my Family, for their endless help and encouragement.

Chapter 1

Introduction

This year marks the 30^{th} anniversary of the first direct Z boson observation made by physicists at the Super Proton Synchrotron at CERN in 1983. For the past three decades properties of this neutral elementary particle were studied in detail by several experiments, including the Tevatron at Fermi National Accelerator Laboratory (US), the Large Electron-Positron Collider (CERN) and the SLAC Linear Collider (US). In the era of the Large Hadron Collider (CERN), the Z boson, together with its electrically charged cousin particle, the W boson, is an important tool for obtaining sensitivity to new physics phenomena. In particular, studies of the inclusive production cross sections of the Z and W bosons constitute a substantial test of the Standard Model of Particle Physics at the highest hadron collider energy accessible so far.

The aim of this thesis is the measurement of inclusive Z boson production cross section in the electron decay channel, using the LHC proton-proton collision data at $\sqrt{s} = 7\ TeV$, collected by the ATLAS Detector in 2011. Several aspects of the study constitutes a complementary cross-check to the latest ATLAS results [1]. The first measurements of this kind were performed with approximately $35 fb^{-1}$ of ATLAS 2010 data and published in [2], with the corresponding support note [3], as well as by the CMS Collaboration with 2010 [4] and 2011 [5] data, and the LHCb Collaboration with $0.94 fb^{-1}$ [6].

This thesis presents the differential cross section measurements as a function of di-electron rapidity η and di-electron invariant mass M_{ee}, in the range from 46 to 150 GeV. The integrated cross section in the fiducial region of the experiment is presented, as well as the result after theoretical extrapolation to the full phase space. The final results are compared to the NNLO QCD predictions, which are calculated using several different sets of parton distribution functions (PDF).

This thesis is organised in ten chapters, where each of the constituents essential for the derivation of the final result is discussed separately. Chapter 2 contains the theoretical outline of the physics relevant for the Z boson production at the LHC, where the Drell-Yan process is introduced, along with the Quark Parton Model (QPM). This is followed by a brief description of the ATLAS detector in Chapter 3 with the emphasis on the detector components most crucial for the Z boson cross section measurement in the electron decay channel, i.e the inner tracking detector and calorimeters. Chapter 4 and Chapter 5 concentrate on the electron trigger, identification and reconstruction in the ATLAS Detector, where the data driven method, central for the estimate of the measurement efficiencies is presented, with an example of the electron trigger efficiency evaluation. Chapter 6 describes data and Monte Carlo generated samples used in analysis, provides a brief specification of the main Monte Carlo events generators, and details the global corrections applied to the MC samples. The event selection procedure is described in Chapter 7. In Chapter 8 the background sources to the process of interest and methods of their determination are described. In particular the data driven method employed to the QCD multijet background evaluation is presented. The summary of results of the $Z/\gamma^* \to e^+e^-$ cross section measurements is included in Chapter 9. An introduction to the methodology for the cross section calculation, details of the systematic uncertainties related to the cross section measurement, and comparison of results with respect to several theoretical predictions calculated at next-to-next-to leading order (NNLO) in QCD, using

various PDF sets, are also contained. The final chapter (Chapter 10) of the thesis provides a brief summary of the work presented.

Chapter 2

Theoretical Overview

This chapter provides a brief overview of the theoretical framework, which describes the fundamental constituents of matter and their interactions, called the *Standard Model*, in the first section. The following parts include some theoretical aspects related to the proton-proton collisions, as well as Z/γ^* production at the Large Hadron Collider with respect to the Drell-Yan Process.

2.1 The Standard Model

The Standard Model (SM) of particle physics constitutes an appropriate description of the elementary particles and three[1] fundamental forces mediated between them. The fundamental particles are spin-half fermions (quarks and leptons), from which all matter is constructed, and the integer spin gauge bosons, which are the force-mediating particles.

There are six quarks and six leptons classified in three generations, where additionally for each of these particles an anti-particle (characterised by the same spin and mass, but opposite values of remaining properties, e.g. electric charge) exists. Six flavours (types) of leptons are distinguished: electron (e), muon (μ), tau (τ) - carrying negative electric charge, and electron neutrino (ν_e), muon neutrino (ν_μ), tau neutrino (ν_τ) - which are electrically neutral. The six flavours

[1]Gravity is not included in the Standard Model.

of quarks are: up (u), charm (c), top (t) - carry electric charge of $+\frac{2}{3}e$, and down (d), strange (s), bottom (b) - electric charge of $-\frac{1}{3}e$, where e is the charge of the proton. Each quark is characterised by an additional degree of freedom, called colour charge, and a quark's colour can take one of three values (charges): red, green, or blue. Both quarks and leptons are spin $\frac{1}{2}$ fermions, which obey Fermi-Dirac statistics.

The gauge bosons are responsible for mediating forces between particles, they have integer spin and they obey Bose-Einstein statistics. The electromagnetic force is mediated by a massless photon (γ). The weak interactions are mediated by the massive, charged W^+, W^- and neutral Z^0 bosons. Finally, massless gluons (g) are the strong force mediators.

Quarks are the only group of elementary particles participating in all three fundamental interactions. The e, μ and τ leptons are subject to electromagnetic and weak interactions, while the neutrinos experience weak force only. An overview of the Standard Model elementary particles is given in Table 2.1.

The Standard Model is a quantum field theory, which successfully describes the theory of the strong interactions between quarks and gluons (i.e. theory of Quantum Chromodynamics, or QCD [7, 8]), the theory of photon mediated electromagnetic interactions of electrically charged particles (i.e. theory of Quantum Electrodynamics, or QED), as well as including a unification of the electromagnetic and weak interactions, as proposed by Sheldon Glashow [9], Abdus Salam [10] and Steven Weinberg [11], in the Electroweak theory. The Standard Model also contains a description of the Higgs mechanism [12, 13, 14], a process in which particles acquire their masses by interaction with the Higgs field.

Despite some limitations, the Standard Model is a favorable theoretical representation, due to an excellent agreement with the experimental measurements, and the recent discovery of a long-sought Higgs boson at the LHC [15, 16, 17], will strengthen its position, as the most comprehensive physics model so far.

The Standard Model Fermions			
	Generation		
Category	1^{st}	2^{nd}	3^{rd}
Leptons	e	μ	τ
	ν_e	ν_μ	ν_τ
Quarks	u	c	t
	d	s	b

The Standard Model Bosons			
	Type of the Force		
Category	Electromagnetic	Weak	Strong
The Gauge Bosons	**Photon** (γ)	$W^{\pm}$, Z^0	**gluon** (g)
The Higgs Bosons	H^0		Origin of Mass

Table 2.1: The Standard Model elementary particles.

2.2 Proton and The Parton Model

In 1969 Richard Feynman proposed the *parton model* [18] to explain observations from collision experiments, where highly energetic electrons were scattered off protons in a liquid hydrogen target. The observed cross-section for a large momentum transfer was greater than anticipated, implying the existence of the proton's internal structure [19, 20].

According to the parton model, a hadron is composed of a number of point-like constituents, named partons, in a reference frame where it has an infinite momentum (i.e. approximation valid at high energies). Assuming the naive approach to the quark parton model, a proton consists of three valence quarks (*uud*). In Quantum Chromodynamics (QCD) the valence quarks can radiate gluons, which are the bosons exchanged to provide the forces that hold the quarks inside the proton. Gluons can radiate gluons and also split into virtual $q\bar{q}$ pairs,

which themselves can radiate other gluons. Therefore, in addition to the three valence quarks, the proton structure contains the sea of quarks and gluons. This is schematically represented in Figure 2.1.

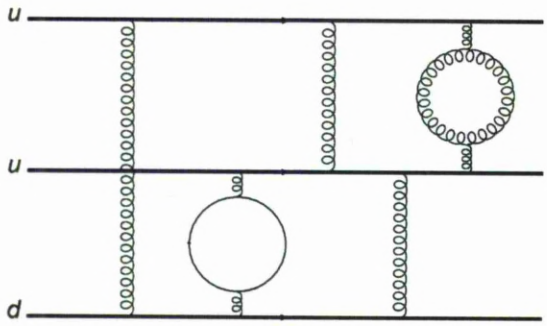

Figure 2.1: Schematic illustration of the interactions between valence quarks of the proton via exchange of the gluons.

2.2.1 The Proton-Proton Collisions

A proton-proton collision at high energies can no longer be approximated as an elastic scattering of two electrically charged objects, as the actual interactions occur between partons contained in the protons.

The two partons (regarded as a free, point-like particles), each from one proton, take part in the interaction, that occasionally[2] involves a large momentum transfer (Q^2). This type of interaction is referred to as a hard scattering process. One possible hard interaction is the annihilation of the incoming partons to produce a resonant state, as a Z^0 boson. The remaining partons, which are not involved in the hard interaction, form the underlying event. They are no longer colour-singlet states and undergo interactions, resulting in an additional hadronic deposits within the detector.

Since the partons are electrically and color charged, they are associated with emissions of gluons[3] and photons (parton showers). The parton can shower before

[2]In most cases the partons are involved in low energy scale interactions.
[3]Emission of gluons dominates in hadronic interactions.

the actual hard scattering process occurs, resulting in the Initial State Radiation (ISR), while the Final State Radiation (FSR) refers to emissions off final state particles. The parton shower evolution is stopped when a low energy scale (usually about 1 GeV) is reached. At this point the colourless hadrons are formed from coloured objects in the process called hadronization. A schematic illustration of a hard scattering process in a proton-proton collision is presented in Figure 2.2.

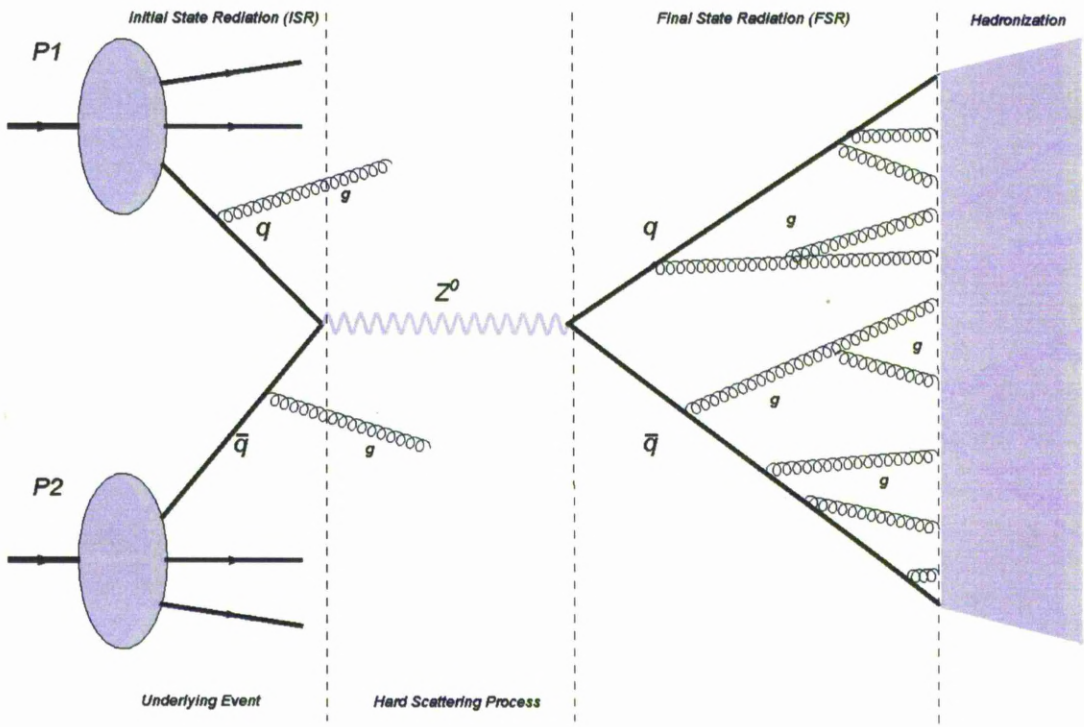

Figure 2.2: Schematic illustration of the hard scattering process in a proton-proton collision. Exemplified is the resonant state involving Z^0 boson with two quarks in the final state. The ISF and FSR are represented by the gluon emissions.

2.2.2 The Parton Distribution Functions

The partonic structure of the proton plays a fundamental role in elementary particle physics, and it is probed in high energy collision experiments. The partons involved in the hard scattering process, come from the incoming protons according to a given probability, which is a function of the proton's momentum

fraction carried by a parton, and the energy scale of the momentum transfer (Q^2) involved, i.e. $f(x_i, Q^2)$. This probability is given by the Parton Distribution Functions (PDFs) [21]. Assuming the proton with a momentum P, and the particular parton i with a momentum p_i, we can define the momentum fraction of the proton carried by a parton, by:

$$x_i = \frac{p_i}{P}, \qquad x_i \in (0, 1); \tag{2.1}$$

where P is determined by the beam energy of the collider.

The sum of the four-vectors of the partons involved in the interaction determines the energy scale of the process, (Q^2), therefore in case of the scattering involving a resonant state:

$$Q^2 = (p_1 + p_2)^2 = M^2 = (p_3 + p_4)^2 = s x_1 x_2, \tag{2.2}$$

where p_1, p_2 denote the four-momenta of incoming partons, and p_3, p_4 the four-momenta of the decay products of the resonant state characterised by the invariant mass M. The center-of-momentum system (cms) energy squared is given by $s = 4P^2$.

The PDFs dependence on Q^2 is successfully described in perturbative QCD (pQCD) by the DGLAP evolution equations [22]. Nevertheless the functional form of the PDFs is not predicted by pQCD, and its determination is performed phenomenologically by a global fit to experimental data. The suitable data are collected in *deep inelastic scattering* (DIS) experiments, including the fixed target experiments, and the electron-proton scattering at HERA, as well as the $p\bar{p}$ collisions at the Tevatron and most recently the pp interactions at LHC. The fits are updated regularly, depending on a new data availability. Several collaborations, each using different approach and parametrisations to perform the global fit, exist. In this thesis recent PDFs sets, as provided by: CTEQ [23], ABM [24], HERAPDF [25], MSTW [26], NNPDF [27] and JR [28] groups, are used.

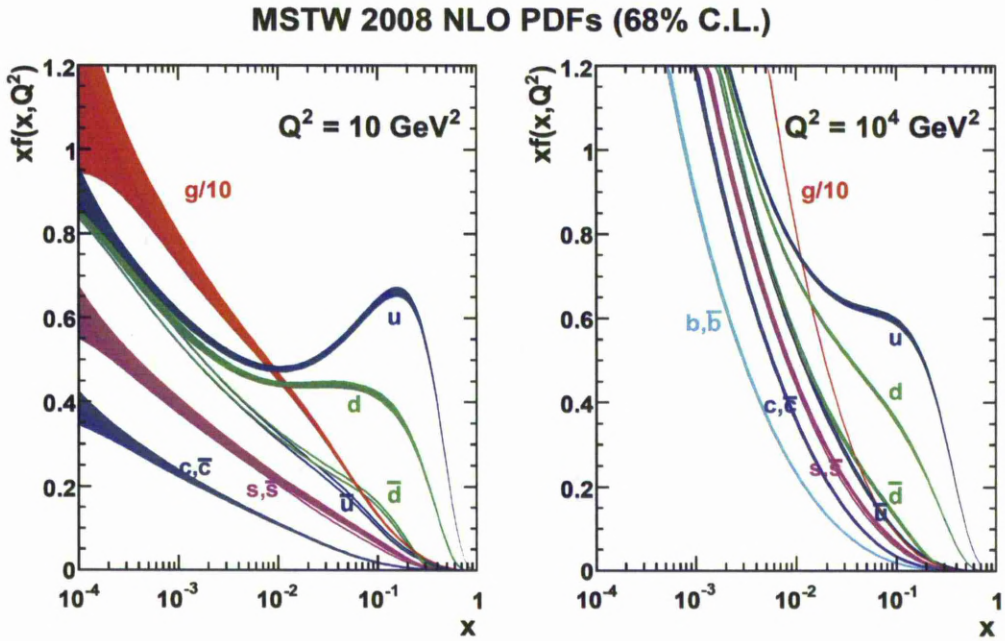

Figure 2.3: The Parton Distribution Functions as determined by the MSTW 2008 *fit at* $Q^2 = 10GeV^2$ *(left hand side) and* $Q^2 = 10^4GeV^2$ *(right hand side), corresponding to* 68% *confidence level [26].*

Figure 2.3 presents the MSTW2008 PDFs, for the two different energy scales: $Q^2 = 10GeV^2$ and $Q^2 = 10^4GeV^2$. Comparison of the PDFs at these distant scales, demonstrates one of the substantial predictions of pQCD, that as $Q^2 \to \infty$, the gluon and sea quark distributions become more dominant at the low x region.

Assuming the particle with an energy E and a certain momentum P, where p_z is its component along the z axis, it is possible to define the rapidity, y:

$$y = \frac{1}{2}\ln\left(\frac{E + p_z}{E - p_z}\right) \tag{2.3}$$

Change in rapidity is invariant under a boost in the z-direction.

In the leading order approximation the momentum fraction carried by the two scattering partons x_1, x_2 is determined by the invariant mass (M) and *rapidity* (y), of the resonant state, according to the equation:

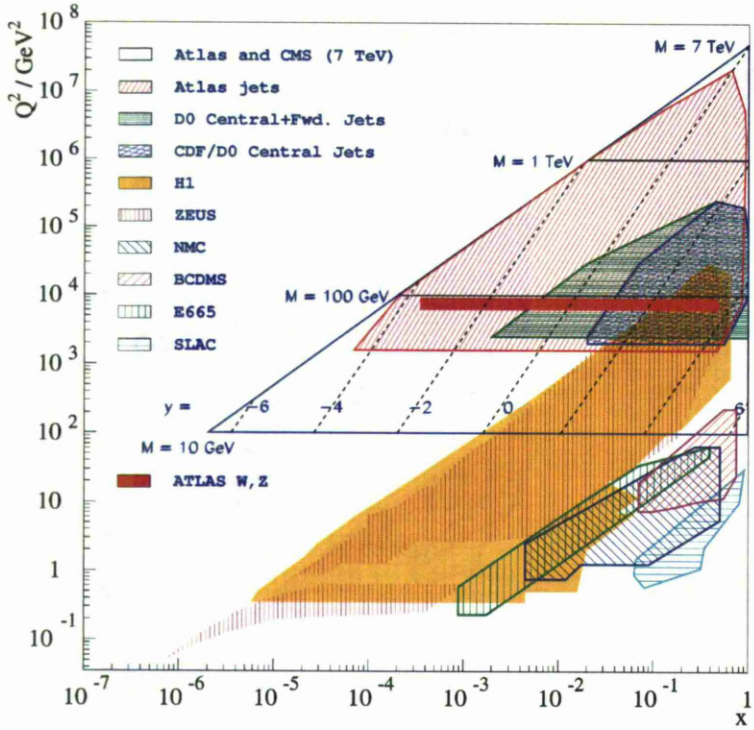

Figure 2.4: Kinematic plane of the deep inelastic scattering (DIS), in $\{Q^2, x\}$, at HERA and for fixed target experiments and their equivalent in Drell-Yan scattering (in M^2, y plane), at the Tevatron and the LHC *(for $\sqrt{s} = 7\ TeV$) [29].*

$$x_{1,2} = \frac{M}{\sqrt{s}} e^{\pm y} \tag{2.4}$$

In other words, the resonant state produced in a parton-parton collision, is characterised by an energy scale $Q^2 = M^2$, and its rapidity, where the mass and rapidity determine the momentum fraction of the interacting quarks. Therefore it is possible to represent the kinematic ranges of the deep inelastic scattering experiments, the Tevatron, and the LHC measurements in a common (x, Q^2) kinematic phase space, as illustrated in Figure 2.4. The kinematic range of the vector bosons, $W^{\pm}$, Z^0 measurements at the LHC is extended towards lower values of x (comparing to the Tevatron), due to the increase in the beam energy.

Considering the limiting case of $x = 1$, the minimum rapidity y_Z of the Z^0 boson is observed and equal to $y_Z = -\ln(2E_p/M_Z) = 4.34$, for beam energy

of 3.5 GeV. The centre of the rapidity distribution $y_Z = 0$, corresponds to $x = M_Z/2E_p = 0.013$. As seen from Figure 2.4, the x range accessed is covered by the measurements of PDFs from H1 and ZEUS [25] experiments. However the prediction of the Z^0 boson cross sections in the rapidity plateau region at the LHC requires an extrapolation of the HERA PDFs by about two orders of magnitude in Q^2. An accurate $W^{\pm}$ and Z^0 cross-section measurements at the LHC primarily tests the validity of the QCD evolution into the region of high Q^2 at small x, and provide constraints on the quark flavour contributions to the cross sections process of interest.

2.3 The Drell-Yan Production of Z/γ^* Boson

Drell-Yan (DY) scattering [30] constitutes a suitable testing ground for perturbative Quantum Chromodynamics (pQCD), as the theoretical calculations describing this process, including the higher order corrections up to next-to-leading order (NLO) [31, 32] and next-to-next-to leading order (NNLO) [33, 34, 35, 36] in perturbation theory, are available.

In the high energy proton-proton collisions at leading order (LO), the production of the Z^0/γ^* boson is due to the Drell-Yan process, where the production of lepton pairs proceeds through the exchange of a virtual photon γ^* or Z^0 boson. These two processes interfere quantum mechanically and can not be experimentally distinguished.

At the leading order (LO), the double differential Drell-Yan scattering cross-section for the process $Z/\gamma^* \rightarrow e^+e^-$ can be written as [29]:

$$\frac{d^2\sigma}{dMdy} = \frac{4\pi\alpha^2(M)}{9} \cdot 2M \cdot P(M) \cdot \Phi\left(x_1, X_2, M^2\right), \tag{2.5}$$

where M corresponds to the mass of electrons pair (e^+e^-). The propagator term and the parton distribution term are denoted $P(M)$ and $\Phi(x_1, X_2, M^2)$

respectively, and will be addressed below.

The cross-section for the discussed process is a sum of the contributions from γ^* and Z^0 exchange, as well as their interference. Therefore the propagator term $P(M)$ and the parton distribution term $\Phi(x_1, X_2, M^2)$ are presented in three different cases:

- **Photon γ^* Exchange**

$$P_{\gamma^*}(M) = \frac{1}{M^4}, \qquad \Phi_{\gamma^*} = \sum_q e_q^2 \cdot F_{q\bar{q}} \tag{2.6}$$

$$F_{q\bar{q}} = x_1 x_2 \cdot [q(x_1, M^2)\bar{q}(x_2, M^2) + \bar{q}(x_1, M^2)q(x_2, M^2)] \tag{2.7}$$

Where e_q denotes the electric charge of the quark.

- **Z^0/γ^* Interference**

$$P_{Z^0/\gamma^*}(M) = \frac{\kappa_Z v_e (M^2 - {M_Z}^2)}{M^2[(M^2 - M_Z^2)^2 + (\Gamma_Z M_Z)^2]} \tag{2.8}$$

$$\Phi_{Z^0/\gamma^*} = \sum_q 2e_q v_q \cdot F_{q\bar{q}} \tag{2.9}$$

$$v_f = I_3^f - e_f \sin^2\Theta, \qquad a_f = I_3^f [f = e, q] \tag{2.10}$$

$$\kappa_Z = \frac{1}{4\sin^2\Theta\cos^2\Theta}, \qquad \cos\Theta = \frac{M_W}{M_Z} \tag{2.11}$$

In the parton distribution term one electric charge e_q is replaced by $2\nu_q$, the neutral current vector coupling. The interference contribution is proportional to ν_e, the vector coupling of the electron, where $I_3^e = -1/2$ and $\sin^2\Theta \cong 1/4$. As the mass increases and passes M_Z, the interference propagator term changes sign from positive to negative (Equation 2.8).

- **Z^0 Boson Exchange**

$$P_{Z^0}(M) = \frac{\kappa_Z(v_e^2 + a_e^2)}{(M^2 - M_Z^2)^2 + (\Gamma_Z M_Z)^2} \tag{2.12}$$

$$\Phi_{Z^0} = \sum_q (v_q^2 + a_e^2) \cdot F_{q\bar{q}} \tag{2.13}$$

Where both the vector and the axial-vector couplings contribute as a sum of squares $(v_e^2 + a_e^2)$.

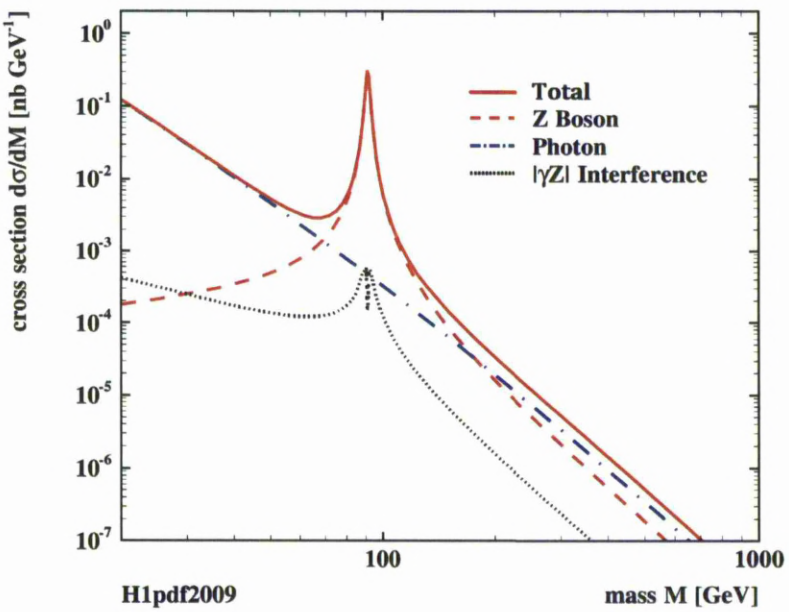

Figure 2.5: The Drell-Yan scattering cross-section of $Z/\gamma^* \to e^+e^-$ process, integrated over the boson rapidity y. The calculation uses the leading order formula, as specified in the text, and the quark distributions from H1PDF2009 *fit. The sum of γ^*, γ^*/Z^0 and Z^0 contributions is represented by a solid, red line, while the absolute value of Z^0/γ^* interference is shown in the black dotted curve [29].*

Figure 2.5 presents $Z/\gamma^* \to e^+e^-$ cross-section as a function of boson mass, and integrated over rapidity y. The pure Z^0 exchange dominates the cross-section distribution in the resonant region. At small M, the photon exchange part has a largest input. At about 70 GeV, the Z^0 and γ^* parts equally contribute to the cross-section measurement. Finally at high M, the photon exchange part again is a dominating part.

At the LHC the leading order Drell-Yan scattering is a dominant process for Z^0/γ^* production, which accounts for approximately 65% of the total cross-section [37] for this process, and is represented by Feynman diagram in Figure 2.6(a). Quark-gluon interactions give rise to higher order QCD contributions to the cross-section. The quark-gluon scattering is the dominant one, and its contribution to the overall cross-section is at the level of about 20%. An example of the quark interacting with a gluon to form a Z^0 boson is shown in Figure 2.6(b).

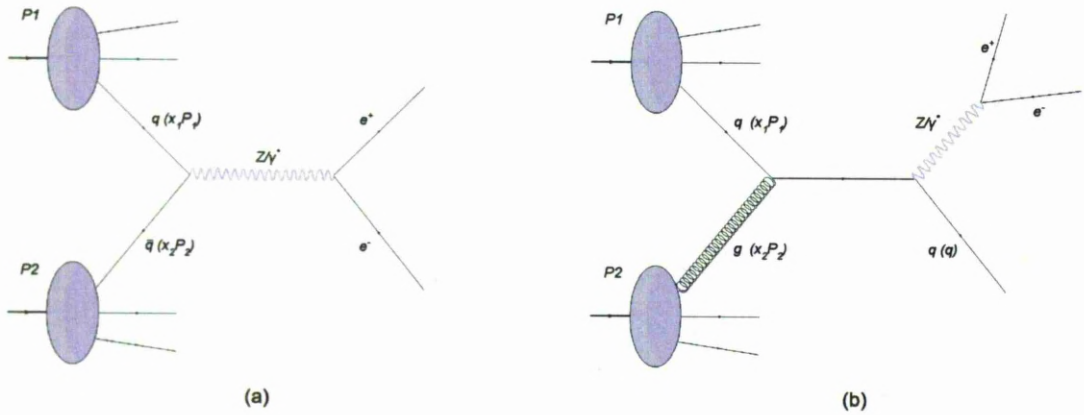

Figure 2.6: The Feynman diagrams for Z/γ^* production in a proton-proton collision. The leading order Drell-Yan process is presented on the left hand side figure, and an example of next-to-leading order diagram on the right.

The Z boson production may be associated with a gluon(s) emission, implying higher order QCD corrections to the production processes. The real emissions, in contrast to the virtual corrections, are characterised by an additional gluon in the final state. The next-to-leading order corrections to the Drell-Yan process are shown in Figure 2.7. Up to next-to-next-to-leading order (NNLO) QCD calculations are available, and the corresponding Feynman diagrams for can be found, for example, in [35].

Table 2.2 summarises the leading order (LO), the next-to leading order (NLO) and the next-to-next-to leading order (NNLO) contributions to the Z boson production.

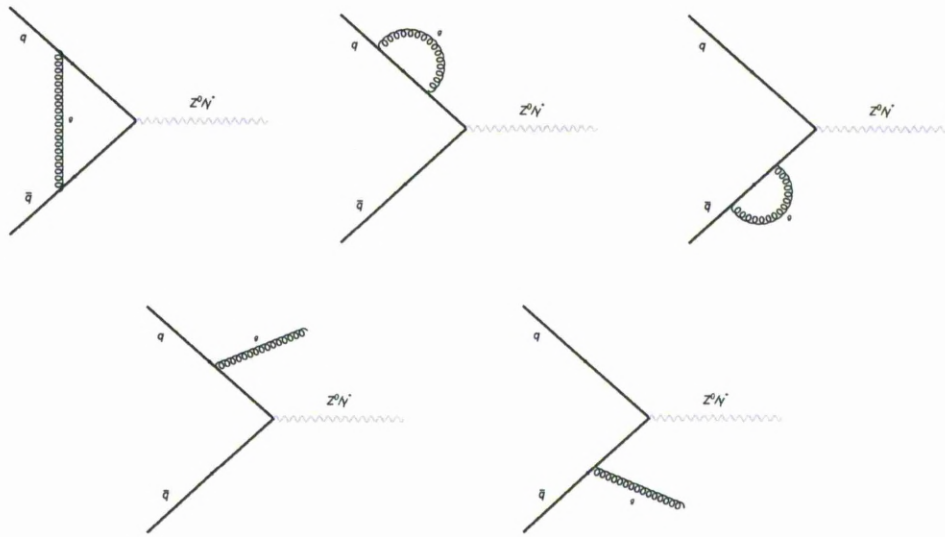

Figure 2.7: The Feynman diagrams for the NLO QCD corrections to the Drell-Yan process. The virtual corrections (top) and the real emissions (bottom) are presented.

Order	*Process*	*Correction*
LO	$q + \bar{q} \to Z$	
NLO	$q + \bar{q} \to Z$	One-loop Correction
	$q + \bar{q} \to Z + g$	
	$q(\bar{q}) + g \to Z + q(\bar{q})$	
NNLO	$q + \bar{q} \to Z$	Two-loop Correction
	$q + \bar{q} \to Z + g$	One-loop Correction
	$q + \bar{q} \to Z + g + g$	
	$q(\bar{q}) + g \to Z + q(\bar{q})$	One-loop Correction
	$q(\bar{q}) + g \to Z + q(\bar{q}) + g$	
	$q + \bar{q} \to Z + q + \bar{q}$	
	$q(\bar{q}) + q(\bar{q}) \to Z + q(\bar{q}) + q(\bar{q})$	
	$g + g \to Z + q + \bar{q}$	

Table 2.2: Various processes contributing to the Z boson production at the LHC; listed at LO, NLO and NNLO.

Decay Mode	*Branching Ratio [%]*
e^+e^-	3.363±0.004
$\mu^+\mu^-$	3.366±0.007
$\tau^+\tau^-$	3.370±0.008
Invisible	20.00±0.06
Hadrons	69.91±0.06

Table 2.3: The Z boson decay modes and their corresponding, measured branching ratios in per cent [38].

2.3.1 Z/γ^* Boson Decay

The Z boson production process is immediately followed by the decay into quark or lepton pairs, due to a very short lifetime of this boson ($\sim 10^{-24}[s]$). Therefore, experimentally detection of the Z boson proceed through the reconstruction of its decay products.

The branching ratio (BR), defined as a fraction of the partial decay rate to the total decay rate of a given process, represents probability of a certain decay mode. The decay branching ratio of a Z into a quark and anti-quark is largest. However, the hadronic channels are experimentally challenging, as the QCD background overwhelms the signal and makes impossible selection of the clean experimental sample. The second most probable decay channel includes neutrino and anti-neutrino in the final state, but as neutrinos interact weakly with matter, they pass through the detector without leaving a trace. Therefore the Z boson decay to charged lepton-antilepton pair is used to select a clean signal sample, despite its smallest branching fraction. In this study the Z boson in its electron-positron decay channel is investigated. Table 2.3 summarises possible Z boson decay modes and their corresponding branching ratios.

Chapter 3

The ATLAS Experiment at the LHC

Progress in the field of experimental particle physics relies on sophisticated instrumentation and involves large collaborations of scientists and engineers. In 1953 a Convention was signed by 12 countries, and entering into force on 29 September 1954, gave a foundation to the European Organization for Nuclear Research, known as CERN[1]. It was one of the Europe's first, large, joint projects.

Over the years it has gained new Member States and continuously increasing the number of professionals involved. CERN has come a long way since its foundation, hosting several accelerators and related experiments, and witnessing multiple important achievements in particle physics, computing science and engineering.

Presently CERN is operating the Large Hadron Collider(LHC) [39], largest and most powerful particle accelerator ever built. It is installed in the 26.7 km circumference tunnel, that was originally constructed for another CERN machine, the Large Electron-Positron Collider (LEP). The tunnel lies between 45 and 170 m underground, crossing the border of France and Switzerland.

Inside the LHC, two highly energetic parallel particle beams[2] travel at close

[1]The name CERN is the acronym derived from the name of the provisional body founded in 1952: "Conseil Europen pour la Recherche Nuclaire" (European Council for Nuclear Research). Its prime objective was to establish a major fundamental physics research organization in Europe.

[2]LHC was designed to collide proton beams at $sqrt(s)$ = 14 TeV and luminosity of

to the speed of light, in opposite direction, colliding at four points on the circumference. Four main detectors: ALICE, ATLAS, CMS and LHCb are located at the corresponding interaction points around the accelerators ring.

In addition to its major success so far, when on 4th of July 2012, ATLAS and CMS experiments reported discovery of a new particle consistent with the Higgs boson [15, 16], the research, technical and educational impact of the LHC and its experiments is hard to overestimate.

The analysis presented in this thesis uses data collected by the ATLAS Experiment in 2011, which were produced as an effect of proton-proton collisions at the centre-of-mass energy of 7 TeV. This chapter contains a brief description of the experimental setup of the LHC in Section 3.1, the ATLAS Detector in Section 3.2 and ATLAS Detector Trigger System in Section 3.3.

3.1 The Large Hadron Collider

The Large Hadron Collider (LHC) is the last element of the accelerator complex at CERN, where two particle beams are accelerated to the highest energies and then brought into collision at four interaction points [40]. The complex, schematically presented in Figure 3.1, is formed by the sequence of machines, each accelerating beam of particles to higher energy. In general it is composed of a linear accelerator (LINAC 2), the Proton Synchrotron Booster (PSB), the Proton Synchrotron (PS) and the Super Proton Synchrotron (SPS). From SPS proton beams of energy 450 GeV are injected to the LHC for the final acceleration.

$10^{34} cm^{-2} s^{-1}$. It is also possible to collide heavy (Pb) ions with nominal energy of 2.8 TeV per nucleon and a peak luminosity of $10^{27} cm^{-2} s{-}1$.

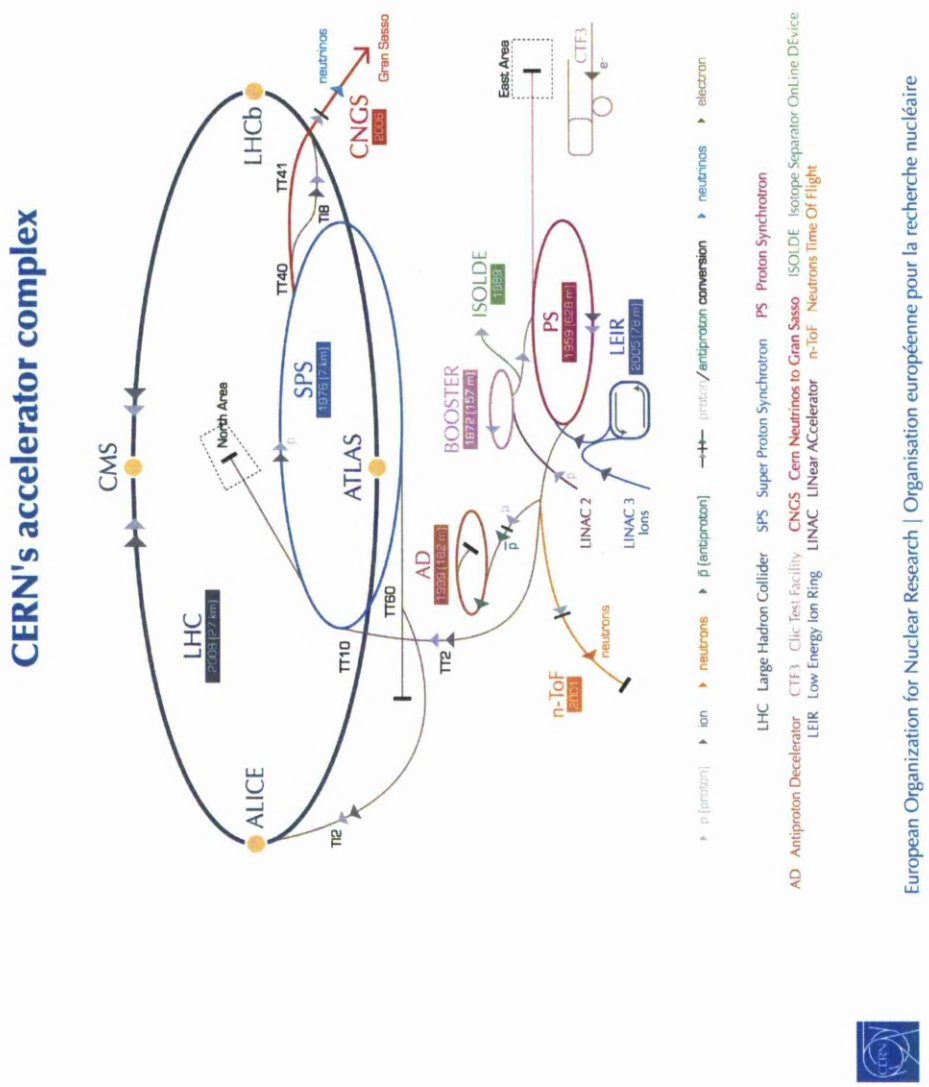

Figure 3.1: Schematic layout of the CERN Accelerator Complex [41].

In order to achieve the highest beam energies a sophisticated superconducting magnets are used [42]. A large magnetic field (8.33 T nominal value), obtained by 1232 dipole magnets, is necessary to bend the protons around the LHC ring, while additionally smaller, quadrupole magnets ensure that the beams remain well focused, guiding them to the four intersection points. Superconductivity is maintained by a cryogenic system, which uses superfluid helium at 1.9 K.

3.1.1 Luminosity

If we consider a given process x, occurring at the LHC with a cross-section σ_x, then production rate R_x of this process can be expressed as:

$$R_x = \mathcal{L}\sigma_x \tag{3.1}$$

Where $\mathcal{L}$ is the instantaneous luminosity of the LHC, one of the most important values used to describe accelerator's performance, usually in units $cm^{-2}s^{-1}$. $\mathcal{L}$ is a function of the beam parameters, and assuming Gaussian beam distribution [39], can be calculated according to the equation:

$$\mathcal{L} = F\frac{{N_b}^2 n_b f_{rev}\gamma_r}{4\pi\epsilon_n\beta^*} \tag{3.2}$$

where:

N_b - number of particles per bunch

n_b - number of bunches per beam

f_{rev} - revolution frequency

γ_r - relativistic gamma factor

ϵ_n - normalized transverse beam emittance

β^* - beta function at the collision point

Additionally, due to the crossing angle at the interaction point, the geometric

luminosity reduction factor F is introduced:

$$F = \left(\sqrt{1 + \left(\frac{\theta_c \sigma_z}{2\sigma^*} \right)^2} \right)^{-1} \tag{3.3}$$

where:

θ_c - full crossing angle at the interaction point

σ_z - RMS bunch length

σ^* - transverse RMS beam size at the interaction point.

Equation 3.3 is valid for two identical, circular beams with $\sigma_z << \beta$.

In other words, to achieve highest luminosity it is necessary to collide at hight frequency high population bunches of low emittance, and the beam optics at the interaction point need to provide lowest possible values of the amplitude functions. Moreover, to avoid luminosity reduction due to the crossing angle at the interaction point, it is necessary to bring the beams at a minimal crossing-angle, ensuring larger area of beam overlap and hence, probability of interaction. The crossing angle of about $300\mu rad$ was introduced in order to prevent unwanted beam interactions outside the actual collision point, and contributes to the luminosity loss of about 15% [38].

As LHC's running conditions change over time, hence $\mathcal{L}$ is also time dependent. Integral over time of data taking is commonly known as integrated luminosity, defined as $L \equiv \int \mathcal{L} dt$, and traditionally expressed in units b^{-1}. Figure 3.2 illustrates ATLAS delivered and recorded integrated luminosity obtained with stable beams and for pp collisions at 7 TeV centre-of-mass energy in 2011. Delivered integrated luminosity (green) refers to the total amount delivered to an experiment by the LHC, and recorded integrated luminosity (yellow), reflects the quantity, that has actually been stored into the disk space. Pictured is the luminosity as determined from counting rates provided by the luminosity detectors. Luminosity detectors are calibrated using van der Meer scans [43], where the two beams are stepwise displaced in the horizontal and vertical planes to measure

Parameter	*Nominal*	2011
Centre-of-mass Energy $\sqrt{s}$	$14TeV$	$7TeV$
Number of Colliding Bunches	2808	1332
Protons per Bunch	$1.15 \cdot 10^{11}$	$1.3 \cdot 10^{11}$
Collisions per Bunch-Crossing $\langle\mu\rangle$	22	8.95
Instantaneous Luminosity	$10^{34}cm^{-2}s^{-1}$	$3.65 \cdot 10^{33}cm^{-2}s^{-1}$

Table 3.1: Nominal LHC values for the main parameters and the numbers obtained in 2011 data taking period [38],[44].

their overlap function.

The LHC main, nominal parameters are summarised and compared to the one obtained in 2011 data taking period in Table 3.1.

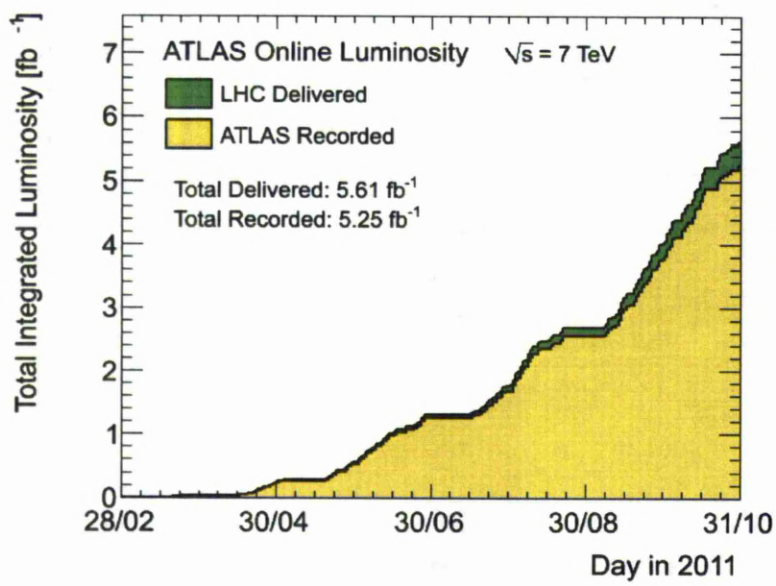

Figure 3.2: Total integrated luminosity delivered to and recorded by ATLAS experiment in 2011 [44].

3.2 The ATLAS Detector

The LHC delivers the proton beams to four interaction points (illustrated in Figure 3.1), where four detectors are located: ATLAS (A Toroidal LHC ApparatuS), CMS (Compact Muon Solenoid)[45], ALICE (A Large Ion Collider Experiment)[46] and LHCb (LHC beauty)[47].

The ATLAS experiment is a general purpose detector, with a diameter of 25 m, length of 42 m, and weight of approximately 7000 tons. This impressive size makes it the largest detector ever built at any particle collider, and considering complexity, it is designed to detect widest possible spectrum of physical processes. Details of ATLAS design, technical specification and performance were published in several extensive documents [48], [49], [50], [51]. This section will provide only a short summary and concentrate on aspects related to subject of this thesis.

Following overall detector concept, the basic design criteria of the ATLAS detector concentrate on [48]:

- Electromagnetic and hadronic calorimetry for identification and accurate measurements of electrons, photons, jets and missing transverse energy (E_T^{miss}).
- Muon spectrometry for muon momentum measurements, precise even at the highest luminosity.
- Efficient tracking system allowing measurements of charged particles with good momentum resolution and reconstruction efficiency.
- Large acceptance in pseudorapidity η with almost full azimuthal angle ϕ coverage.
- Highly efficient trigger system.

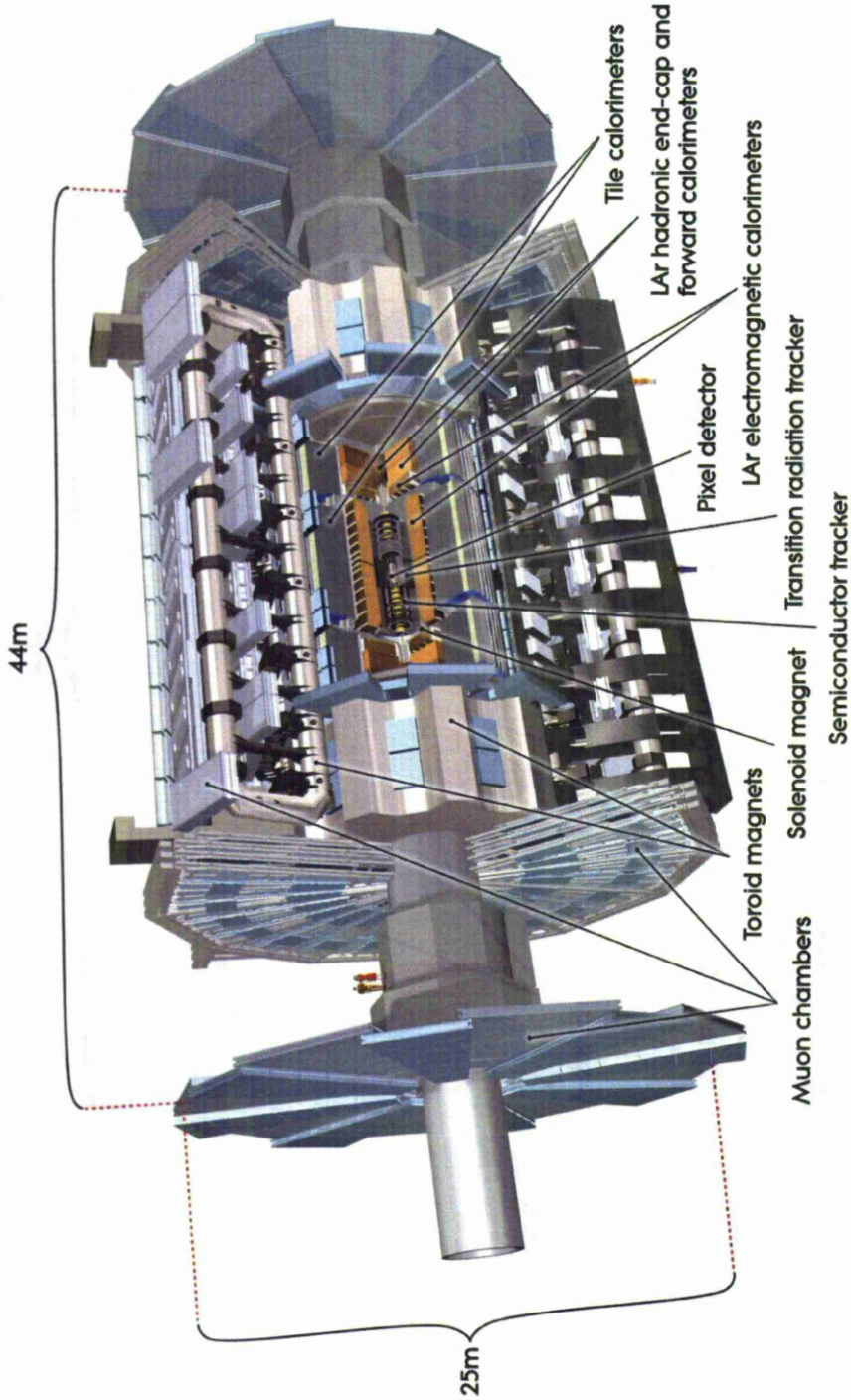

Figure 3.3: The ATLAS Detector and its main subsystems [48].

DetectorComponent	*RequiredResolution*	*η Coverage*	
		Measurement	*Trigger*
Tracking	$\frac{\sigma_{p_T}}{p_T} = 0.05\%\ p_T \oplus 1\%$	±2.5	–
Electromagnetic Calorimetry	$\frac{\sigma_E}{E} = \frac{10\%}{\sqrt{E}} \oplus 0.7\%$	±3.2	±2.5
Hadronic calorimetry			
Barrel and End-cap	$\frac{\sigma_E}{E} = \frac{50\%}{\sqrt{E}} \oplus 3\%$	±3.2	±3.2
Forward	$\frac{\sigma_E}{E} = \frac{100\%}{\sqrt{E}} \oplus 10\%$	$3.1 < \lvert\eta\rvert < 4.9$	$3.1 < \lvert\eta\rvert < 4.9$
Muon Spectrometer	$\frac{\sigma_{p_T}}{p_T} = 10\%$	±2.7	±2.4

Table 3.2: General design performance requirements of the ATLAS sub-detectors [48].

In order to fulfill these requirements, the ATLAS detector consists of a four major elements: Inner Detector (ID), Calorimetric System (CS), Muon Spectrometer (MS) and the Magnet System. The Inner Detector, composed of a Pixel Detector, Semiconductor Tracker (SCT) and a Transition Radiation Tracker (TRT), is responsible for tracking and measuring the charge and the transverse momentum p_T of the electrically charged particles. It's design ensures a coverage in $|\eta|$ direction up to 2.5 and full ϕ range. The Calorimetric System identifies photons, electrons and hadrons and measures the energy deposited in the calorimeter. The Calorimertic System is composed from an Electromagnetic Calorimeter (inner component which measures electrons and photons) and the Hadronic Calorimeter (outer component designed for detecting hadrons). The CS covers a large range of $|\eta| < 3.2$ for the main calorimetric system and additionally $3.1 < |\eta| < 4.9$ for the forward calorimeter region. The Muon Spectrometer is designed to identify, track and provide measurements of charge and momentum of the muons. The ATLAS Magnet System consists the central solenoid magnet and the toroid magnet systems. Produced magnetic field bends the trajectory of the charged particles proportionally to its strength. The central solenoid magnet provides the

magnetic field for the Inner Detector, while the toroid magnet is responsible for the Muon Spectrometer.

The layout of the ATLAS Detector and its main components are pictured in Figure 3.3, while general performance goals are summarised in Table 3.2.

ATLAS adopts right-handed coordinate system with an origin at the nominal interaction point. The x-axis pointing towards the centre of the LHC tunnel, the y-axis points upwards, towards the surface of the earth, while z-axis is defined by the beam direction (see Figure 3.4). The x-y plane is therefore transverse to the beam direction. The azimuthal angle ϕ is measured around the beam axis, and the polar angle θ is the angle from the beam axis.

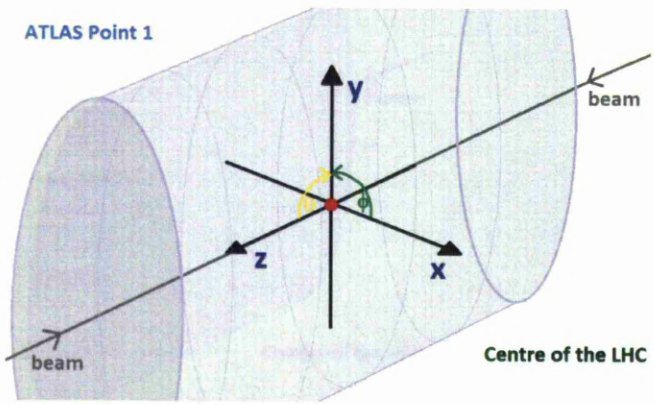

Figure 3.4: Schematic picture of the ATLAS coordinates system.

One of the most important kinematic variables used to describe objects in high energy physics is rapidity, denoted y. It can be defined using the total energy of a particle $E = \sqrt{\vec{p}^2 + m^2}$ and its momentum in the z-direction p_z, as in Equation 2.3.

In the case of massless objects, where $E = |\vec{p}|$ the rapidity can be simplified to the pseudorapidity η, and defined using the polar angle θ:

$$\eta = -\ln\left(\tan(\frac{\theta}{2})\right) \tag{3.4}$$

The pseudorapidity is zero at $\theta = \frac{\pi}{2}$. At $\theta = 0$ pseudorapidity tends to $+\infty$ and at $\theta = \pi$ to $-\infty$. Figure 3.5 shows the dependence of the pseudorapidity η versus polar angle θ.

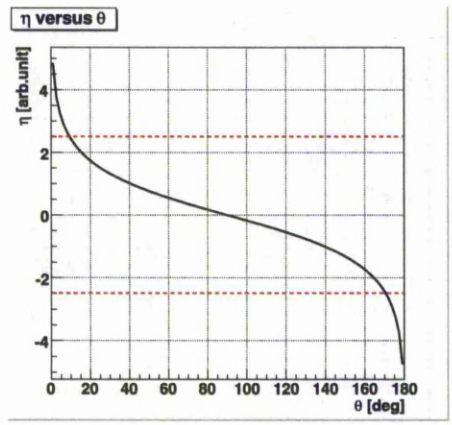

Figure 3.5: The pseuodrapidity η as a function of the polar angle θ. The ATLAS Inner Detector coverage of $|\eta| < 2.5$ indicated as a red dashed line.

The distance $\triangle R$ in the pseudorapidity-azimuthal angle $(\eta - \phi)$ space is defined as:

$$\triangle R = \sqrt{(\triangle\eta)^2 + (\triangle\phi)^2} \tag{3.5}$$

The transverse momentum p_T is the part of the total momentum of a particle produced in a collision, that is perpendicular to the direction of the incoming beams, and can be defined in the x-y plane, as:

$$p_T = \sqrt{p_x^2 + p_y^2} = |p| \sin\theta \tag{3.6}$$

Similarly the transverse energy E_T and the missing transverse energy E_T^{miss} are defined.

3.2.1 The Inner Detector

The Inner Detector (ID) is the innermost part of ATLAS Detector, and situated closest to the interaction point, withstands the rigorous LHC environment of collisions at 40 MHz bunch-crossing rate. The ID is responsible for the tracking of charged particles, providing pattern recognition, momentum determination, and primary and secondary vertex measurements. The Pixel Detector, the Semiconductor Tracker (SCT) and the Transition Radiation Tracker (TRT), these three sub-systems compose the ID and provide a high granularity design, using the silicon technology in the first two layers (pixels and SCT), and a straw tube gaseous detector in the outer layer (TRT). Composition of the Inner Detector and its structure is schematically presented in Figure 3.6 and Figure 3.7. The Inner Detector is immersed in a 2 T magnetic field, provided by a superconducting solenoid, which is situated on the inner face of the electromagnetic calorimeter.

The Pixel Detector

The Pixel Detector [52] contains three concentric cylinders with the axis along the beam (5, 9 and 12 cm radius respectively, called the barrel) and six concentric disks, three on each side of the barrel (called the end-cap). The innermost barrel layer, called b-layer, is dedicated to measure the primary vertex position, and especially for a precise measurement of a secondary vertices of a short-lived particles, such as B-hadrons. The building unit of the Pixel Detector is the module, each measuring 2×6 cm and containing 250 μm thick silicon, as a detecting material. A total of 1744 modules (1456 barrel modules and 288 end-cap modules), each containing 16 readout chips and number of electronic components, are used. The nominal pixel size is 50×400 μm, and with 46080 pixels per module, the total number of pixels in the system is approximately 80 million (67 million in the barrel and 13 million in the end-caps), covering a total active area of about $1.7 m^2$.

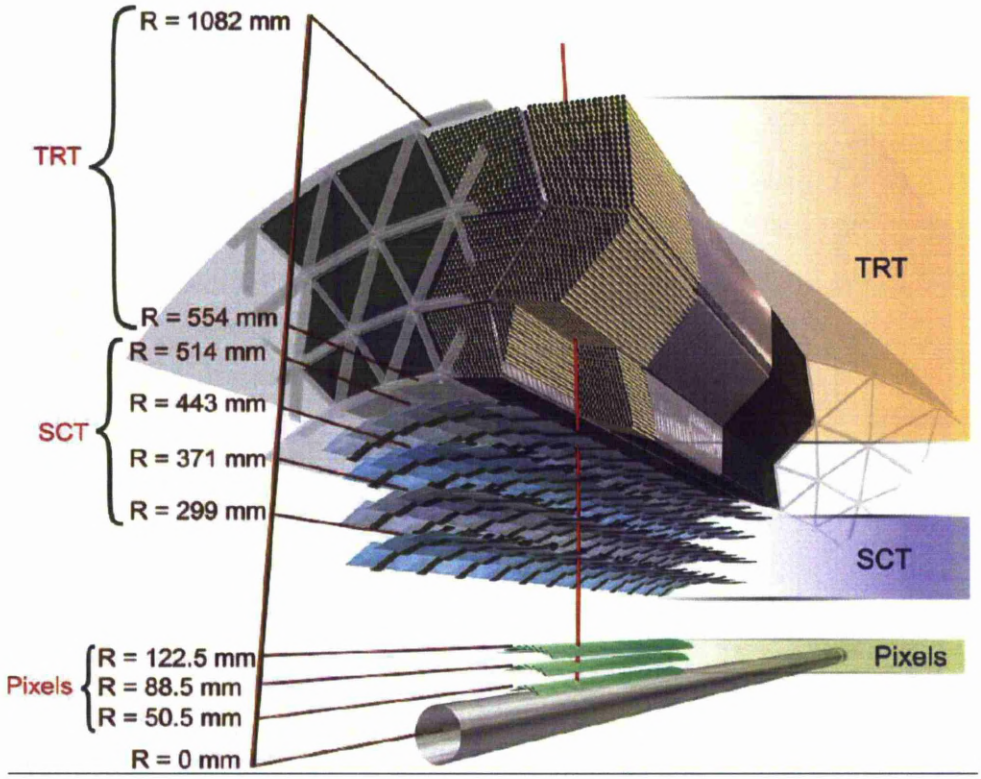

Figure 3.6: Drawing of the ATLAS Inner Detector, showing the structure of the Pixel Detector, the Semiconductor Tracker (SCT) and the Transition Radiation Tracker (TRT). A track of $p_T = 10GeV$ at $\eta = 0.3$, traversing the barrel region of the ID is also shown [48].

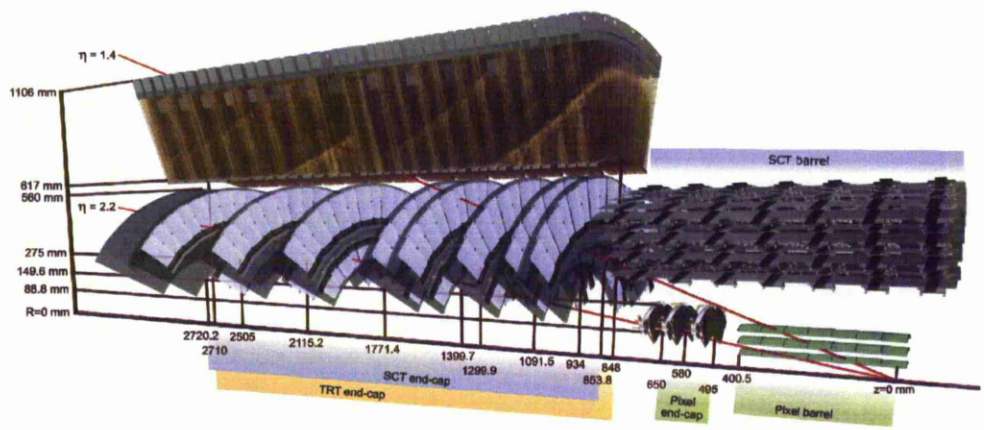

Figure 3.7: The ATLAS Inner Detector traversed by two 10 GeV tracks with $\eta = 1.4$ and $\eta = 2.2$ in the end-cap (the TRT barrel detector is not shown) [48].

The Semiconductor Tracker

The Semiconductor Tracker (SCT) [53] is the middle component of the Inner Detector, and as the Pixel Detector, it is also composed of a barrel and two end-cap regions (called End-cap A and End-cap C), but rather than small pixels it uses long, narrow strips, providing larger active area. There are four barrel layers and nine discs at each end-cap, consisting 4088 modules in total (2112 in barrel and 1976 in the end-caps). The silicone microstrip sensors are used as a detecting medium. There are 8448 single-sided sensors installed in the barrel and 6944 in the end-caps, where majority of the modules contain two sensors on each side of the module, glued back-to-back with a small angle of 0.040 rad between them. This allows to obtain three dimensional hit information and determine a resolution in the z-direction. Typically four hits are obtained for each charged particle track, with a single hit efficiency between $97 - 100\%$ (depending on the layer, including acceptance losses). The SCT has approximately 6.3 million readout channels and a total active area of 61 m^2.

The University of Liverpool ATLAS group was highly involved in all aspects of the construction, testing, installation and commissioning of the Semiconductor Tracker End-cap C. Majority of work was carried out in the Liverpool Semiconductor Detector Centre (LSDC) and the Oliver Lodge Laboratory workshop. In particular this included production, testing and assembly of the modules. A total of 988 SCT end-cap modules were successfully mounted onto nine discs in Liverpool.

The Transition Radiation Tracker

The Transition Radiation Tracker (TRT) [54] is the outermost part of the Inner Detector, with a two main components: a straw tracker and a transition radiation detector. The TRT contributes to the Inner Detector tracking system, as well as has an excellent electron identification capability. Similarly to the Pixel

Detector and the Semiconductor Tracker, the TRT contains barrel and two end-cap regions. The TRT is built of 298000 cylindrical drift tubes (straws), each up to 144 cm long and 4 mm in diameter, filled with a $Xe(70\%)CO_2(27\%)O_2(3\%)$ gas mixture. Xenon is used for its good X-ray absorption, while oxygen and carbon dioxide to increase the drift velocity of the electron and for photon quenching. The straws, containing a 30 μm in diameter gold plated tungsten wire in their centre, are kept under a high voltage of a negative polarity (about -1500 V) and act as cathodes. When a charged particle passes through, the gas mixture becomes ionised, and the drift electrons are detected by the wire, producing a signal. The track of a given particle is determined by analysing a pattern of wires, that have produced a signal. The layers of straws are interleaved with transition radiation material (polypropylene-polyethylene fibres in the barrel and polypropylene foils in the end-caps), which causes the ultra-relativistic charged particles passing through to produce low energy transition radiation photons [3]. This process contributes to the ionisation of the gas mixture, increasing amplitude of the signal. Moreover the number of transition radiation photons produced by a given particle is proportional its relativistic factor $\gamma = \frac{E}{m}$, and electrons with mass $m_e = 0.511\ MeV$ are able to emit more transition radiation than the pions with mass $m_\pi = 140\ MeV$. For that reason, the TRT uses two thresholds for a signal recognition. A low threshold is adopted for tracking and a high threshold to identify electrons (particle tracks with many very strong signals are associated with electrons). The TRT is not as precise as Pixel Detector or SCT, but it provides about 36 hits per track, allowing reconstruction of even a very long tracks, and contributes to measurements of the momenta of high p_T particles with small track curvatures.

[3] This process, known as transition radiation, occurs when relativistic charged particles cross the boundary between two media characterised by different dielectric constants.

3.2.2 The Calorimeter System

The ATLAS Calorimeter System is composed of the Electromagnetic Calorimeter and Hadronic Calorimeter, and its using sampling calorimeters based on two different technologies: liquid Argon (LAr) [55] and scintillating tiles [56]. Situated just outside the solenoidal magnet surrounding the Inner Detector, the calorimeters provide energy and position measurement of electrons, photons and hadrons over an $|\eta|$ range < 4.9. As these particles pass through the calorimeter, they interact (either electromagnetically or via strong processes) with the absorbing material and produce showers of secondary particles, until their full absorption. This energy deposition is then sampled to provide basis of accurate electrons, photons and jets identification, as well as E_T^{miss} measurements. In general the electromagnetic showers are fully included in the Electromagnetic Calorimeter, while longer and broader hadronic showers in Hadronic Calorimeter. A cut-away view of the ATLAS Detector Calorimeter System is presented inFigure 3.8.

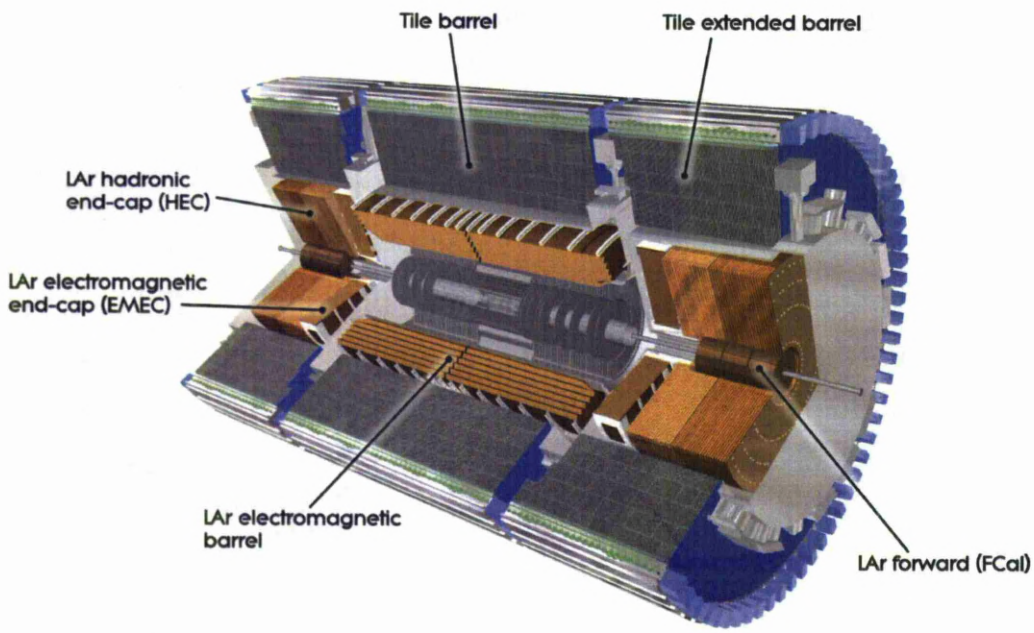

Figure 3.8: The cut-away view of the ATLAS Calorimeter System [48].

The Electromagnetic Calorimeter

The Electromagnetic calorimeter is composed of a barrel part ($|\eta| < 1.475$) and two end-cap elements ($1.375 < |\eta| < 3.2$). The barrel part, built of two identical half-barrels, is separated by a 4 mm thick gap at z = 0. Each end-cap element contains two coaxial wheels: an outer one covering the region $1.375 < |\eta| < 2.5$, and an inner one covering $2.5 < |\eta| < 3.2$. Over its full coverage the EM calorimeter uses LAr as a detection medium and lead plates as an absorbing material, where the accordion geometry provides full ϕ-coverage without azimuthal cracks.

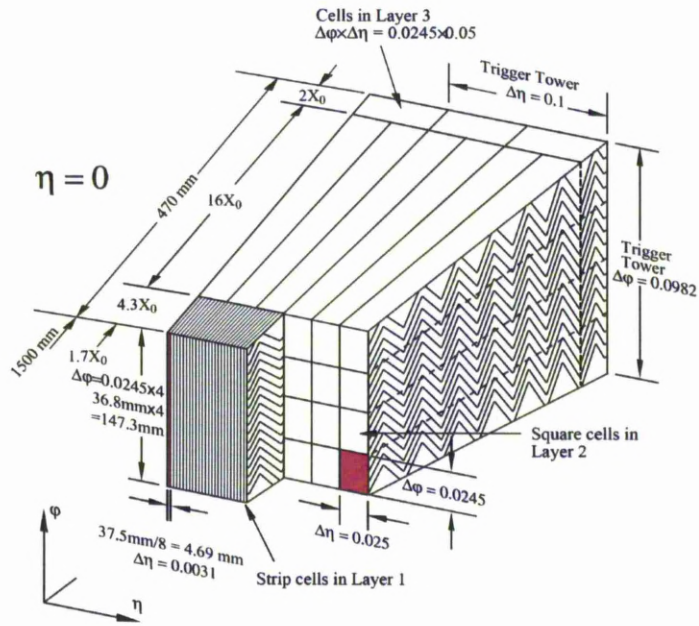

Figure 3.9: Sketch of the Electromagnetic Calorimeter barrel module with the accordion geometry and different layers shown [48].

Over the region dedicated to precision measurements ($|\eta| < 2.5$, i.e. matched to the ID in η), the EM calorimeter is segmented in three sections in depth, and characterised by a fine granularity, while the region covering $2.5 < |\eta| < 3.2$ is segmented in two sections in depth and has a coarser lateral granularity. Schematic picture of the barrel module is shown in Figure 3.9, where three layers are vis-

ible. The first layer, finely segmented in strips along η, is suitable for accurate position measurements. In the second layer the largest fraction of the energy of the shower is deposited. Finally the third layer is less segmented, as it collects only the tail of the electromagnetic shower. Moreover, in the range of $|\eta| < 1.8$, an additional LAr layer was incorporated. Acting as a pre-sampler, it allows to determine and correct for the energy loss in the ID, the solenoid and the cryostat wall. The transition region between barrel and end-caps, corresponding to $1.37 < |\eta| < 1.52$, contains a large amount of material (used for services, support structures, etc), resulting in a reduced performance. Therefore this region is excluded from analysis presented in this thesis.

The Hadronic Calorimeter

The Hadronic Calorimeter is positioned around the EM calorimeter and covers the range $|\eta| < 4.9$. Its main function is reconstruction, identification and energy measurement of particle jets and E_T^{miss} determination. In the region of $|\eta| < 1.7$ hadronic calorimetry is performed by the Tile Calorimeter (central barrel part corresponds to $|\eta| < 1.0$ region, while so-called extended barrel covers $0.8 < |\eta| < 1.7$), using the scintillating tiles as the active material and steel for absorption. The tiles are placed in a periodic pattern with a photomultiplier tubes located behind every module. Wavelength shifting fibres connect tiles with a photomultiplier, allowing the scintillation light to be read out. A schematic drawing of the Tile Calorimeter module is presented in Figure 3.10.

In the end-cap regions, similarly to the Electromagnetic Calorimeter, LAr is used as an active material but with copper, rather than lead as an absorbing medium. Each end-cap is composed of two separate wheels with two longitudinal layers each, giving total of four layers per end-cap region.

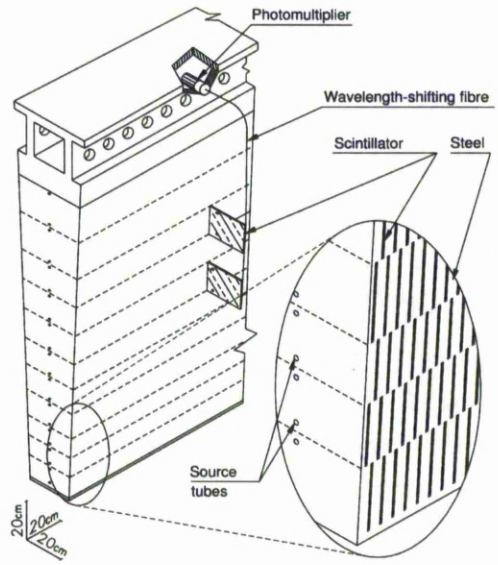

Figure 3.10: Sketch of the Tile Calorimeter barrel module with the various components of the optical readout [48].

The Forward Calorimeter

The Forward Calorimeter uses the LAr technology and extends $|\eta|$ coverage up to 4.9. It is composed of three layers. The first one is optimised for an electromagnetic measurements and adopts copper plates for absorption, while the remaining two measure energy of the hadronic interactions, using tungsten as an absorbing material.

3.2.3 The Muon Spectrometer

The Muon Spectrometer is a part of the ATLAS Detector not directly related to the analysis presented in this thesis, therefore it is only briefly summarised for completeness, whereas a detailed description can be found in [48] or [57].

The outer part of the ATLAS Detector consists the Muon Spectrometer, which is the largest sub-detector in terms of detector's volume. Its main objective is to detect and measure momenta of charged particles exciting the Calorimeter

System. In fact the only known final state particles[4] to pass all other sub-detectors and reach the Muon Spectrometer are muons. The superconducting air-core toroid magnets are used to bend trajectories of the particles. The magnet system is composed of a long barrel, covering the range $|\eta| < 1.4$ and two end-cap magnets, covering $1.6 < |\eta| < 2.7$. In most of the η range precision tracking is provided by the Monitored Drift Tube (MDT) Chambers, while in the region $2 < |\eta| < 2.7$ the Cathode Strips Chambers (CSC) are used for this purpose.

3.3 Trigger System

Existence of the highly efficient trigger system [50] was one of the basic design criteria of the ATLAS Detector. With an initial bunch-crossing rate of 40 MHz the rate of selected events is reduced by the Trigger System to about 200 Hz, enabling recording and offline processing. While this is a significant rejection, the trigger system remains reliable and sensitive to interesting physics processes. In order to perform successfully ATLAS trigger is organised in three levels, where each level gradually reduces the number of accepted events. Events selected by the trigger are recorded by the Data AcQuisition (DAQ) system. A schematic illustration of the ATLAS Trigger and DAQ System is shown in Figure 3.11.

3.3.1 The L1 Trigger

The first level of ATLAS Detector Trigger System is called Level-1 (L1), and it is a hardware based trigger, which also allows flexible programming of thresholds, according to variable run conditions, physics requirements or increasing luminosity. For each collision event L1 makes a decision, in less than 2.5 μs, whether or not to pass it to the next level [48]. The L1 trigger selects objects with high-p_T (muons, electrons, photons, jets, τ-leptons decaying into hadrons), as well as events with a large missing or total transverse energy. The L1 trigger selection is

[4]Except for neutrinos, which pass through all parts of the ATLAS Detector, remaining undetected.

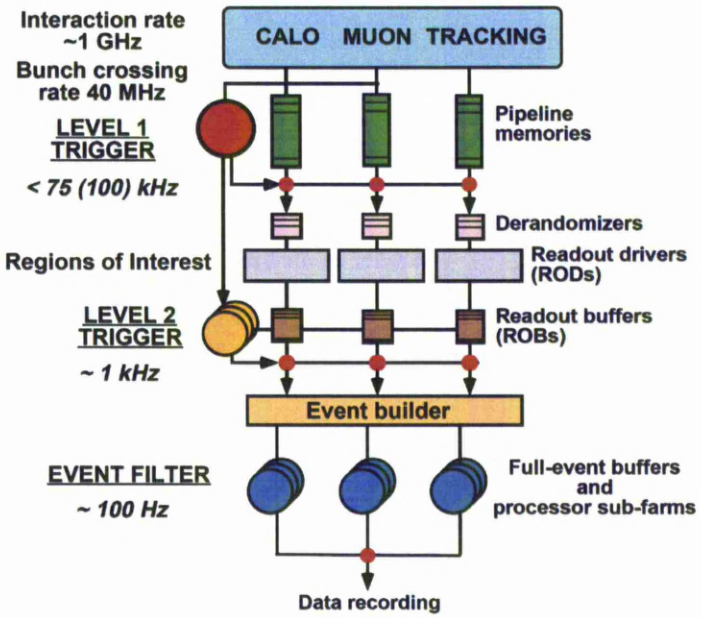

Figure 3.11: Schematic representation of the ATLAS Detector Trigger and Data Acquisition System [50].

based on reduced granularity information from the Calorimeters and the Muon System, where significant energy deposits are localised in $\eta - \phi$ space and defined as Regions of Interest (ROIs). When certain conditions and thresholds applied by L1 are met, then the ROIs are processed further by the next level of trigger system. During 2011 data taking period the output rate from L1 trigger does not exceed 60 kHz [58].

3.3.2 High Level Trigger

Following L1 Trigger, there are Level-2 (L2) and Event Filter Triggers, composing so-called High-Level Trigger (HLT), which is software based. The Level-2 Trigger (L2) uses fast custom algorithms to process partial event data within Regions of Interest (ROIs) identified by L1. The detector- specific Readout Buffers (ROBs) are responsible for storing data from L1 accepted events until L2 decision is made. On average L2 processing time is about 40 ms per event and an output event

rate is reduced to approximately 5 kHz (on average in 2011 [58]). When a given event passes L2 trigger, the Event Builder accesses ROBs and assembles event fragments to provide the Event Filter (EF) with a full event information. The EF reduces the event rate to $\sim$400 Hz with an average event processing time of 4 s. The EF algorithms use the full granularity and precision of ATLAS Detector to refine the trigger selections. Events that pass the EF are recorded.

Chapter 4

Electron Reconstruction and Identification

All proton-proton collision events, that successfully pass through the ATLAS Trigger are recorded and available for an offline reconstruction. In this process interesting physics objects like electrons, photons, muons, taus and jets (as well as E_T^{miss}) are reconstructed form the raw data, using common ATLAS software framework, called *ATHENA* [59]. The main purpose of the *ATHENA* software is to generate, simulate, digitize and reconstruct LHC events in the ATLAS Detector, ensuring a common approach for software development and the design of its packages at the same time.

This thesis investigates Z^0 boson in an electron[1] decay channel and relays on the reconstruction, identification and trigger efficiency of electrons within the ATLAS Detector. The following chapter describes offline electron reconstruction in Section 4.1, identification process in Section 4.2 and corresponding performance in Section 4.3. Section 4.4 include a brief description of the electron energy scale and resolution determination. In the final part (Section 4.5) electron charge identification efficiency is presented.

[1] If not stated explicitly, therm "electron" is used to describe both, electron as well as positron.

4.1 Electron Reconstruction

Electron reconstruction [60] is based on information from two ATLAS sub-detectors: the Inner Detector and the Electromagnetic Calorimeter. For electrons considered in this thesis, which are reconstructed in the central region corresponding to the pseudo-rapidity range of $\eta < 2.47$, as defined by the tracker and granularity of the EM calorimeter, reconstruction is initialised by energy deposits in the EM calorimeter. The energy deposits, called clusters, are subsequently matched to corresponding tracks reconstructed by the Inner Detector, to form electron candidates.

4.1.1 Cluster Seed Reconstruction

The standard *egamma* electron reconstruction algorithm [2] is used in this analysis. A preliminary set of seed clusters is selected by a *sliding−window* algorithm from local maxima of energy deposited in the EM calorimeter and within this window's size. The window is a fixed size rectangle defined, with respect to the granularity of the calorimeter's middle layer, to be 3×5 cells in units of 0.025×0.025 in $\eta \times \phi$ space. The seed clusters with a total transverse energy above 2.5 GeV are considered.

4.1.2 Track Reconstruction and Matching

The track reconstruction starts with a seed tracks identification in the Pixel detector and the first layer of the SCT, and subsequently additional SCT hits are used to form the track candidates, within the tracking volume of $|\eta| < 2.5$. All track candidates which pass good quality criteria are loosely matched to seed clusters by extrapolation of the last measured point to the second layer of the calorimeter. The spatial separation between the cluster and the track is required

[2] There are two main offline electron reconstruction algorithms used in ATLAS. One, called "*egamma*", described briefly in this chapter and second, optimised for a low energy electrons, track-seeded reconstruction algorithm (called "*softe*"), not treated here.

to be $\Delta\eta < 0.05$ and $\Delta\phi < 0.1$. An electron is reconstructed if at least one track is successfully associated with a seed cluster, but in a case when there are several tracks matched to the same cluster, the priority is given to the one with silicon hits and the smallest $\Delta R = \sqrt{\Delta\eta^2 + \Delta\phi^2}$ distance.

4.1.3 Full Cluster Reconstruction

After the track-cluster matching the electron cluster is rebuilt using 3×7 and 5×5 sliding windows (in η/ϕ middle layer cell units) in the barrel and end-caps respectively, allowing for different overall energy distributions in these two regions to be reconstructed effectively. The total cluster energy is calculated [48] by taking into account electron energy deposits in the different parts of the detector (both active and inactive) and briefly this contributions include:

- Energy deposited in the material in front of the EM calorimeter (estimated)
- Energy deposited in the cluster (measured)
- Lateral leakage - energy deposited outside the cluster (estimated)
- Longitudinal leakage - energy deposited outside the EM calorimeter (estimated)

An accurate cluster energy determination relies on detailed *MonteCarlo* simulation of energy deposition within the active and inactive parts of the detector in order to several corrections to the reconstructed cluster energy to be applicable. Finally the energy of the electron is given by the energy of the cluster, while the η and ϕ directions are obtained from the corresponding track parameters.

4.2 Electron Identification

The baseline identification of electrons [60], [61] in the central pseudo-rapidity region ($|\eta| < 2.47$) of ATLAS relies on a cut-based selection, which allows separation of isolated electrons from other backgrounds. The selection uses the

calorimeter, tracking and combined variables in order to distinguish signal electrons, electrons originating from photon conversions or Dalitz decays, as well as jets, which fake electrons. The cuts have been defined within offline *IsEM* menu and grouped into three categories: *loose*, *medium* and *tight*, where each set has increasing background rejection power and can be applied independently. In order to confront an increasingly high luminosity conditions of the LHC, the whole *IsEM* menu has been reviewed, optimised and consequently replaced in 2011 by a new menu, called *IsEM++*, which includes *loose++*, *medium++* and *tight++* sets of cuts [62]. The full list of variables used to define *loose++*, *medium++* and *tight++* sets of electron identification criteria is summarised in Table 4.1.

- ***Loose++*** Set of identifications requirements using calorimeter variables, such as a shower shape and the energy leakage into the hadronic calorimeter, as well as track quality cuts (minimum seven silicon hits, including at least one in the pixel layer). Moreover a loose cluster-track matching in η direction is applied ($|\Delta\eta| < 0.015$).

- ***Medium++*** Set of identification requirements, which in addition to all *loose++* listed above, includes a tighter cluster track matching in η ($|\Delta\eta| < 0.005$) and loose cuts on the TRT high threshold hits ratio. For the region $|\eta| > 2.01$ more demanding conditions need to be met with respect to the shower shape and track hits, while for $|\eta| < 2.01$ at least one hit in b-layer is requested.

- ***Tight++*** Set of identification requirements, which in addition to all *loose++* and *medium++* listed above, introduces additional cut on the cluster energy over track momentum variable (E/p). This cut is defined as an interval between minimum and maximum E/p value, depending on a given electron η and cluster energy (defined as $11(E_T) \times 10(\eta)$ bin matrix). Furthermore a tighter requirement with respect to the number and fraction of high

threshold TRT hits and an asymmetrical cut on the cluster-track matching following $\Delta\phi$ direction is applied.

4.3 Electron Reconstruction and Identification Efficiencies

An accurate determination of electron reconstruction and identification efficiencies is important for many physics analyses, including measurements presented in this thesis. The electron efficiency measurements are based on so-called *"tag-and-probe"* method, where in general one electron from the event, the tag electron, is required to pass a strict selection criteria ensuring clean sample, while the second electron, the probe, remains unbiased from an event selection, allowing for efficiency measurement. For a more comprehensive description of this method, please refer to Section 5.2. Those measurements are carried out using both data and Monte Carlo samples, and the results are compared to reveal possible differences, usually present due to a small Monte Carlo mis-modeling of the detector components and/or additional material distributions. The *Scale Factors* are defined as a ratio of measured (data) over simulated (MC) efficiencies, and applied to the Monte Carlo generated samples, in order to correct for the data/Monte Carlo discrepancy.

Dedicated studies of the electron efficiencies were performed and relevant scale factors were obtained by the *egamma* group, results are presented in [63], [62] and [58].

The official ATLAS recommendations for the values of the scale factors originating from electron trigger, reconstruction and identification efficiency studies, are used for the Z boson cross section measurement summarised in this thesis.

Type	*Description*
	***Loose++* Selection**
Acceptance	$\|\eta\| < 2.47$
Hadronic leakage	Ratio of E_{T} in the first layer of the hadronic calorimeter to E_{T} of the EM cluster (used over the range $\|\eta\| < 0.8$ and $\|\eta\| > 1.37$)
	Ratio of E_{T} in the hadronic calorimeter to E_{T} of the EM cluster (used over the range $\|\eta\| > 0.8$ and $\|\eta\| < 1.37$)
Second layer of EM calorimeter	Ratio of the energy in 3×7 cells over the energy in 7×7 cells centred at the electron cluster position
	Lateral width of the shower
First layer of EM calorimeter	Total shower width
	Ratio of the energy difference associated with the largest and second largest energy deposit over the sum of these energies
Track quality	Number of hits in the pixel detector (≥ 1)
	Number of hits in the pixel and SCT detectors (≥ 7)
Cluster-track matching	$\Delta\eta$ between the cluster and the track (< 0.015)
	***Medium++* Selection (includes *Loose++*)**
b-layer	Number of hits in b-layer (≥ 1) for $\|\eta\| < 2.01$
Track quality	Number of hits in the pixel detector (> 1) for $\|\eta\| > 2.01$
	Transverse impact parameter (< 5 mm)
Cluster-track matching	$\Delta\eta$ between the cluster and the track (< 0.005)
TRT	Loose cut on the TRT high-threshold fraction
	***Tight++* selection (includes *Medium++*)**
Track quality	Tighter transverse impact parameter cut (< 1 mm)
Cluster-track matching	Asymmetric cut on $\Delta\phi$ between the cluster and the track
	Ratio of the cluster energy to the track momentum (E/p)
TRT	Total number of hits in the TRT
	Cut on the TRT high-threshold fraction
Conversions	Electron candidates matched to the reconstructed photon conversions are rejected

Table 4.1: Detailed list of identification variables used for the loose++, medium++ and tight++ electron identification requirements for the central region of the ATLAS detector ($|\eta| < 2.47$) (based on [62]).

4.3.1 Electron Reconstruction Efficiency

The electron reconstruction efficiency is defined as the probability, that the dedicated algorithm will reconstruct a genuine electron depositing its energy in the EM cluster. The efficiency measurement is performed with respect to the reconstructed cluster (for electrons with $E_T > 2.5\ GeV$, assumed to be a 100% efficient process) and represents the track reconstruction and the cluster-track matching performance. The tag-and-probe method was used to calculate reconstruction efficiencies, requiring a tag electron to pass tight ID criteria and match the trigger while a probe is considered to be an electron or photon (allowing identification of cluster-track matching failure) candidate. Further cut on the invariant tag-probe mass of $80 - 100\ GeV$ (after background substraction) is the discriminating variable. Reconstruction efficiency includes track quality and the hadronic leakage fraction cuts performance, as introduced by a new *loose++ IsEM* menu. The studies were accomplished in two-dimensional bins of electron p_T and η, in order to obtain a high precision and minimise systematic uncertainties. The electron reconstruction efficiency as a function of probe η is shown in Figure 4.1. The efficiency to reconstruct an electron with a good quality track matching an electromagnetic cluster that fulfills the hadronic leakage fraction requirement is approximately 90% for the end-cap region and about 96% in the barrel region, for high E_T probes. Corresponding Scale Factors (SFs) are found to be very close to one, with an uncertainty of less than 0.5%. Details can be found in [63]. These SFs are applied to correct the MC samples used in analysis presented in this thesis.

4.3.2 Electron Identification Efficiency

The electron identification efficiency is defined as the probability, that the reconstructed electron candidate will fulfill one of the identification criteria (*loose++*, *medium++* or *tight++*). Efficiency studies were performed with the tag-and-

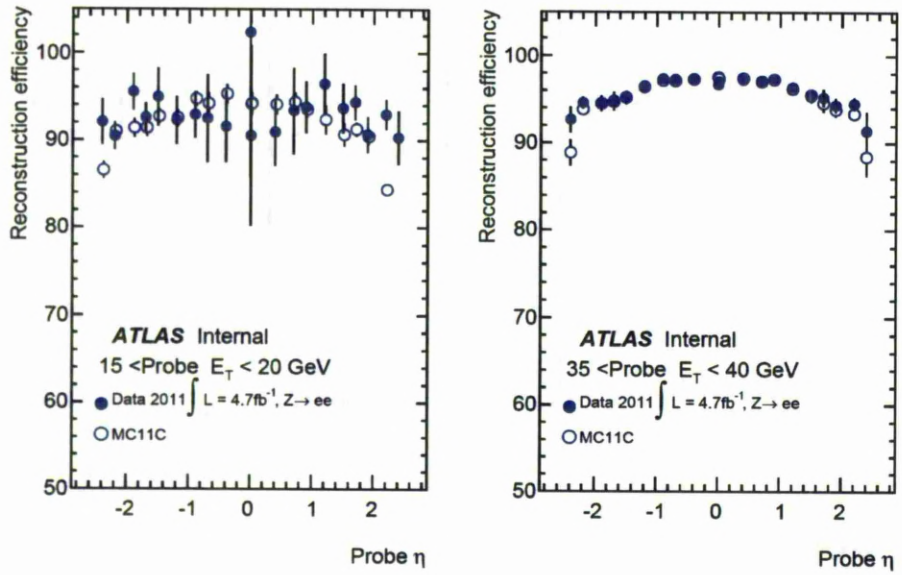

Figure 4.1: Electron reconstruction efficiencies measured in data and Monte Carlo, obtained with probes of $15 < E_T < 20$ *GeV (left) and* $35 < E_T < 40$ *GeV (right) [63].*

probe method using $W \to e\nu$, $Z \to ee$ and $J/\Psi \to ee$ events. Obtained SFs are combined and presented with statistical and several correlated systematical components. Similarly to reconstruction efficiency, the identification efficiency and corresponding SFs are calculated in a double differential binning of electron η and E_T. Details can be found in [63]. These SFs are applied to correct the MC samples used in analysis presented in this thesis. The electron identification efficiency from $Z \to ee$ events as a function of probe η is shown in Figure 4.2. The *Loose++* set of cuts was found to provide $93 - 95\%$ identification efficiency. The *Medium++* cuts select electrons with efficiency of approximately 85% and have a higher background rejection power, comparing to *Medium* menu. The *Tight++* selection introduces a slight improvement in electron identification with respect to the previous *Tight* [63].

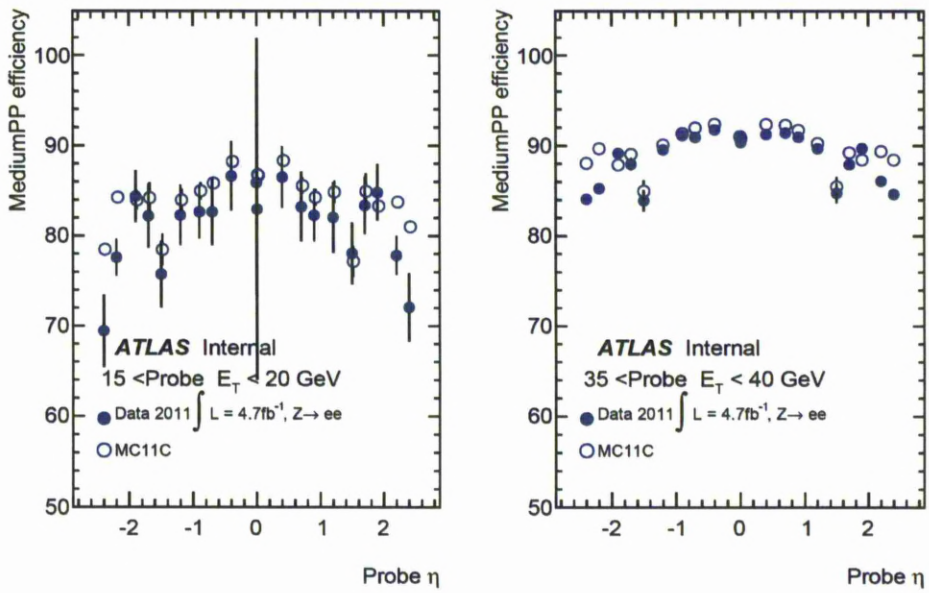

Figure 4.2: Electron Medium++ identification efficiencies measured in data and Monte Carlo, obtained with probes of $15 < E_T < 20$ *GeV (left) and* $35 < E_T < 40$ *GeV (right) [63].*

4.4 Electron Energy Scale and Resolution

An accurate calibration of the electron energy is an important factor for all physics analyses considering electrons in the final state, including a precise measurements of the W and Z boson production cross-sections. Dedicated studies have been performed to obtain the electron energy scale and resolution using various *in situ* techniques, and results are presented in [60], [64]. This thesis follows official recommendations with respect to the energy scale and resolution, by applying relevant correction factors [65].

4.4.1 Energy Scale

Initially the electromagnetic calorimeter energy scale was obtained from Monte Carlo simulations [49, 50] and test-beam measurements [66, 67, 68], and improved with ATLAS data collected in 2010 [60] and 2011 [64].

The energy scale correction factors α are determined from $Z \rightarrow ee$ and $J/\Psi \rightarrow ee$ events, using the precise knowledge of the Z and J/Ψ masses. An alternative method employing $W \rightarrow e\nu$ decay channel is used to study the E/p ratio. The electron energy scale obtained by two methods agrees within systematic uncertainties [60].

The energy measured by the calorimeter E^{meas} is expressed in terms of the true electron's energy (E^{true}) and a factor α, which accounts for a possible miscalculations in a given region i, according to the equation:

$$E^{meas} = E^{true}(1 + \alpha_i) \tag{4.1}$$

The so-called energy scale correction factors α are determined by minimizing the unbinned log-likelihood function [49], which makes use of the Z lineshape, as predicted by $PYTHIA$ MC simulation. The correction factors α_i (including statistical and several systematic uncertainties) provided for the full $|\eta| < 4.9$ range, are applied to correct electron energy in data, using $E^{corr} = E^{meas}/(1+\alpha_i)$.

In the case of an alternative method, the $W \rightarrow e\nu$ events were used to study E/p distributions fitted with a Crystal Ball function [69]. The most probable value of $\widehat{E/p}$ was determined in data and MC and compared to obtain α. The energy scale correction factors α acquired by using two alternative methods are presented as a function of the electron's cluster pseudorapidity in Figure 4.3.

4.4.2 Energy Resolution

Details of the electron energy resolution studies with 2010 and 2011 data can be found in [60] and [64] respectively.

The fractional energy resolution in the electromagnetic calorimeter is expressed as a function of η dependent parameters a, b and c:

$$\frac{\sigma E}{E} = \frac{a}{\sqrt{E}} \oplus \frac{b}{E} \oplus c \tag{4.2}$$

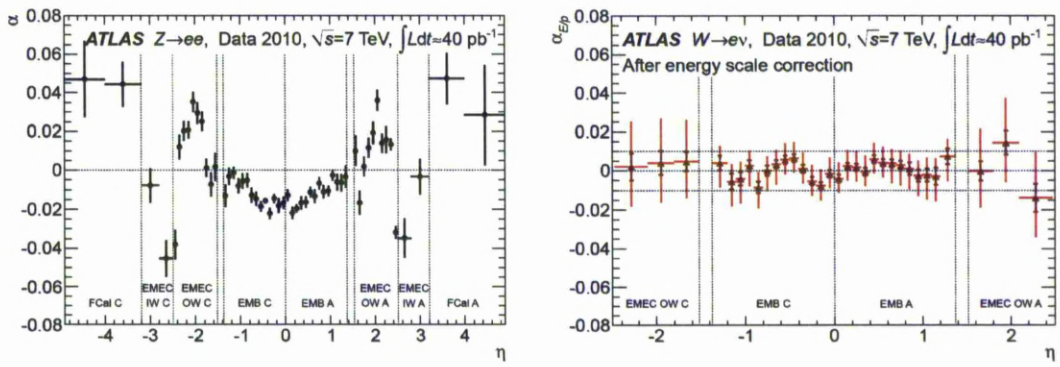

Figure 4.3: Electron energy scale correction factor α as a function of the pseudo-rapidity obtained from $Z \to ee$ (left) and $W \to e\nu$ (right) events. The $W \to e\nu$ measurement is shown after the baseline calibration has been applied [60].

where a is the sampling term, b is the noise term and c is the constant term. The sampling and noise terms (a and b) are assumed to be well modeled by the simulation and are taken from MC, while the constant term c is measured in data. For this purpose $Z \to ee$ events were studied. A di-electron mass spectrum fitted with a Breit-Wigner convoluted with a Crystal Ball function was used, so that the Breit-Wigner width is set to match the Z width and the Crystal Ball function describes the resolution. The observed differences in the energy resolution between data and Monte Carlo samples are corrected, by applying the smearing factors (random numbers distributed appropriately to match the measured resolution) to the MC reconstructed energy. The reconstructed dielectron mass distributions, for two different pseudorapidity regions, stating the Gaussian width (σ) of the Crystal Ball function for data and MC are shown in Figure 4.4.

4.5 Charge Identification Efficiency

The electron charge identification probability [63, 62] is defined as the fraction of electrons with correctly assigned charge to all charge-assigned electrons, and depends on the electron identification cuts applied. The possible inefficiency of the electron charge identification arises, when a high p_T secondary particle's track

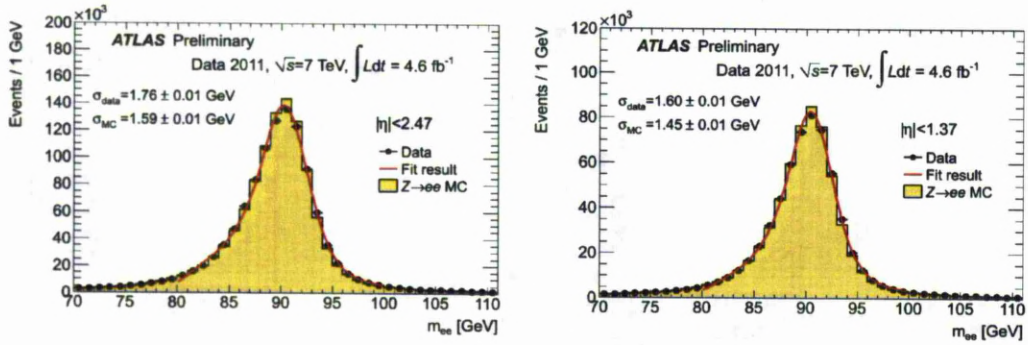

Figure 4.4: Calibrated dielectron mass distributions for $Z \rightarrow ee$ events for all pairs (left) and all pairs with $|\eta| < 1.37$ (right) [70].

or wrongly reconstructed track is matched to the EM cluster.

In order to measure the charge identification rate, the tag-and-probe method is used to study $Z \rightarrow ee$ events, and the ratio of the number of opposite sign pairs to the number of all charge-assigned pairs is determined.

The electron charge identification efficiency as a function of $|\eta|$ for *Medium++* and *Tight++* selection criteria is presented in Figure 4.5.

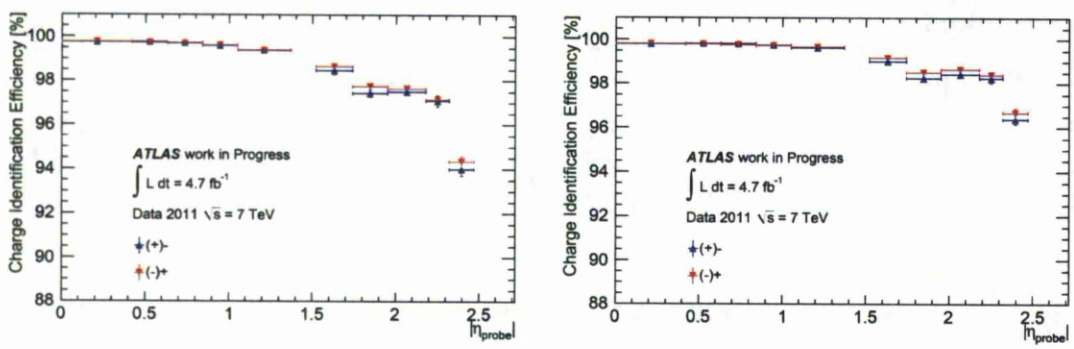

Figure 4.5: Electron (triangle) and positron (inverted triangle) charge identification efficiency as a function of $|\eta|$ for Medium++ (left) and Tight++ (right) selection cuts [62].

In general the electron charge identification is a highly efficient process with a strong η dependence, where a drop in efficiency is observed in the forward region, due to the larger amount of detector material. Moreover charge identification efficiency is not "charge sensitive", ie. no substantial difference between misiden-

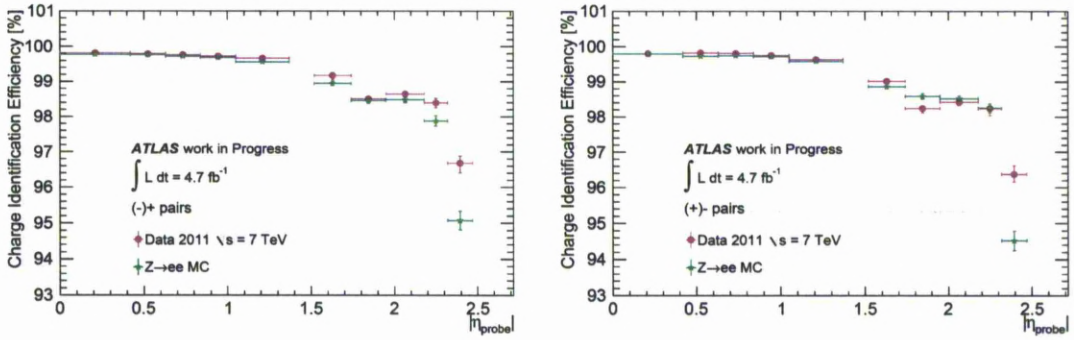

Figure 4.6: Comparison of data and Monte Carlo charge identification efficiencies for Tight++ selection of (-)+ pairs (left) and (+)- pairs (right) [63].

tification of electrons and positrons is observed. Comparison between data and MC simulation shows a good agreement in the barrel region, while for the highest η region a discrepancy is observed (see Figure 4.6).

In order to adapt the MC efficiencies to the one observed in data, the *ElectronMCChargeCorrector* tool available from *egammaAnalysisUtils* is used in this analysis.

4.6 Summary

An electron in ATLAS Detector is characterised by a narrow cluster of energy deposited in the Electromagnetic Calorimeter, that is associated with a track reconstructed in the Inner Detector. A common electron selection is a cut-based process, that uses the particle identification variables defined in the *IsEM* menu in order to separate genuine electrons from background. For 2011 ATLAS analysis the *IsEM++* menu was the basis of electron identification, introducing new *Loose++*, *Medium++* and *Tight++* operating points.

The efficiency to reconstruct and identify electrons in ATLAS Detector has been measured in 2011 using data driven techniques. A common approach is to use so-called *Tag&Probe* method. Efficiency measurements provide scale-factors (SF), which are obtained from Data to Monte Carlo (MC) comparison. The Scale

Factors are used to adjust the efficiencies predicted by MC simulation to reflect efficiencies observed in data.

The electron reconstruction efficiency exceed 90% for the whole η range, and for E_T above 15 GeV. The electron identification efficiency defined by a *Loose++* set of cuts is about $93 - 95\%$. The *Medium++* cuts identify electrons with efficiency of approximately 85%, while *Tight++* cuts provide identification efficiency of approximately $68 - 76\%$, depending on η range. The electron charge identification efficiency has a strong η dependance, with efficiency above 99% for the central region, which drops to about 94% for the forward region (for *Medium++* electrons).

Chapter 5

Electron Trigger Efficiency

Efficiency measurements related to electron identification, reconstruction and triggering are performed using data-driven methods. The introductory sections of this chapter describe the types of trigger used in 2011 data taking period, with respect to the instantaneous luminosity delivered to the LHC. Section 5.2 introduces the *Tag and Probe method* exploited in the trigger efficiency studies. The following parts present methodology for both single and di-electron trigger efficiency calculations, where comparison to the Monte Carlo predictions yields the corresponding scale factors (SF). This thesis follows an official ATLAS recommendations, with respect to the values of the scale factors used to correct for the data/Monte Carlo discrepancies, including those originating from the electron trigger efficiencies studies [58, 60]. However the Tag and Probe method is an important, and common tool for the assessment of electron efficiencies, therefore it is instructive, first to demonstrate a working example of its direct application, before specific recommendations are to be used in the cross-section measurement.

5.1 Electron Trigger Menu in 2011

The ATLAS detector trigger system is briefly described in Section 3.3, this section outline a short characteristic of different electron trigger types, as used in 2011 data taking period.

The acquisition of a given event with an electron candidate(s) in the final state, proceed according to definitions included in the electron trigger menu. The menu is flexible and definitions change, taking into account the increasing instantaneous luminosity and pile-up conditions of the LHC, in order to maintain the desired trigger rates. In particular, it is achieved by applying various thresholds or different sets of selection cuts.

Table 5.1 and Table 5.2 summarise the main single and di-electron triggers used and evolution in trigger rates at different levels with respect to luminosity is detailed. Name of the trigger include an information about the type of the physics object concerned (e.g. "e" stands for a single electron, or "2e" - two electron candidates in the final state), the transverse energy (E_T in [GeV]) threshold applied at EF, as well as the selectivity level of a given set of cuts used (i.e. *loose*, *medium* or *tight*).

In order to accommodate increasing instantaneous luminosity, while keeping trigger accept rates within designed limits (overall output at L1$\leq$ 60 $[kHz]$ and EF about 400 $[kHz]$), electron trigger menu was optimised by implementing the η-dependent EM thresholds, and a hadronic leakage requirement, at the L1. To mark this change, the letters *vh* were added into the naming convention. For the di-electron trigger a tighter threshold requirement was adopted (changing E_T from 7 to 10 $[GeV]$ at L1) when the instantaneous luminosity exceeded 1.5 $\times$ $10^{33}[cm^{-2}s^{-1}]$, and the symbol T was implemented in the trigger's name. At the HLT the EM threshold was raised from 20 to 22 $[GeV]$ for a single electron trigger, and from 10 to 12 $[GeV]$ for a di-electron trigger. Finally to take into account the changes in the offline electron identification criteria (Section 4.2), the *medium1* set of requirements was introduced, to trigger on the electron candidates, which satisfy the new *medium++* offline selection.

Name	*Luminosity Range* $[cm^{-2}s^{-1}]$	*L1 Rate [Hz]*	*L2 Rate [Hz]*	*EF Rate [Hz]*
e20_medium	up to 2.0×10^{33}	7300	273	50
e22_medium	$2.0 - 2.3 \times 10^{33}$	5700	273	45
e22vh_medium1	from 2.3×10^{33}	3600	150	22

Table 5.1: Single electron triggers listed with respect to the instantaneous luminosity range, when in use as a main analysis trigger. Corresponding rates at L1, L2 and EF are specified. (Based on [58].)

Name	*Luminosity Range* $[cm^{-2}s^{-1}]$	*L1 Rate [Hz]*	*L2 Rate [Hz]*	*EF Rate [Hz]*
2e10_medium	up to 0.7×10^{33}	13600	83	1.6
2e12_medium	$0.7 - 1.5 \times 10^{33}$	5900	36	0.9
2e12T_medium	$1.5 - 2.3 \times 10^{33}$	2100	36	0.9
2e12Tvh_medium	from 2.3×10^{33}	800	36	0.9

Table 5.2: Di-electron triggers listed with respect to the instantaneous luminosity range, when in use as a main analysis trigger. Corresponding rates at L1, L2 and EF are specified. (Based on [58].)

5.2 Tag and Probe Technique

The electron trigger efficiency can be extracted by applying the data-driven *Tag and Probe* method on $Z/\gamma^* \rightarrow e^+e^-$events.

In order to calculate the efficiency, a pair of related objects originating from a mass resonance (i.e. J/ψ, Z etc.), is as suitable choice. The di-electron $Z/\gamma^* \rightarrow e^+e^-$ channel has a clear signature and easily reducible background, therefore is well suited for application of the *Tag* and *Probe* technique.

The *Tag* electron is responsible for triggering an event and selected via a stringent selection, while the *Probe* electron remains unbiased from the event selection, and is used to efficiency measurement. This technique can be applied in various efficiency measurements, depending on the respective definitions of *Tag* and *Probe*. The details of the selection applied in this specific analysis are outlined below.

The adequate background subtraction is crucial for reliable extraction of

events, suitable for the *Tag* and *Probe* studies. However the background contamination in the central invariant mass region, where the studies are performed (i.e. $80 < m_{ee} < 100$, see below), is at the level of 0.5% and assumed to be negligible (see Section 8.4).

Efficiency of the trigger is evaluated from a ratio of number of *Probes* passing a given trigger to all selected *Probes*:

$$\epsilon_{trigger} = \frac{N_{probes\_passed\_trigger}}{N_{all\_probes}} \tag{5.1}$$

The trigger efficiency was evaluated at different levels of electron identification criteria, *ie* Medium(++) and Tight(++).

Electron trigger efficiency is highly dependent on the kinematics of the electron, therefore the efficiencies and SFs are measured as a function of electron pseudorapidity η and electron transverse momentum p_T.

For the purpose of the following efficiency calculations, 2011 *ATLAS* data (period $D-M$) and $Z/\gamma^* \to e^+e^-$ MC signal sample generated with PYTHIA6[1] are used. The common selection[2] include events from the standard *Good Run List* (GRL) and are "good" *Object Quality*. Problematic regions of the LAr calorimeter are excluded from analysis (noise burst cut). The primary vertex is required to have at lest three associated tracks, and so-called *author electrons* (1 or 3) are selected. The therm *author* refers to the algorithm used to reconstruct a particular electron. *Author==1* represents the object that has been found by the cluster based algorithm (i.e. standard *egamma* algorithm, as described in Section 4.1.1) only, while *author==3* stands for the electron reconstructed by the standard, as well as the track-based algorithm simultaneously. For more details, please refer to Section 7.3.

[1]Please refer to Chapter 6 and Table 6.1 for more details.
[2]For a detailed description see Section 7.2.

5.3 Single Electron Trigger Efficiency

In order to calculate a single electron trigger efficiency, the tag electron is first selected among offline reconstructed electron candidates, and required to match an online electron passing the single electron trigger ($e20\_medium$, $e22\_medium$ or $e22vh\_medium1$ - depending on luminosity) at all trigger levels (i.e. at L1, L2 and EF). The matching is performed in the (η, ϕ) space, within the cone of $\Delta R < 0.15$, where $\Delta R = \sqrt{(\Delta\eta)^2 + (\Delta\phi)^2}$. The tag electron is subject to additional selection cuts, including $p_T > 25\ GeV$, and $tight{+}{+}$ identification. The tag electron has to be reconstructed within $|\eta| < 2.47$, excluding $1.37 < |\eta| < 1.52$, corresponding to a transition region between the barrel and the end-caps, as well as $1.60 < |\eta| < 1.70$ region of low efficiency (see Section 7.3 for more details). The second electron, with a $p_T > 20GeV$ is considered as a probe, if it forms an invariant mass with a tag, in the range of $80 < m_{ee} < 100\ GeV$, and has an opposite electric charge.

The single electron trigger efficiency is defined as a ratio of probes matching in ΔR an online electron, that pass the trigger selection, to all selected probes.

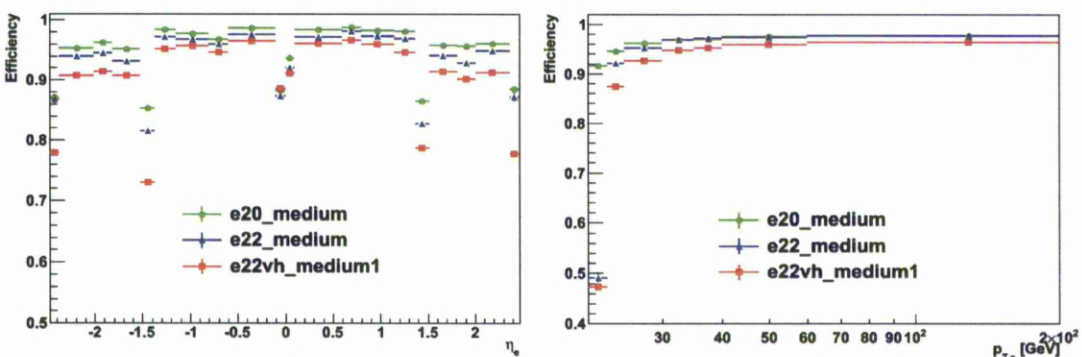

(a) (b)

Figure 5.1: Trigger efficiencies calculated with respect to medium(++) electron selection, and presented as a function of η (a) and p_T (b) of the electron.

Approximately $1.8[fb^{-1}]$, $0.6[fb^{-1}]$, and $2.5[fb^{-1}]$ of the ATLAS data were

recorded, when the main single electron triggers for physics analysis were *e20_medium*, *e22_medium*, and *e22vh_medium1* respectively.

The efficiencies of the *e20_medium*, *e22_medium*, and *e22vh_medium1* triggers, calculated in data with respect to the *medium++* electrons, and presented as a function of η and p_T of the electron, are shown in Figure 5.1.

In general the single electron trigger performance is high, with inefficiencies arising mainly from the resolution of reconstruction and identification variables at the high level trigger. Reconstruction algorithms implemented in the *HLT*, and especially the tracking algorithm at *L2*, do not correspond at the level of sophistication to the offline algorithms, due to time constraints related to the online processing. Moreover the offline electron identification is related to certain limitations, which also affect the trigger performance. This is particularly visible for the *e22vh_medium1* trigger. It involves a tighter selection criteria and a larger number of variables, comparing to the *e20_medium* and *e22_medium* triggers, and its performance is most affected.

5.4 Di-electron Trigger Efficiency

The efficiency of a di-electron trigger, for events with two identified electrons, is defined as a product of a single trigger efficiency for each of the two electrons, and measured as a function of a given offline parameter:

$$\epsilon^{double}_{trigger}(\eta_{(e_1,e_2)}, p_{T(e_1,e_2)}, ...) = \epsilon^{single}_{trigger}(\eta_{(e_1)}, p_{T(e_1)}, ...) \cdot \epsilon^{single}_{trigger}(\eta_{(e_2)}, p_{T(e_2)}, ...) \quad (5.2)$$

where the $\epsilon^{single}_{trigger}$ is calculated equivalently to Section 5.3. The tag electron, is selected with *medium++* identification criteria, and match an online electron, passing the single electron trigger selection (*e20_medium*, *e22_medium* or *e22vh_medium1* - depending on luminosity) at all trigger levels (i.e. at L1, L2 and EF). The $\epsilon^{single}_{trigger}$ efficiency is defined as a ratio of probes matching in $\Delta R < 0.15$ an online electron, that pass the trigger selection (*e12_medium*, *e12T_medium* or

$e12Tvh\_medium$), to all selected probes. The efficiencies were calculated with respect to the probe electrons identified with either *medium++* or *tight++* selection criteria.

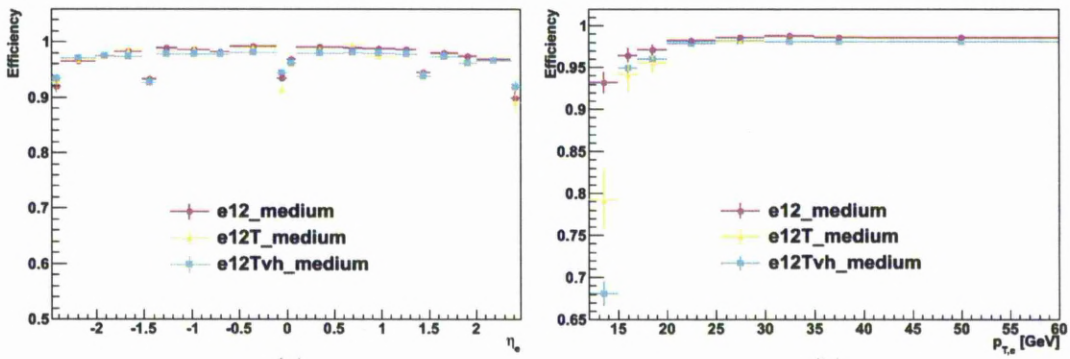

(a) (b)

Figure 5.2: Trigger efficiencies calculated with respect to tight++ electron selection, and presented as a function of η (a) and p_T (b) of the electron.

The efficiencies of the $e12\_medium$, $e12T\_medium$, and $e12Tvh\_medium$ triggers, calculated in data with respect to the *tight++* electrons, are shown in Figure 5.2, as a function of η and p_T of the electron. At the efficiency plateau all triggers follow a similar profile and show a very high performance, reaching $97 - 99\%$. From Figure 5.2(b) it is visible that the efficiency plateau is reached by all three triggers at about 23 $[GeV]$.

The sources of systematic uncertainty related to the trigger efficiency measurements with the *Tag and Probe* technique, include the selection of the *Tag* electron, the size of the invariant mass window of the electron pair, as well as the size of the ΔR cone considered in the trigger matching procedure. The total systematic uncertainty on this measurement is typically small, details are included in [58].

5.4.1 Scale Factors

The scale factors are obtained from comparison of the data calculated trigger efficiencies to the one acquired from the Monte Carlo predictions, and defined as a ratio of data to MC. Figure 5.3 shows comparison of *e20_medium* trigger efficiencies obtained from data and simulated $Z \rightarrow ee$ events. Both distributions are in a good agreement, but MC simulation tends to overestimate the trigger efficiency.

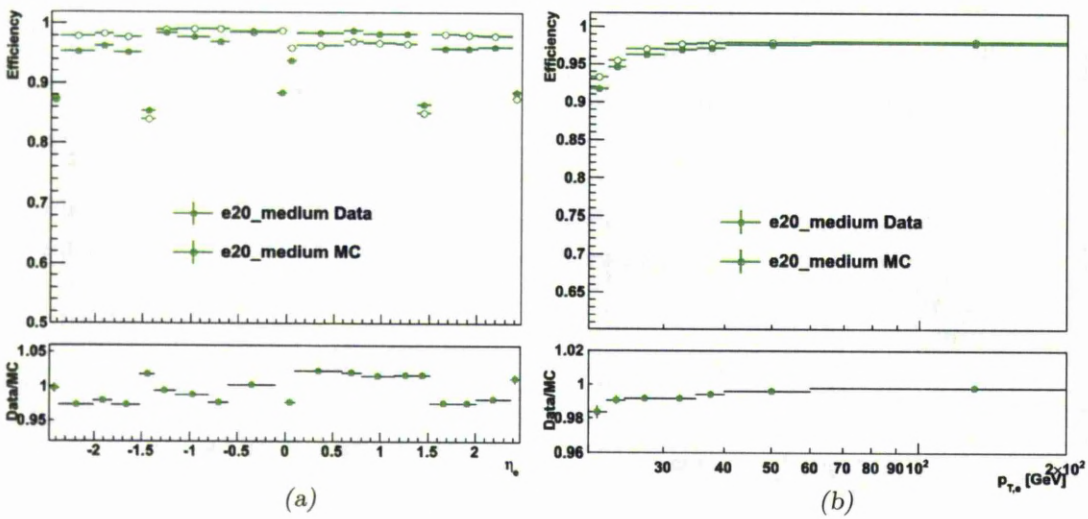

(a) (b)

Figure 5.3: Comparison of e20_medium trigger efficiency obtained from data and MC simulation, with respect to the medium electron selection. Efficiency as a function of η (a) and p_T (b) of the electron is presented.

Chapter 6

Data and Monte-Carlo Samples

This chapter describes data (Section 6.1) and Monte Carlo generated (Section 6.3) samples used in analysis presented in this Thesis. Section 6.2 provides a brief specification of the main Monte Carlo events generators, while the last section (Section 6.4) details the global corrections applied to MC samples, resulting from the differences between data and simulation.

6.1 Data Sample

The analysis is based on the proton-proton collisions data at $\sqrt{s} = 7\ TeV$ collected by the ATLAS experiment during 2011. The data are divided into sub-periods (B-M), reflecting changes in data taking conditions, such as luminosity, different trigger menus or detector's operational status. During 2011 data-taking period the LAr Calorimeter had a several minor problems with respect to the Front End Boards (FEBs), noise bursts or dead/noisy single cells. In order to select events that were collected during the time when the ATLAS sub-detectors, essential to this analysis, were operating properly, the ATLAS WZ common *Good Run List* (GRL) (`data11_7TeV.periodAllYear_DetStatus-v36-pro10_CoolRun Query-00-04-08_WZjets_allchannels_DtoM.xml`) is used. Moreover to reject a bad quality or fake clusters originating from calorimeter problems, additional cuts, like a noise burst ($LArError = 2$) and *Object Quality* cuts, are applied

[71]. The sub-periods D-M are considered in the final analysis, providing a total integrated luminosity of $\mathcal{L} = 4.64\ fb^{-1}$ with a systematic uncertainty of 1.8% [72, 73].

6.2 The Monte-Carlo Event Generators

The purpose of a high energy physics generators [74, 75] is to combine the theoretical predictions for a given process, in order to produce events imitating the one obtained in a real experiment. The simulation of extremely complex final states involving a large number of particles is accomplished by using a tool of factorization. It allows separation of interesting processes, with respect to the scale of momentum transfer involved, and their independent consideration. In particular case of the LHC collisions, the Monte Carlo generators implement description of the hadrons structure, the parton showers, the hard scattering process and the hadronization. The MC event generators often use different approaches and approximations for the calculations of these steps, and therefore the theoretical predictions obtained from MC simulations are to some extent dependent on the choice of the MC generator. There are specialised generators dedicated to a particular step of event simulation, as well as the multi-purpose one, able to govern all aspects of factorisation. It is often beneficial to combine components of different programs, depending on the process of interest (eg. POWHEGPYTHIA6 used to generate $Z \rightarrow ee$ events, where the PYTHIA6 generator provides parton showers and PHOTOS simulate the effect of QED final state radiation), in order to obtain the most accurate theoretical predictions.

There are many Monte Carlo generators available for the purpose of LHC physics. The one used to generate the samples relevant to this analysis will be shortly discussed in the following sub-sections.

6.2.1 Pythia

PYTHIA [76] is a general purpose event generator, able to simulate lepton-lepton, lepton-hadron and hadron-hadron interactions within a broad range of theoretical models. Its versatility and reliability, as well as ease of handling, make it a popular choice in HEP physics. The hard scattering process is calculated in leading-order (LO) approximation, while the higher-order corrections are approximated with the parton shower approach, characterised by a limited accuracy for predicting events with higher jet multiplicity. The simulation of hadronisation process is based on the Lund string model [77], where stable and unstable hadrons are generated and the unstable ones decay into stable particles according to their branching ratios. In the case of certain particle decays, different models are also available and used by a dedicated generators, and their output is combined with PYTHIA, to provide predictions as accurate as possible. As an example the input from TAUOLA (Section 6.2.6) package used to simulate τ lepton decays including spin information, can be given. For the calculations of QED bremsstrahlung PHOTOS generator is used (Section 6.2.5).

6.2.2 Herwig

Similar to PYTHIA, HERWIG (Hadron Emission Reactions With Interfering Gluons) [78] is also a general purpose generator, able to simulate lepton-lepton, lepton-hadron and hadron-hadron collisions. This include calculations of various hard scattering processes, angular-ordered parton showers, hadronisation and underlying event simulations. The main differences between the two generators arising from approach to the parton shower and the hadronisation process generation. HERWIG uses an angular-ordered shower for initial and final state radiation, while the hadronisation process is based on the cluster fragmentation model [79]. It is also possible to interface HERWIG with other specialised generators like PHOTOS or TAUOLA to simulate complex particle decays. Moreover to

generate multiple parton scattering events in hadron-hadron, photon-photon or photon-hadron events, the JIMMY [80] generator is used, which is a package that should be linked to HERWIG and HERWIG based generators.

6.2.3 Powheg

POWHEG [81, 82, 83, 84] is a specialised MC generator which calculates the hard scattering process up to next-to-leading order (NLO) in QCD. It can be interfaced with a shower generator (as PYTHIA or HERWIG), so that the LO accuracy of the parton shower and NLO accuracy of the hard process are both supported.

6.2.4 Mc@Nlo

MC@NLO [85] is a generator similar to POWHEG, including the full NLO QCD corrections in calculation of the hard scattering process. The output of the simulation is further managed by a multipurpose generator (usually HERWIG), which provides the parton shower and the hadronisation.

6.2.5 Photos

PHOTOS [86] algorithms generate QED radiative corrections to particle decays. It is used in conjunction with a host Monte Carlo generator, which provides information about the topology of the process and the four-vectors of particles involved. Versatile PHOTOS algorithm uses this information to generate bremsstrahlung photons with a given probability and with respect to every event, which are then included in the fraction of already existing events and kinematic configurations are modified to ensure the energy-momentum conservation. The double-counting is avoided by excluding QED effects from a host generator (in HERWIG by default, in PYTHIA by setting an internal PARJ(90) [87] parameter to $2 \cdot 10^4$, i.e. the threshold in GeV below which leptons do not radiate).

6.2.6 Tauola

TAUOLA [88] is a MC package dedicated to simulate decays of polarised τ leptons, constructed in such way, that it can be easily interfaced with a several generating programs. For each decay mode an individual phase space generator, a separate weak and hadronic current description, as well as a part responsible for the choice of the τ lepton decay mode and the overall administration, is provided. TAUOLA is often used in combination with PHOTOS, as per recommendation.

6.3 Monte-Carlo Samples

A number of Monte Carlo samples (production MC11c) performed using full detector simulation and reconstruction in the version 17.0.X of the ATLAS *Athena* software, is used in presented analysis to calculate acceptances and study both signal and background processes. The full ATLAS detector simulation is based on GEANT4 [89]. The multiple proton-proton interactions per bunch crossing ("pile-up") are also considered in the simulation, so that the original hard-scattering event is overlayed with the minimum bias events generated with PYTHIA6.

The primary signal sample of $Z/\gamma^* \rightarrow e^+e^-$ events, available with a high statistics is generated with POWHEG event generator, where the parton showers are provided by PYTHIA6. The additional signal samples, produced with the MC@NLO and POWHEG both showered by HERWIG, are used for the study of systematic effects related to the choice of the event generator. Moreover signal samples produced with the PYTHIA6 generator has been exploited in some aspects of the efficiency studies. The background processes taken into account are simulated either with PYTHIA6, POWHEG or HERWIG. In order to simulate the effect of QED final state radiation, the PHOTOS program was used in the case of all generators, while τ decays are simulated by TAUOLA.

The PYTHIA6 and HERWIG generators employ MRST *LO** [90] parton distribution functions (PDFs), while for the POWHEG and MC@NLO the CT10

NLO PDF set [23] is used.

Overview of all data sets used for the analysis, together with their official data set number and basic properties is provided in Table 6.1. The cross-sections specified in the table are used to normalise estimates of the expected number of events in the distributions obtained with these MC samples [1]. The samples of EW processes ($Z \to ee$, $W \to e\nu$, $W \to \tau\nu$, $Z \to \tau\tau$) are normalised to next-to-next-to-leading-order (NNLO) cross-sections, where the calculations are provided by the FEWZ program using the MSTW 2008 [26] PDF set and published in [91]. In the case of signal $Z \to ee$ samples produced in various mass ranges, the cross-section provided by the generator multiplied by the k-factor valid for the $m_{ee} > 60$ GeV range, is used. The uncertainties on cross-sections arise from the choice of PDF, from factorisation and renormalisation scale dependence, and the size of the correction from NLO to NNLO. The total uncertainty of 5% and 7% is assumed for the single and di-boson samples respectively.

The $t\bar{t}$ cross section of $165pb$ was calculated at $m_t = 172.5GeV$ with a total uncertainty of $+7\%$ and -10% (from [92, 93, 94]).

6.4 Global Reweighting of Monte-Carlo Samples

The production process of Monte Carlo samples is separated into periods, in a similar way to a real data acquisition, taking into account specific detector conditions, pileup and trigger settings present during 2011 data taking period. In general MC tends to describe data in an appropriate way, but also several minor inaccuracies are present, which need to be corrected at the analysis level. This involves application of the relevant weights to the truth MC information, and validation of their effects at the reconstruction stage.

[1] Except for the JF17 (QCD) samples, where the cross-section is taken directly from the PYTHIA6 generator; provided only for completeness and not used in the analysis.

PhysicsProcess	*Comment*	*DataSet*	*Generator*	$\sigma \cdot BR \cdot \varepsilon_{filter}$ [nb]	*Number of Events* $\times[10^6]$
$Z/\gamma^* \to e^+e^-$	($m_{ee} > 60$ GeV)	106046	PYTHIA6	0.990	10
$Z/\gamma^* \to e^+e^-$	($15 < m_{ee} < 60$ GeV)	108320	PYTHIA6	1.462	2
$Z/\gamma^* \to e^+e^-$	($m_{ee} > 53.8$ GeV)	108303	POWHEGPYTHIA6	1.006	20
$Z/\gamma^* \to e^+e^-$	($38 < m_{ee} < 53.8$ GeV)	129806	POWHEGPYTHIA6	0.0878	1
$Z/\gamma^* \to e^+e^-$	($m_{ee} > 53.8$ GeV)	126006	POWHEGHERWIG	1.006	5
$Z/\gamma^* \to e^+e^-$	($38 < m_{ee} < 53.8$ GeV)	129808	POWHEGHERWIG	0.0878	1
$Z/\gamma^* \to e^+e^-$	($53.8 < m_{ee} < 75$ GeV)	147219	POWHEGHERWIG	0.04713	1
$Z/\gamma^* \to e^+e^-$	($m_{ee} > 105$ GeV)	147220	POWHEGHERWIG	0.02464	0.5
$Z/\gamma^* \to e^+e^-$	($m_{ee} > 60$ GeV)	106087	MC@NLO	0.990	5
$Z/\gamma^* \to e^+e^-$	($40 < m_{ee} < 75$ GeV)	147215	MC@NLO	0.1151	2.5
$Z/\gamma^* \to e^+e^-$	($m_{ee} > 105$ GeV)	147216	MC@NLO	0.02418	0.5
$W^+ \to e^+\nu_e$		108297	POWHEGPYTHIA6	6.160	23
$W^- \to e^-\bar{\nu}_e$		108300	POWHEGPYTHIA6	4.300	17
$W \to \tau\nu_\tau$		107054	PYTHIA6	10.460	1
$Z/\gamma^* \to \tau^+\tau^-$	($m_{\tau\tau} > 60$ GeV)	106052	PYTHIA6	0.989	3
$t\bar{t}$		105200	MC@NLO	$(0.165^{+7\%}_{-10\%}) \cdot 0.56$	1.5
WW		105985	HERWIG	$44.9 \cdot 0.389 \cdot 10^{-3}$	1.5
WZ		105987	HERWIG	$18.5 \cdot 0.310 \cdot 10^{-3}$	1
ZZ		105986	HERWIG	$6.02 \cdot 0.212 \cdot 10^{-3}$	0.25
$JF17$	*Dijet* ($\hat{p}_T > 15$ GeV)	105802	PYTHIA6	$1.15 \times 10^6 \cdot 0.085$	10
$JF17$	*Dijet wgt* ($\hat{p}_T > 15$ GeV)	106009	PYTHIA6	$1.15 \times 10^6 \cdot 0.085$	5

Table 6.1: Summary of the Monte Carlo samples used. The columns list both the signal and background samples, indicating the generators used in the production process, together with the official data set number denoting the process, as well as the amount of available events. For each sample the cross section times the branching ratio, to which the estimates are normalised, multiplied by the efficiency of a filter applied on the final state particles, $\sigma \cdot BR \cdot \varepsilon_{filter}$*, is quoted.*

6.4.1 Vertex Reweighting

The beam spot position in x, y and z direction is represented by a Gauss function, which is also included in the MC simulation. However comparison of data and MC revealed discrepancy in an exact position and width of the modelled z_{vtx} distribution, which requires a corrections (weights) to be applied. The weights are evaluated from the data/MC ratio and adopted to the generated events, where the hard interaction provides an information on the z coordinate. All MC samples used in the analysis are reweighted using the `VertexPositionReweightTool` available from `egammaAnalysisUtils`. The z_{vtx} distribution in MC simulation before and after reweighting, as well as a shape observed in data is shown in Figure 6.1.

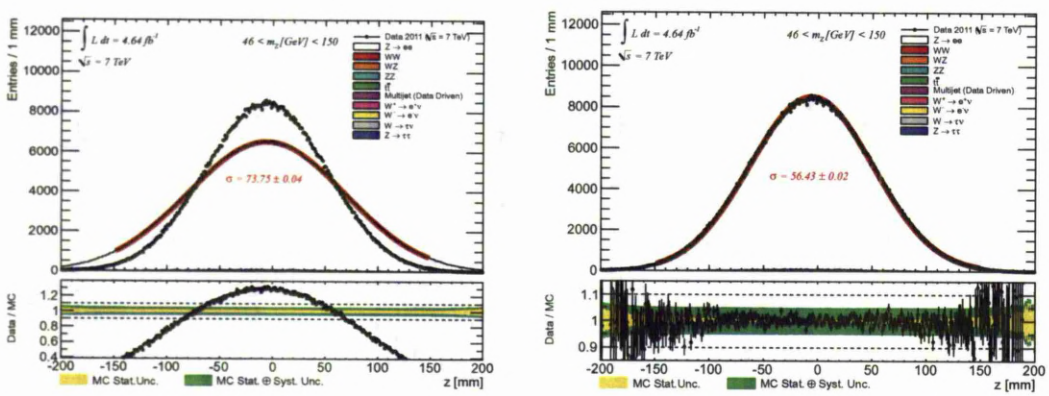

Figure 6.1: Comparison of z_{vtx} distribution from data and MC, where MC before (left hand side) and after reweighting (right hand side) is presented.

6.4.2 Pileup Reweighting

To take into account effects of multiple interactions per bunch crossing (pileup) the MC samples (MC11c) are simulated according to the μ distribution, as measured in each data period, by overlaying the original hard scattering event with the simulated minimum bias events. Since the pileup modelling manifests residual differences, a reweighting as a function of μ is performed by using the

`PileupReweightingTool` [95]. Shown in Figure 6.2 are the distributions of the number of average interactions per bunch crossing $\langle\mu\rangle$, and number of primary vertices N_{vtx} with at least three reconstructed tracks, where the selection cuts and reweightings have been applied.

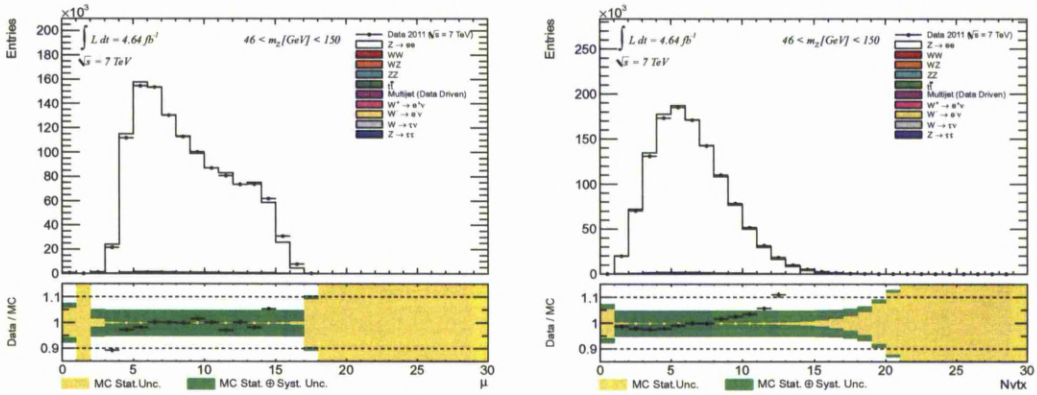

Figure 6.2: On the left hand side the distribution of the number of average interactions per bunch crossing is shown. On the right hand side the distribution of the number of primary vertices is presented. Both distributions are plotted after selection cuts and weights applied.

6.4.3 Z Boson p_T Reweighting

The previous studies [96, 3] shown that the predictions of Z boson p_T spectrum obtained from the main signal generators used in this analysis are not fully compatible with a distribution observed in data. The disagreement is especially apparent in the low p_T region. Although this mismodelling has a limited impact on the cross-section studies performed here, the PowhegPythia6, PowhegHerwig and Mc@Nlo generated signal samples have been reweighted using `BosonPtReweightingTool` from the `egammaAnalysisUtils` package.

6.4.4 Z Boson Line Shape Reweighting

Recent studies [97] have found, that a large diversity in the electroweak parameters' settings implemented in MC generators lead to anomalous discrepancies in

some of the key kinematic distributions, including the lineshape of the Z boson resonance. Different MC generators use various approach when including the basic EW properties like the mass and width of the boson, method for the resonace parametrisation, or the choice of the coupling constants. This leads to the inconsistency in the parameter definitions across generators used in this analysis. The LineShapeTool (from the ATLAS svn) is used to analytically reweight this various predictions to the common *Improved Born Approximation*, in order to address the boson lineshape divergence. This tool is exploited to correct all the samples used in the analysis, and the performance of the lineshape reweighting is shown in Figure 6.3, where the ratios of PYTHIA6 to other MC generated M_{ee} distributions, before and after reweighting are plotted. As an example, the MC generators used in the main analysis are exploited, i.e. POWHEGPYTHIA, POWHEGHERWIG and MC@NLO.

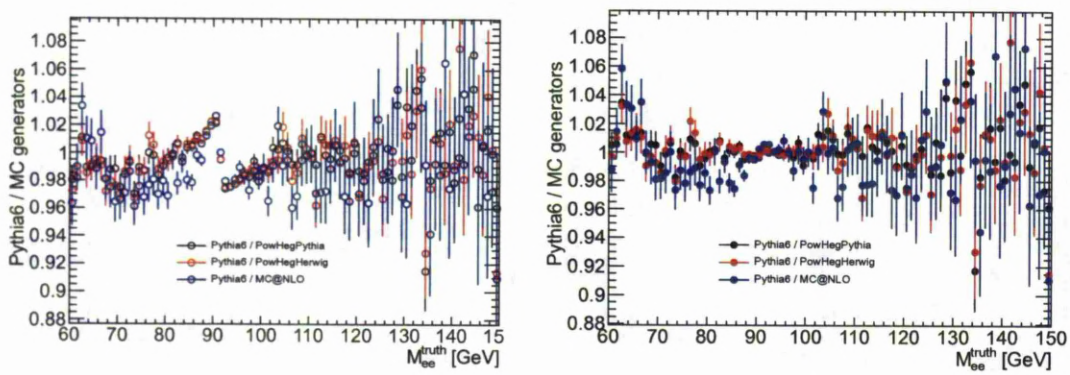

Figure 6.3: The ratios of the PYTHIA6/POWHEGPYTHIA, PYTHIA6/POWHEGHERWIG *and* PYTHIA6/MC@NLO *generated* M_{ee} *distributions before (left hand side) and after (right hand side) application of the lineshape reweighting.*

Chapter 7

Event Selection

A set of tailored cuts, optimised for an effective background rejection performance, is applied to yield a sample of high-quality electron candidates originating from $Z/\gamma^* \rightarrow e^+e^-$decays. Following chapter introduces the specific criteria used to identify the Z boson events, and presents results of their application.

7.1 Electron Energy and Direction Definition

To calculate the basic electron kinematic variables some assumptions have been made and rules following the official *egamma* group recommendations [98] are applied. The electron four-vectors are calculated using an information from the electromagnetic cluster and the corresponding track. In particular the energy (E) of the cluster, the η and ϕ directions from the track, and the zero electron mass are taken into account. In the case when the track has less then four silicon hits, the cluster information is used. However that kind of TRT only tracks do not pass the *Medium++* identification criteria (see Section 4.2) and are not included in the cross-section measurements presented here. In order to apply all calorimeter-related cuts and bins (η requirement, crack region removal, etc.), as well as the efficiency or energy scale corrections, the cluster coordinates are used.

Trigger	*DataPeriod*	*IntegratedLuminosity*$[fb^{-1}]$
2e12_medium	D-J	1.68
2e12T_medium	K	0.59
2e12Tvh_medium	L-M	2.43

Table 7.1: Di-electron trigger listed with respect to the different data taking periods. The integrated luminosity (in $[fb^{-1}]$) for a given period is also quoted.

7.2 Basic Event Selection

A successful event selection is characterised by a well balanced proportion of identified signal candidates to the amount of rejected background. The events included in the standard *Good Run List* (GRL - see Section 6.1), which ensures stability of the beam parameters and that the sub-detectors crucial for the electron analysis were in their nominal conditions during the data taking periods, are considered. Events affected by LAr noise burst are excluded with *larError* > *1* cut and the quality of the *egamma* object is checked, using the *Object Quality Flag* implemented in the Athena framework. *Object Quality* cut eliminates electrons with problematic clusters, mainly caused by the presence of a dead Front End Boards (FEB) or by the dead/noisy cells.

The presence of a primary vertex with at least three associated tracks is required in every event, in order to reject a non-collision background. The events are selected by the di-electron trigger. The type of the trigger used depends on the data taking period, as specified in Table 7.1.

7.3 Kinematic Selection and Further Requirements

Further event selection includes identification of good electrons, which are then combined to form a Z boson candidate. For each object information about the algorithm involved in its reconstruction is stored in the *author* variable. To fulfill

	$Z/\gamma^* \to e^+e^-$ *Selection*
Collision Event	*Good Run List* (GRL)
	Primary vertex with reconstructed $N_{tracks} \geq 3$
	Noise burst rejection with $larError > 1$
Trigger	Data period dependent trigger (see Table 7.1)
Electron Selection	*Object Quality (Good Electrons)*
	Electron author 1 or 3
	Medium++ identification
	$p_T > 20$ GeV
	$\|\eta\| < 2.47$ excluding $1.37 < \|\eta\| < 1.52$ and $1.60 < \|\eta\| < 1.70$
Event Selection	Two identified electrons
	Opposite sign charge

Table 7.2: Summary of the event selection criteria.

the further requirements, event must contain two electrons reconstructed with the standard *egamma* algorithm (described in Section 4.1), denoted as *author* == 1. As ATLAS uses two algorithms to reconstruct electrons in the central region of the experiment (the second one dedicated mostly to low p_T electrons and seeded by a track in the ID), it is possible that a given electron candidate is found by the two algorithms simultaneously. In this case, when the track is common to a candidate soft-electron and a standard *egamma*, then the objects are regarded to be the same and have *author* == 3. Those electrons are also considered in the further selection.

Electron candidates passing identification criteria at the *Medium++* level (as detailed in Section 4.2) are required to have $E_T > 20\ GeV$, be of the opposite charge, and fall in the kinematic region of $\eta < 2.47$. The transition region between the barrel and end-cap calorimeters, corresponding to $1.37 < |\eta| < 1.52$ is excluded from analysis.

The comparison of η distribution in data and MC shows major discrepancy in a very small end-cap region $|\eta| = 1.65$–1.70, which can be seen in Figure 7.1. This

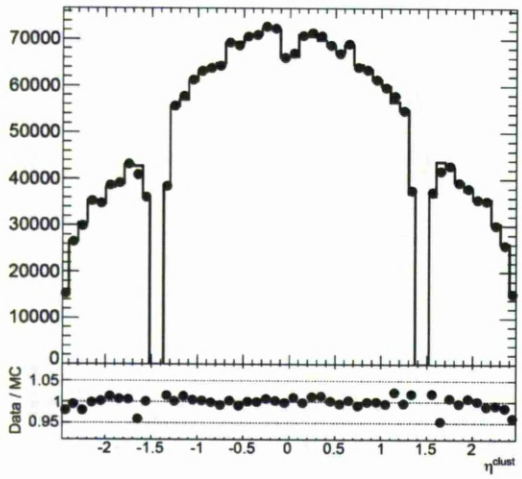

Figure 7.1: Electron $\eta^{cluster}$ distribution obtained from data (points) and MC (histogram). Due to the observed inefficiency in the small end-cap region corresponding to $1.6 < |\eta| < 1.7$; electron is considered in the analysis if it is reconstructed in one of the following $|\eta|$ intervals: $|\eta| < 1.37$ or $1.52 < |\eta| < 1.60$ or $1.70 < |\eta| < 2.47$ [1].

inefficiency is probably due to the combination of some material and calibration effects [1][99]. As at the moment this is not fully understood issue, and therefore an additional region of $1.60 < |\eta| < 1.70$ is excluded from analysis. The event selection criteria are summarised in Table 7.2.

7.4 Performance of the Event Selection

Table 7.3 summarises the number of selected $Z/\gamma^* \rightarrow e^+e^-$ candidates remaining after the selection procedure has been applied to data sample. A total of 1152247 candidates pass all criteria in the invariant mass window $66 < m_{ee} < 116\ GeV$, 36364 in $46 < m_{ee} < 66\ GeV$ and 13145 in $116 < m_{ee} < 150\ GeV$.

Selection	ε^{abs}[%]	ε^{rel}[%]
All events (after preselection)	100.00	100.00
Primary Vertex (with ≥ 3 tracks)	99.95	99.95
Veto LAr noise bursts	99.65	99.70
Di-electron trigger	3.96	3.98
excl. $\|\eta\| < 2.47$	3.85	97.16
excl. $1.47 < \|\eta\| < 1.52$	3.34	86.75
excl. $1.6 < \|\eta\| < 1.7$	3.07	92.05
Author electron	3.04	98.76
$p_{\mathrm{T}} > 20$ GeV	2.09	69.00
Object Quality (GOOD)	2.07	98.84
Medium++	1.45	69.92
Opp. charge pairs	1.42	98.15
$46 < M_Z < 66$ GeV	0.04 (36364)	2.98
$66 < M_Z < 116$ GeV	1.34 (1152247)	94.65
$116 < M_Z < 150$ GeV	0.02 (13145)	1.08

Table 7.3: $Z/\gamma^* \rightarrow e^+e^-$ cut flow table with in terms of absolute and relative efficiency for a given criterion, w.r.t. initial number of Z boson candidate events after preselection, ε^{abs}, and relative to the prior selection step ε^{rel} in per cent. In each m_Z bin number of selected events is explicitly tabulated.

Chapter 8

Background Contributions to $Z/\gamma^* \rightarrow e^+e^-$ Signal

An accurate estimation of the amount of events originating from the background processes that pass the selection procedure (specified in Chapter 7) is essential to $Z/\gamma^* \rightarrow e^+e^-$cross-section measurement. In this chapter the background sources to the process of interest and methods of their determination are described. In particular the data driven method employed to the QCD multijet background evaluation is exemplified in Section 8.2.

8.1 Sources of Background

There are several background processes identified as valid for this analysis, and in general they are grouped into two categories, namely electroweak and QCD backgrounds.

Group of the electroweak backgrounds is associated with a real, high p_T and isolated electron production in the event. These events include the semi and fully leptonic decay modes of $t\bar{t}$ pairs, the electroweak boson decays $W \rightarrow e\nu_e$, $W \rightarrow \tau\nu_\tau$ and $Z/\gamma^* \rightarrow \tau^+\tau^-$, where the τ leptons may decay into electrons ($\tau \rightarrow e\nu\bar{\nu}$), as well as di-boson ($WW$, WZ, ZZ) events. The second group includes the multijet events produced in QCD interactions, which are the dominant

source of fake electrons (i.e. jets misidentified as isolated electrons). With respect to various sources of background events, the corresponding Monte Carlo data sets have been generated and described in Section 6.3. The electroweak backgrounds are simulated taking into account each process individually, while the QCD backgrounds are simultaneously included to compose one set, the so-called $JF17$ filtered sample. Nevertheless, despite the fact that the $JF17$ sample contains approximately 10 million events, the large QCD cross section and high electron selection cuts efficiency result in a fact, that these events are not sufficient for a direct estimate of the QCD multijet background in $Z/\gamma^* \rightarrow e^+e^-$events. Therefore, while the electroweak backgrounds are estimated relying entirely on MC produced samples, the QCD background contributions are evaluated using a data-driven technique.

8.2 Data-driven QCD Multijet Background Estimation

The misidentification of jets as isolated electrons gives rise to the background in Z boson production. The two main processes of multijet production can be distinguished. The heavy flavour production of $b\bar{b}$ and $c\bar{c}$, leading to the subsequent decays of b and c quarks, where electrons are typically embedded within hadronic jets and poorly isolated, as well as inflight decays of pions and kaons. The overwhelming cross section of the QCD processes and related large uncertainties, which arise mainly from a limited theoretical understanding, demand the QCD multi-jet background be determined using a data-driven technique.

8.2.1 Isolation Variable

The topology of $pp \rightarrow Z/\gamma^* \rightarrow e^+e^-$ events is characterised by a clean signature, comprised of two, highly energetic and isolated electrons in the final state. Calorimeter variables can be studied to distinguish genuine, isolated electrons

from poorly isolated and fake electrons, which are passing all the identification criteria, contributing directly to the event selection.

The isolated electrons deposit their energy in the narrow cluster localised in the EM calorimeter, while the non-isolated electrons and jets are characterised by an additional energy deposit (due to the presence of accompanying particles) in the immediate proximity of the electron candidate. Therefore the calorimetric isolation variables are introduced, which enable determination of the value of energy deposited in cells surrounding the reconstructed electron clusters, providing grounds for separation of the signal electrons from the background.

It is possible to define a cone with a given radius ΔR, built around the reconstructed cluster of the electron candidate in η and ϕ space, so that the $\Delta R = \sqrt{\Delta\eta^2 + \Delta\phi^2}$. The calorimetric isolation variable $E_T^{cone}(\Delta R)$ is calculated by subtracting the transverse energy of the electron from the total transverse energy deposited in the cone ΔR. In the following the cone size $\Delta R = 0.3$ is used and the corresponding variable is denoted as $E_T^{cone}(0.3)$. To minimise the E_T dependence of the selection, the calorimetric variable normalised to the electron transverse energy $E_T^{cone}(0.3)/E_T$ is investigated.

In general the misidentified electrons originating from the QCD events are characterised by a larger values of the isolation variable, due to a hadronic activity associated with the fake electrons.

Figure 8.1 shows the comparison of the calorimetric isolation variable $E_T^{cone}(0.3)$ distribution obtained from data and Monte Carlo. It is visible, that the shape of the distributions is adequately modeled, but associated with a shift towards the lower energy values. To correct this discrepancy the MC distributions of the isolation variable are shifted by a constant value of 0.4 GeV.

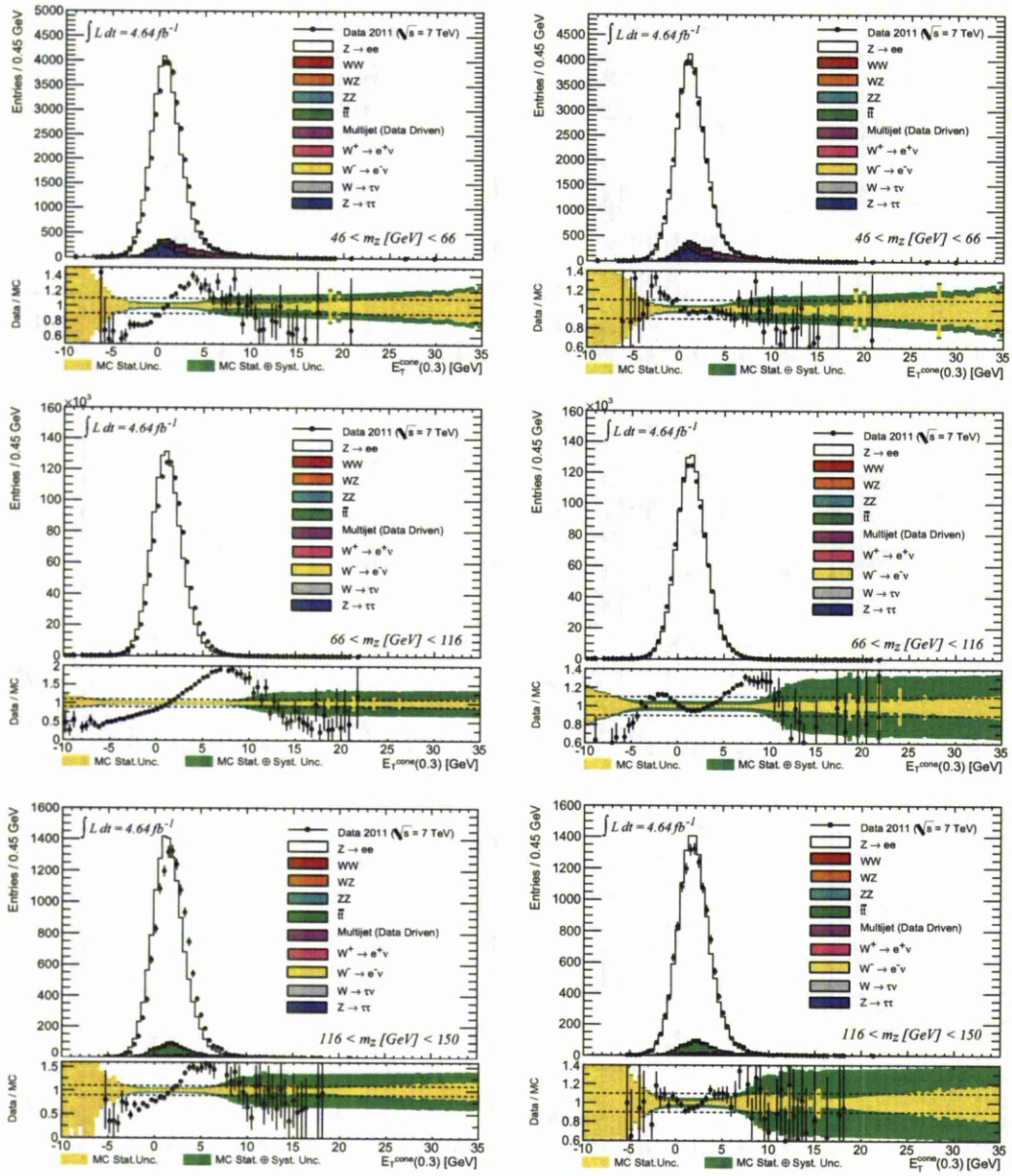

Figure 8.1: Calorimetric isolation variable $E_T^{cone}(0.3)$ distributions used for the data driven multi-jet background estimation. Shown for the three different m_Z intervals. On the right hand side the MC distributions are shifted by 0.4 GeV.

8.2.2 Background Enhanced Selection

To investigate the amount of the multi-jet background passing the selection criteria, a special background enhancing procedure is applied to the data sample, in order to create a template distribution containing a large number of fake electrons. It is obtained by reversing electron identification cuts, allowing the objects imitating electrons to enter the selection. Consequently candidates selected by a di-photon trigger (EF_2g20_loose) and passing the *Loose++* identification criteria, but failing at *Medium++* level, are included, while all the kinematic cuts related to transverse momentum and the geometrical acceptance of the detector remain unchanged and have to be fulfilled. The template selection created in such a way is assumed to have the same shape of the $E_T^{cone}(0.3)$ distribution, as the multi-jet background that survives the original signal selection, but it contains considerably larger amount of events.

8.2.3 Normalisation Procedure

To successfully estimate the QCD background contribution to the signal selection, it is necessary to perform the normalisation procedure, ie. to estimate the scale factor to be applicable to the background enhanced template selection, in order to normalise it to the expected number of multi-jet events that pass the signal selection.

As described in Section 8.2.1, misidentified electrons are usually not well isolated and have a larger values of the isolation variable, than the genuine electrons. Therefore, in order to evaluate the correct scaling for the number of multi-jet template events, the $E_{\mathrm{T}}^{cone}(0.3)/E_T$ distributions for the data events after signal selection, and the multi-jet enhanced selection template are compared in the region, where data starts to deviate from the sum of signal and $EW + t\bar{t}$ described by the Monte Carlo simulation.

As expected, the region of interest dominates the tail of the $E_{\mathrm{T}}^{cone}(0.3)/E_T$

distribution, since for the real electrons there is virtually no transverse energy left in the surrounding ΔR cone, after removal of electron E_{T}. This is not the case for the multi-jet component, where clusters are generally wider, with a lot of hadronic activity remaining.

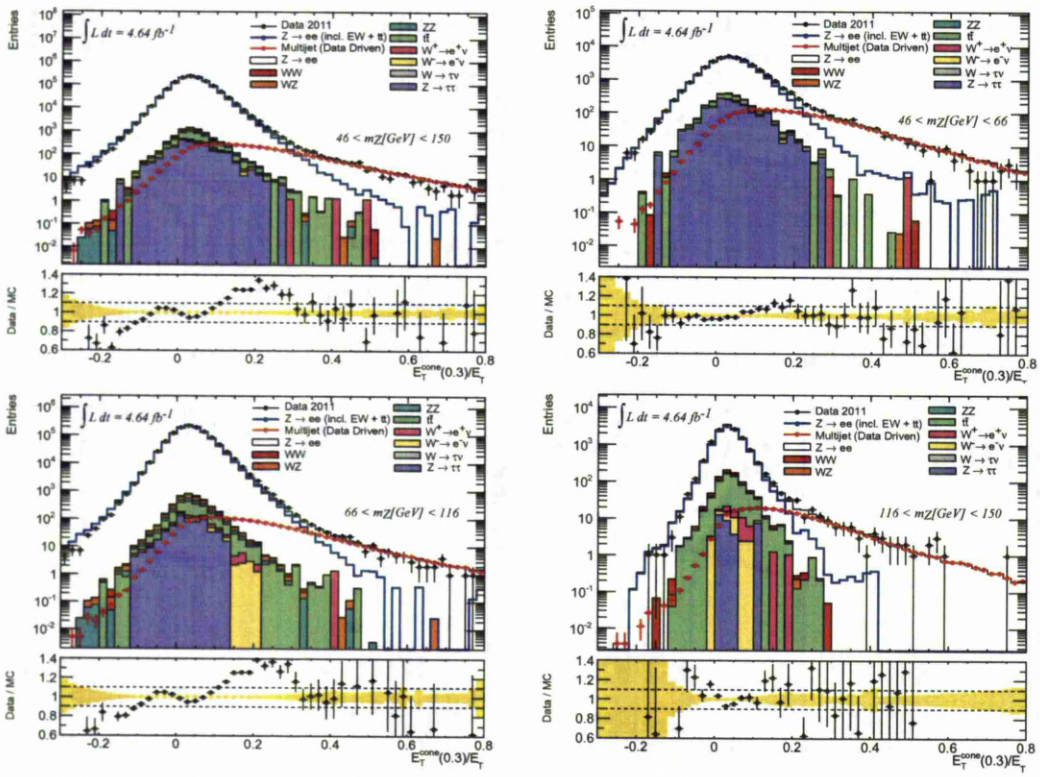

Figure 8.2: Calorimetric isolation variable normalised to the transverse energy $E_T^{cone}(0.3)/E_T$, shown on the logarithmic scale. The distribution in the various m_Z ranges is presented, together with multi-jet data driven template modelled.

Moreover it is observed, that $E_{\mathrm{T}}^{cone}(0.3)/E_T$ spectrum varies between three different m_Z ranges considered, not only in terms of statistics, but also in shape of the measured distribution (see Figure 8.2), which narrows with increasing transverse energy, reflecting close relation to the respective cluster's deposit sizes. The normalisation scale strongly depends on the tail's lower edge position, therefore has to be evaluated over m_Z bins separately. The higher edge is fixed at $E_{\mathrm{T}}^{cone}(0.3)/E_T = 0.61$ to reduce dependance on the very large values of isolation

variable, which might not be well modelled in MC simulation.

The normalisation interval and resulting scale are determined via the two stage iterative procedure:

i. Scaling factor is derived using wide tail interval between 0.05 and 0.61. The logic of the method is depicted on the flow chart (Figure 8.3), and also detailed below.

ii. Resulting multi-jet distribution is summed with signal and remaining backgrounds from Monte Carlo, and compared, within mentioned interval, to the data distribution, via χ^2 identity test [100, 101, 102], i.e. evaluating χ^2 p-value[1] - probability that two histograms represent identical distributions.

In the following iterations consecutive shift (by +0.02) to the lower edge position is introduced until it reaches the upper edge boundary. As may be seen in Figures 8.4, 8.5, 8.6 and 8.7, the result is a scan of the normalisation constant over a high isolation tail together with the measure of the agreement between the data, after signal selection, and modelled multi-jet background. Consequently, fit with the highest p-value defines the normalisation interval and number of multi-jet events.

Figure 8.3 shows the algorithm behind, $scale^{temp}$, Multi-jet template scaling calculation. The reasoning is to equalize the number of multi-jet events seen in a given tail, N_{tail}^{Temp}, with those measured in data, N_{tail}^{Data}, after subtraction of signal, $N_{tail}^{sig,MC}$, and electroweak + $t\bar{t}$ backgrounds, $N_{tail}^{bkg,MC}$ samples. Monte Carlo models for the EW processes used in the study are normalised to the measurement luminosity using NNLO cross section values, with an exception of $t\bar{t}$ which is available at NLO. For a given $E_{\mathrm{T}}^{cone}(0.3)/E_T$ tail the iteration starts with

[1]Please see Appendix for explicit definition of the p-value.

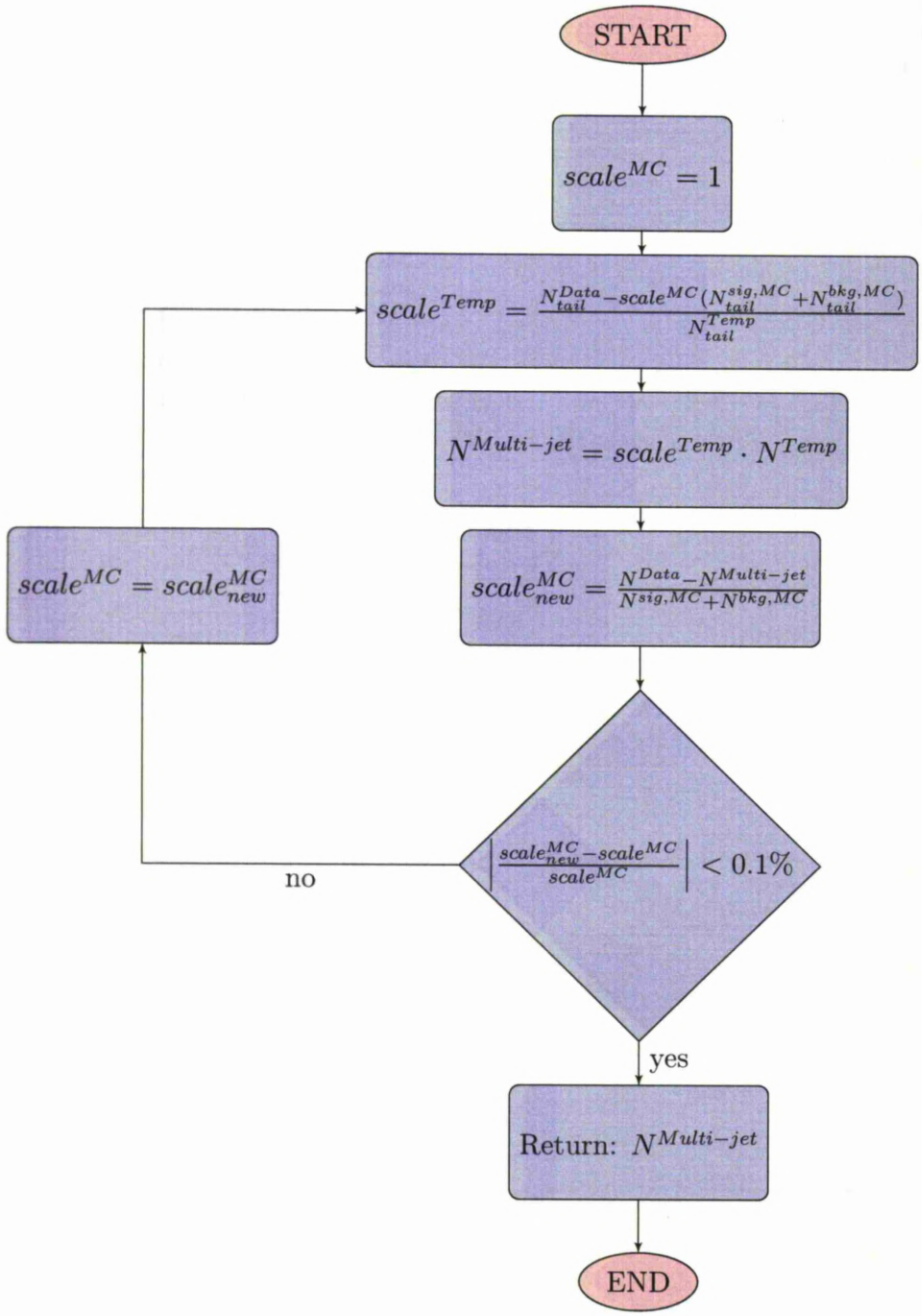

Figure 8.3: Flow chart of an iterative algorithm to determine the scaling for the data-driven Multi-jet template for a given normalization interval. $N^{Data,MC,...}$ denotes number of events in either full or tail of the $E_{\mathrm{T}}^{cone}(0.3)/E_T$ spectrum such: $N = \sum_i w_i$ where w_i is a weight including efficiency corrections for a given Monte Carlo event.

a nominal input for scale applied to Monte Carlo, $scale^{MC} = 1$. What follows, $scale^{temp}$ is defined as a ratio between the number of data events in the tail (subtracting signal and background models) to N_{tail}^{Temp}. Consequently, normalised number of the multi-jet events, $N^{Multi-jet}$, is evaluated by multiplying number of unscaled multi-jet template events, N^{Temp}, with the $scale^{temp}$ (see node 4 in Figure 8.3).

The dependance on the initial normalisation of the Monte Carlo samples is removed by the reevaluation of the scale applied to the Monte Carlo, $scale_{new}^{MC}$, which is measure of agreement between the number of selected data events N^{Data}, subtracting $N^{Multi-jet}$, to those modeled with Monte Carlo for signal, $N^{sig,MC}$, and background, $N^{sig,Bkg}$. Providing, that the change in the normalisation for the Monte Carlo is not significant ($< 0.1\%$) the algorithm converges, with the final value for the number of multi-jet events, $N^{Multi-jet}$, returned in the last iteration. The method is efficient converging most often after (mode) 2 cycles.

It is important to note that in principle the evaluation of the normalisation constant could be performed over each y_z cross-section measurement bin (please refer to Section 9.2), as an extension to one (global) scale, per each m_Z bin. In practise it was found that it is not beneficial, since the systematics suffers from available statistics. The approach did not improve the accuracy of the estimate due to a strong sensitivity to the available data, which is small ($\mathcal{O}(10)$ events in $66 < M_Z < 150$) for the tail $E_{\mathrm{T}}^{cone}(0.3)/E_T$ regions in the high Z rapidity bins.

8.2.4 Systematic Uncertainties

As briefly mentioned in the previous section, the major systematic uncertainty related to the scaling of the multi-jet background arises from the choice of the normalisation interval, in particular the lower edge position. In order to asses the magnitude of the dependance, results of the scan (see Figures 8.4, 8.5, 8.6 and 8.7), with a step of +0.2 applied to the lower edge position, over the ranges of

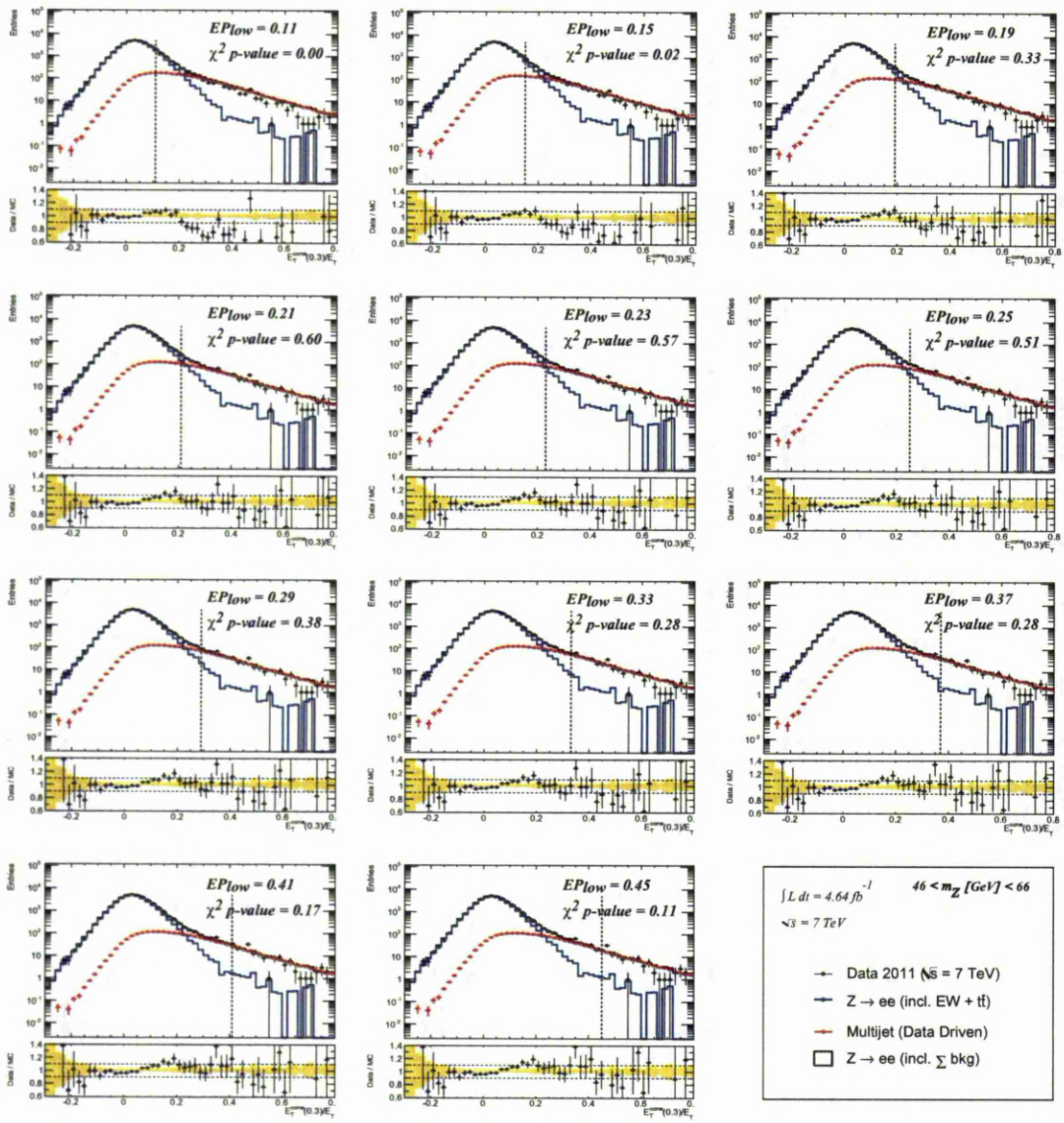

Figure 8.4: Electron isolation distributions used for the data driven Multi-jet background estimation. Selection of plots showing iterative change to the normalisation interval. Performance of the data driven template is confirmed with χ^2 p-value. Shown for the $46 < m_Z < 66$ $[GeV]$ range, where EP_{low} denotes position of the lower edge.

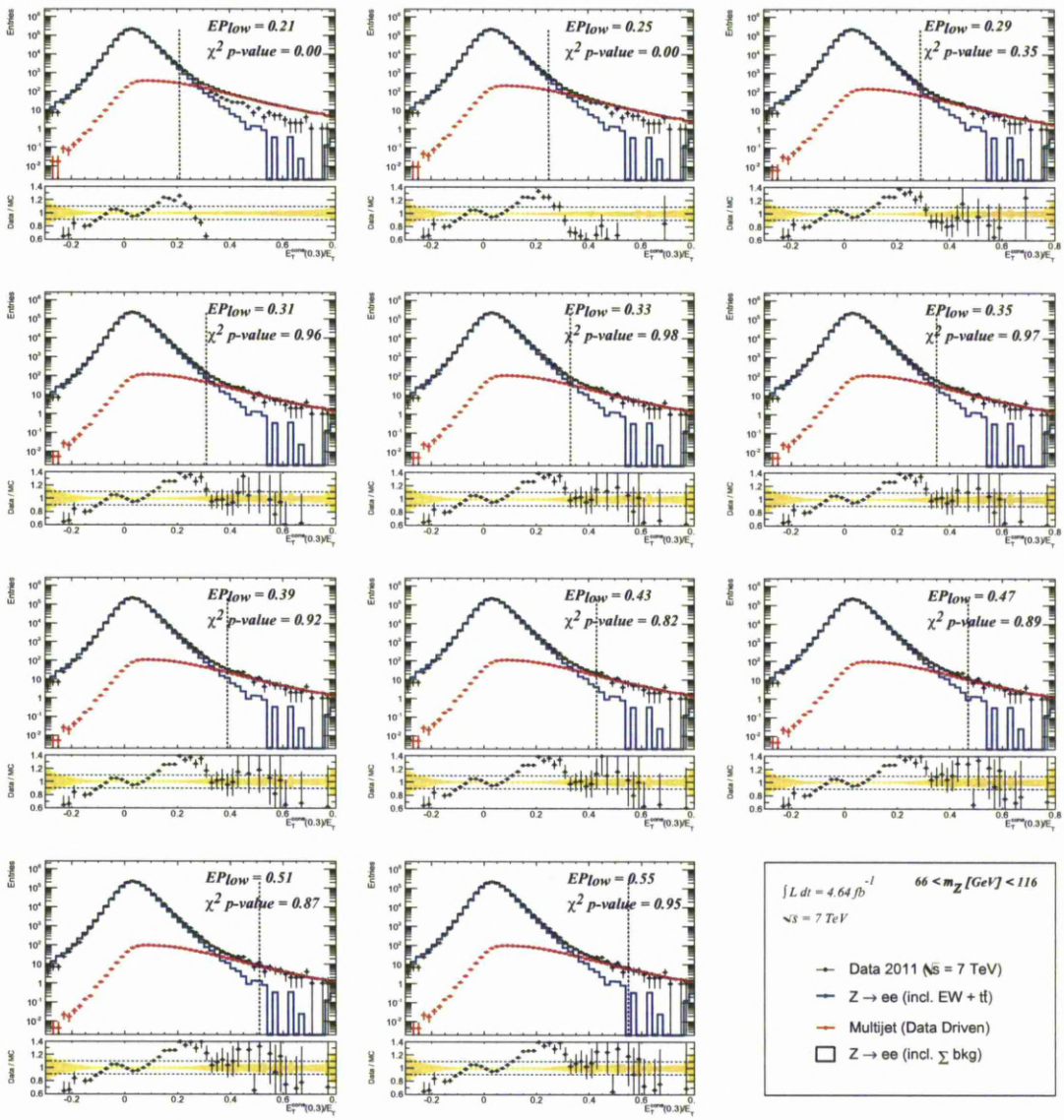

Figure 8.5: Electron isolation distributions used for the data driven Multi-jet background estimation. Selection of plots showing iterative change to the normalisation interval. Performance of the data driven template is confirmed with χ^2 p-value. Shown for the $66 < m_Z < 116$ $[GeV]$ range, where EP_{low} denotes position of the lower edge.

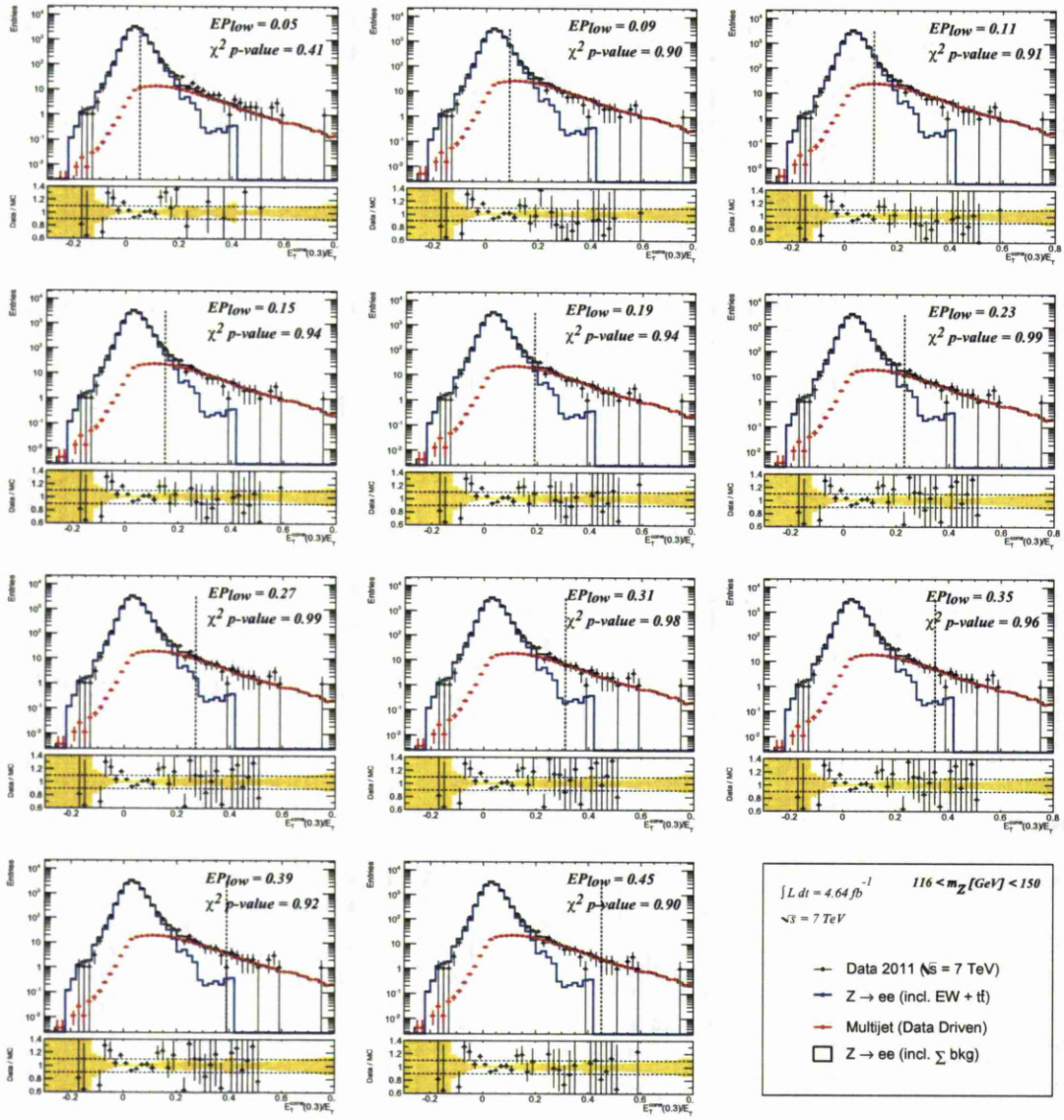

Figure 8.6: Electron isolation distributions used for the data driven Multi-jet background estimation. Selection of plots showing iterative change to the normalisation interval. Performance of the data driven template is confirmed with χ^2 p-value. Shown for the $116 < m_Z < 150$ [GeV] range, where EP_{low} denotes position of the lower edge.

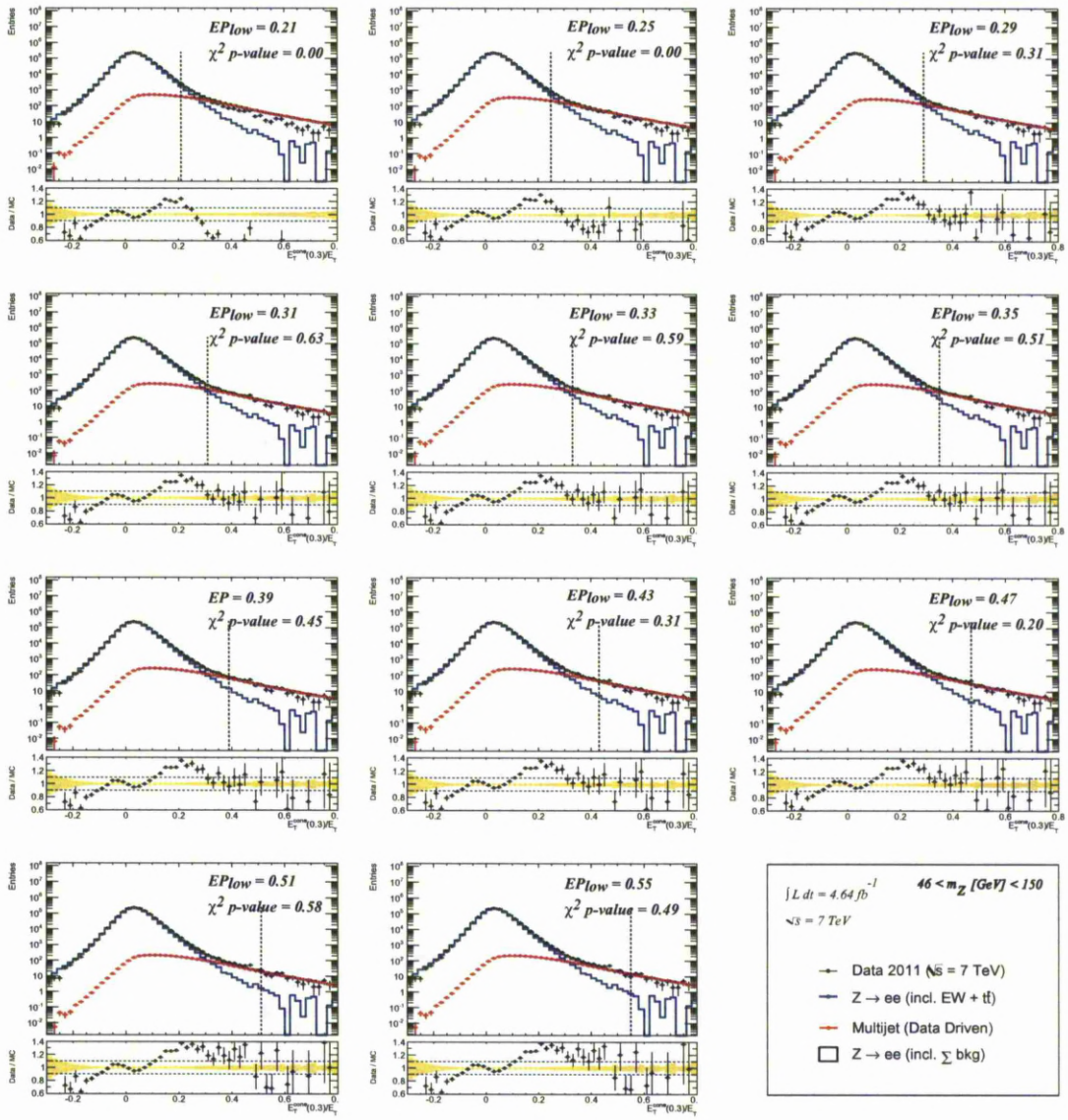

Figure 8.7: Electron isolation distributions used for the data driven Multi-jet background estimation. Selection of plots showing iterative change to the normalisation interval. Performance of the data driven template is confirmed with χ^2 p-value. Shown for the $46 < m_Z < 150$ $[GeV]$ range, where EP_{low} denotes position of the lower edge.

$E_{\mathrm{T}}^{cone}(0.3)/E_T$ tail distributions, were investigated.

As may be seen in Figure 8.8, there is an arbitrary choice for the region, in which systematic variation in estimated $N^{Multi-jet}$ value was performed. The choice of this arbitrary region is motivated by the fact, that since the Monte Carlo simulation and (unbiased) data-driven multi-jet background should describe data perfectly, therefore resulting (estimated) $N^{Multi-jet}$ should, apart from statistical fluctuations, be independent from the choice of the normalisation region.

As a result, estimation of the systematic uncertainty is conducted in the region with relatively flat distribution of $N^{Multi-jet}$, reasonable agreement between the model and data (reflected by χ^2 p-value), and do not suffer from available statistics. The value for the systematic variation is differentiated in the m_Z bins, and also integrated over the entire range. It is conservatively[2] taken as a half of the uncertainty band, where the uncertainty band is defined as a distance between maximum and minimum variation, including statistical fluctuations. Consequently a relative systematic uncertainty of $\pm 14.7\%$ in low ($46 < m_Z < 66$), $\pm 32.1\%$ in central ($66 < m_Z < 116$), $\pm 35.0\%$ in high ($116 < m_Z < 150$) and $\pm 25.1\%$ integrated over entire mass region ($46 < m_Z < 150$) is assumed on the model. The estimated numbers of the Multi-jet events are summarized in tab Table 8.1.

8.3 Control Distributions

In this section the control distributions are presented. After all selection cuts have been applied to data and both the signal and background MC samples, the number of selected MC events is normalised to data using NNLO cross-section predictions, assuming an uncertainty of 5% for signal and background samples,

[2]More rigorous approach would require to consider statistical uncertainties on $N^{Multi-jet}$ as correlated between the variations, resulting in reduction to the the size of the uncertainty band. Nevertheless, since assumption was made regarding the homogeneity between shapes of the multi-jet distribution surviving signal selection in data and originating from enhanced selection, in order to avoid underestimation of the uncertainty the errors were considered uncorrelated.

	Multi-jet
$46 < m_Z < 66$	$2037.26 \pm 96.46_{(stat)} \pm 298.79_{(syst)}$
$66 < m_Z < 116$	$1663.31 \pm 147.05_{(stat)} \pm 534.52_{(syst)}$
$116 < m_Z < 150$	$252.23 \pm 38.19_{(stat)} \pm 94.49_{(syst)}$
$46 < m_Z < 150$	$4144.26 \pm 189.62_{(stat)} \pm 1041.81_{(syst)}$

Table 8.1: Data driven estimate for the number of Multi-jet events differentiated over M_Z bins.

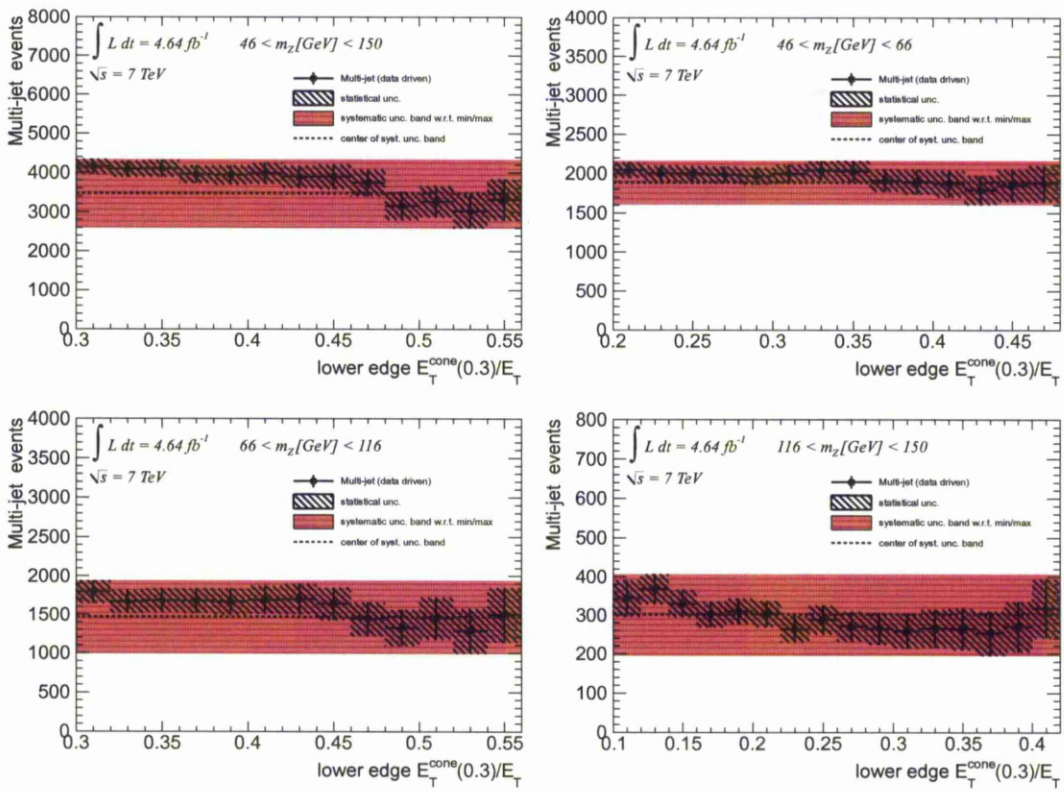

Figure 8.8: Scan over the region used to evaluate the systematic uncertainty for the data driven Multi-jet scaling, shown across different Z mass bins. As may be observed the $N^{Multi-jet}$ distribution is largely independent from the width of the normalization interval. The hashed error bars represent statistical uncertainty on each variation. Red area reflects uncertainty band which is an interval between maximum and minimum deviation, including statistical fluctuations. The dashed line is set as the center of the uncertainty band.

except for the di-boson and $t\bar{t}$ samples, where the uncertainty is 7% and $(^{+7\%}_{-10\%})$ respectively (see Section 6.3). The statistical uncertainty is represented by a yellow band, while the green band includes statistical and systematic uncertainties combined in quadrature. Several electron and Z boson kinematic variables distributions are considered as the control distributions, in order to investigate the final level of agreement between MC predictions (reweighted, according to description in Section 6.4) and the observed data.

Electron Variables

The distributions of electron kinematic variables are illustrated in a linear scale in Figures 8.9–8.11 and in a logarithmic scale in Figures 8.12–8.14. The control distributions of electron p_T, electron cluster η and electron track ϕ are presented for the three m_Z ranges. As seen from the Data/MC ratio plots, an overall good agrement between data and MC is observed.

Boson Variables

The control distributions of Z boson variables are illustrated in this section. Invariant mass distribution integrated over rapidity in the range $0 < |y_Z| < 2.4$ is presented, as well as the rapidity integrated over mass range $46 < m_Z < 150$. Both presented in linear and logarithmic scale in Figure 8.15. Further comparison of boson p_T and rapidity η is performed in three mass ranges, and shown in Figure 8.17 and Figure 8.18 respectively in linear, and in Figure 8.20 and Figure 8.21 in logarithmic scale. From the Figure 8.16 and Figure 8.19 it is visible that the Z mass peak region is well modeled (within 2%) by the MC simulation, while for the $\sim 60 - 80$ GeV mass region a redundancy of approximately 10%, that evolves into deficit of the same order below 60 GeV is observed.

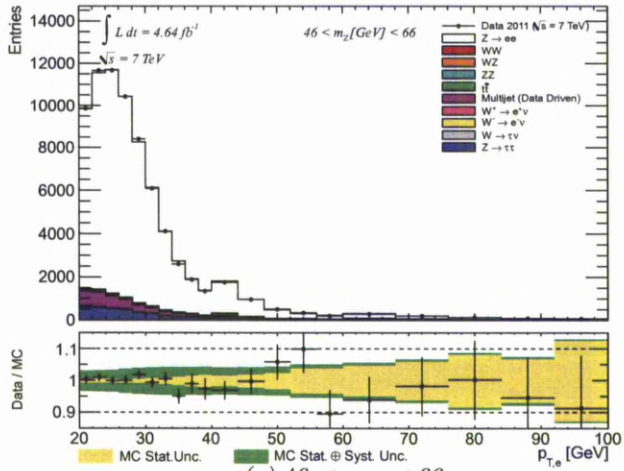

(a) $46 < m_Z < 66$

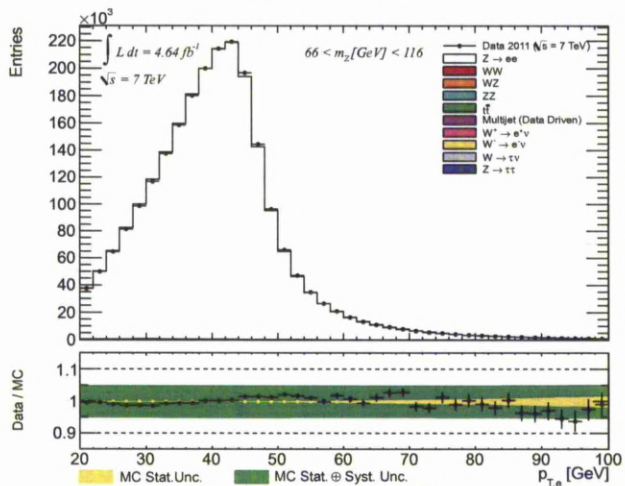

(b) $66 < m_Z < 116$

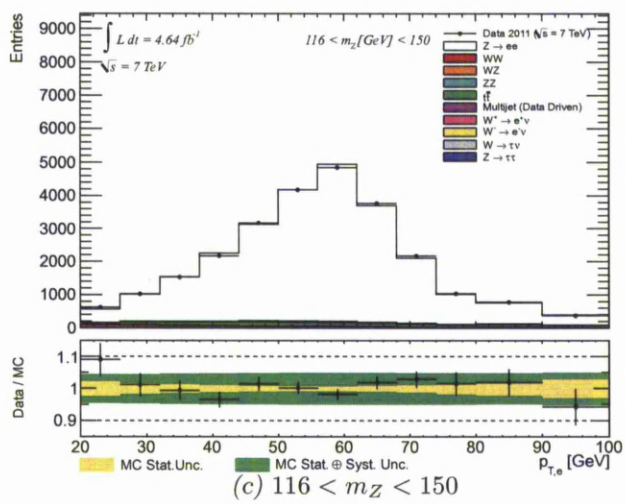

(c) $116 < m_Z < 150$

Figure 8.9: Distribution of the electron transverse momentum p_T presented in the linear scale for the three m_Z ranges.

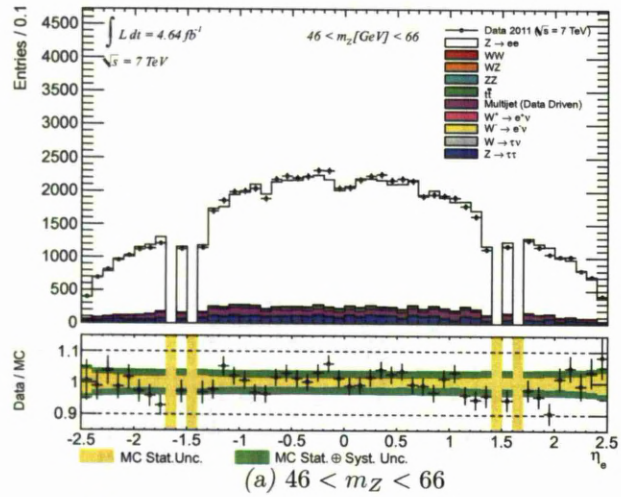

(a) $46 < m_Z < 66$

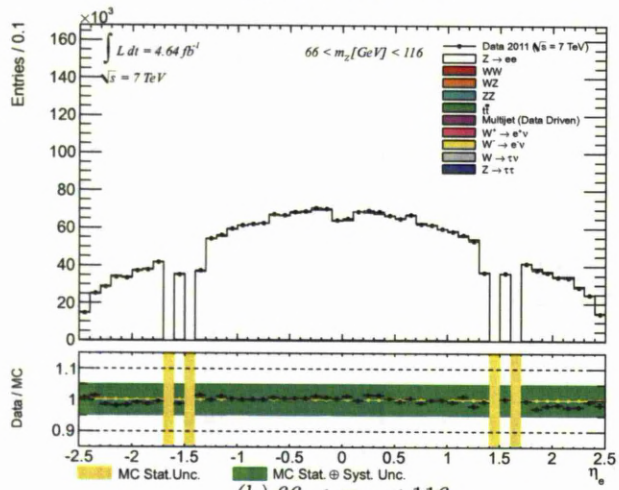

(b) $66 < m_Z < 116$

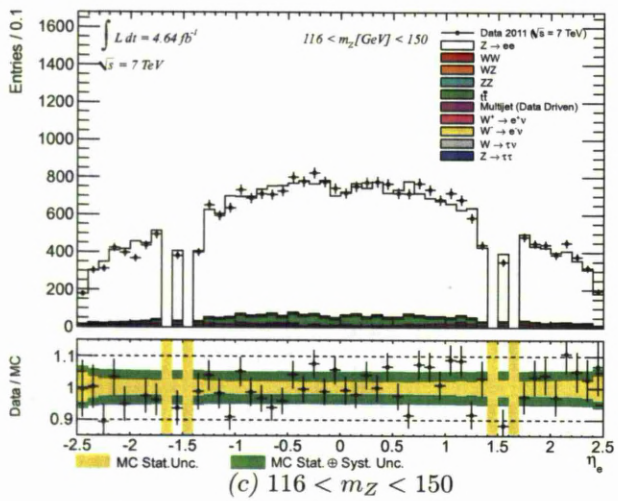

(c) $116 < m_Z < 150$

Figure 8.10: Distribution of the electron cluster pseudorapidity η presented in the linear scale for the three m_Z ranges.

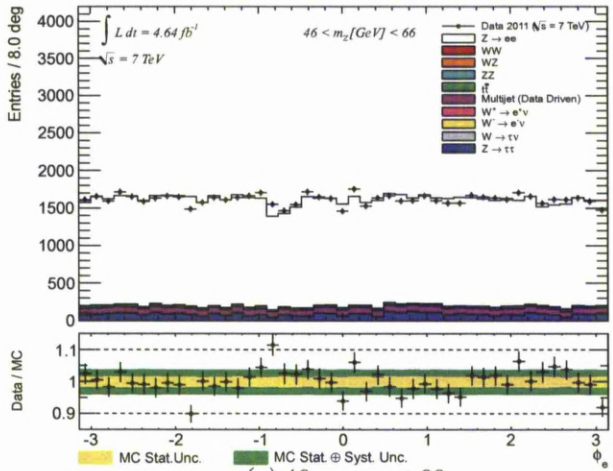

(a) $46 < m_Z < 66$

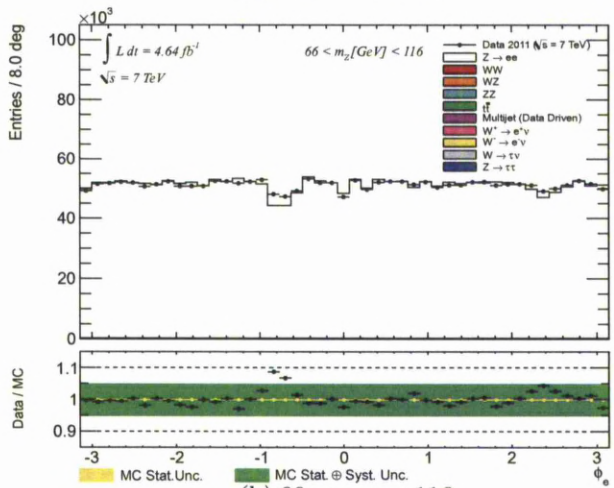

(b) $66 < m_Z < 116$

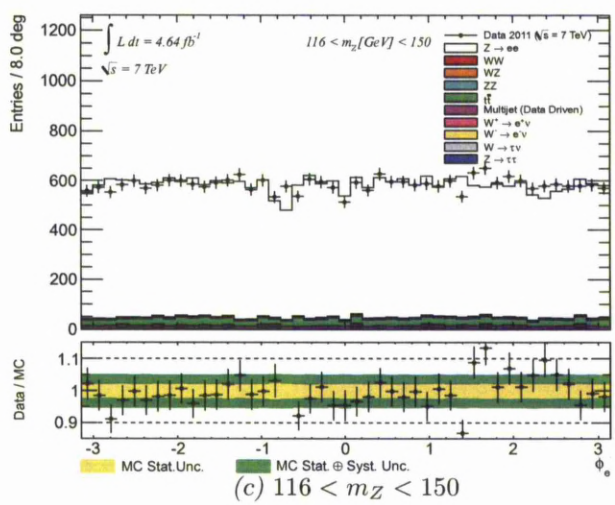

(c) $116 < m_Z < 150$

Figure 8.11: Distribution of the electron track azimuthal angle ϕ presented in the linear scale for the three m_Z ranges.

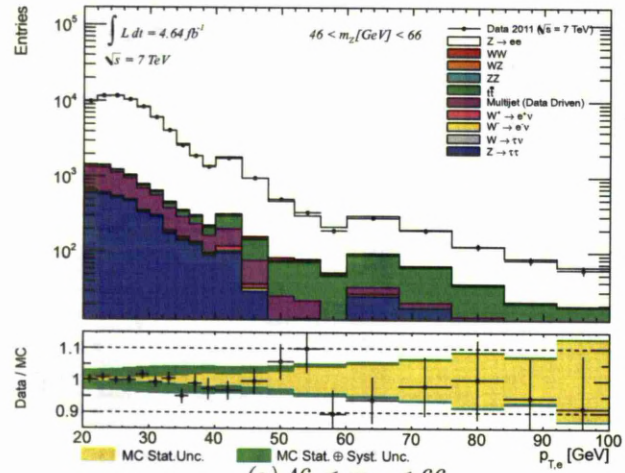

(a) $46 < m_Z < 66$

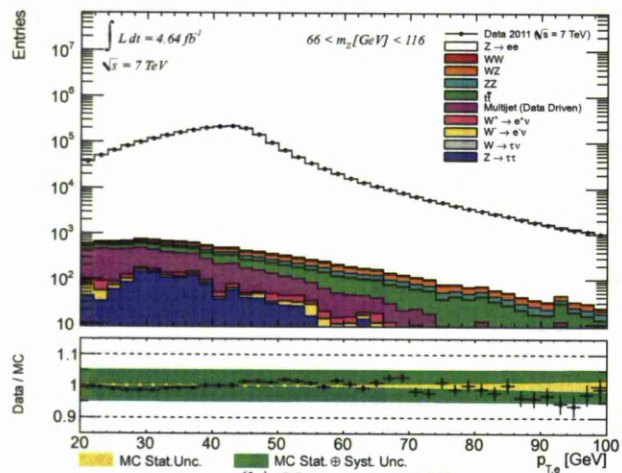

(b) $66 < m_Z < 116$

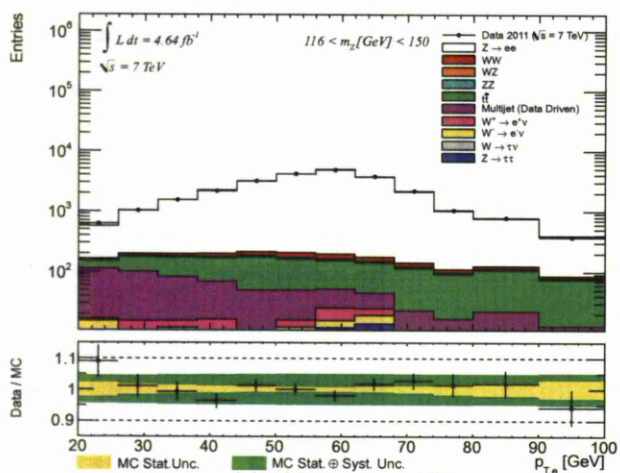

(c) $116 < m_Z < 150$

Figure 8.12: Distribution of the electron transverse momentum p_T presented in the logarithmic scale for the three m_Z ranges.

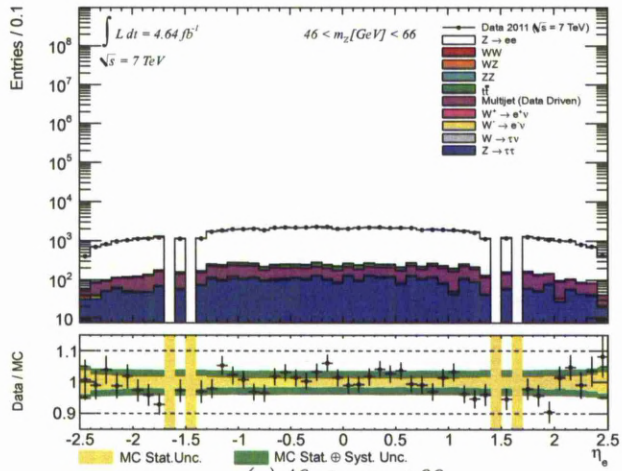

(a) $46 < m_Z < 66$

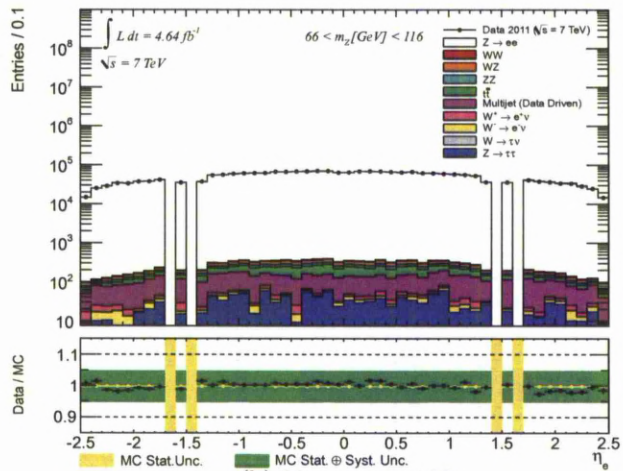

(b) $66 < m_Z < 116$

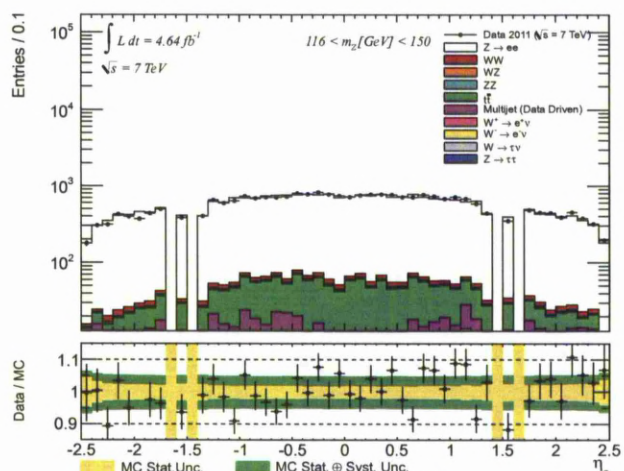

(c) $116 < m_Z < 150$

Figure 8.13: Distribution of the electron cluster pseudorapidity η presented in the logarithmic scale for the three m_Z ranges.

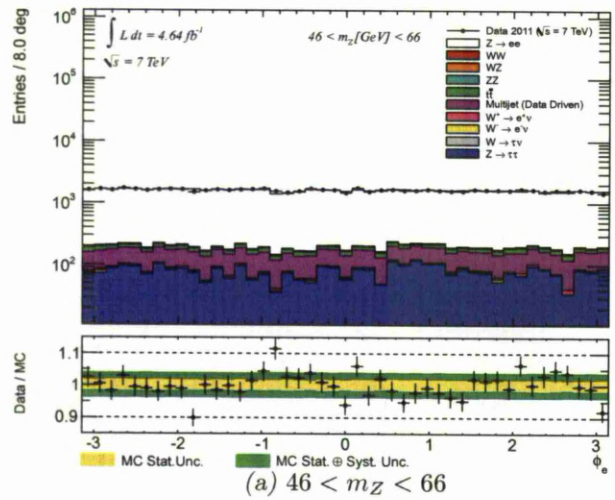

(a) $46 < m_Z < 66$

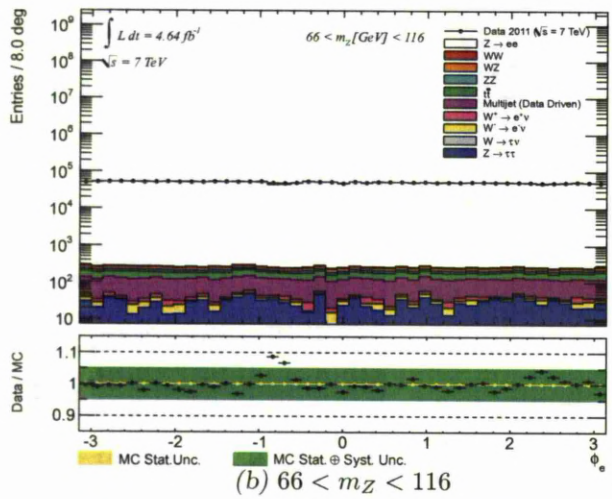

(b) $66 < m_Z < 116$

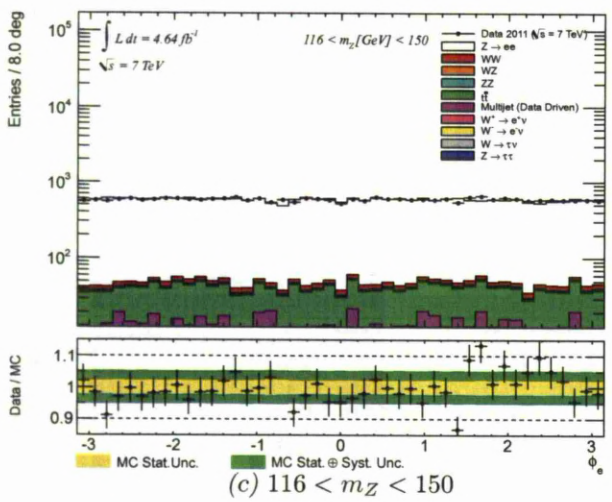

(c) $116 < m_Z < 150$

Figure 8.14: Distribution of the electron track azimuthal angle ϕ presented in the logarithmic scale for the three m_Z ranges.

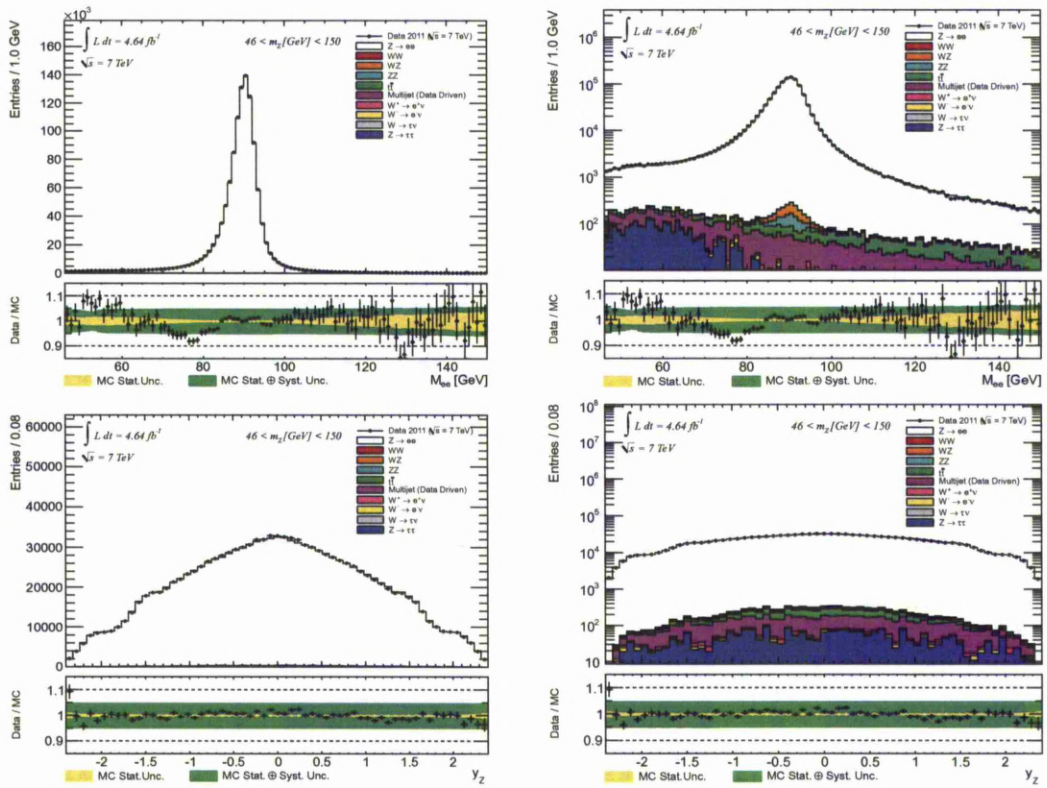

Figure 8.15: Distribution of the Z mass integrated over rapidity in the range $0 < |y_Z| < 2.4$ (top) and the rapidity integrated over mass range $46 < m_Z < 150$ (bottom), presented in linear (left) and logarithmic (right) scale.

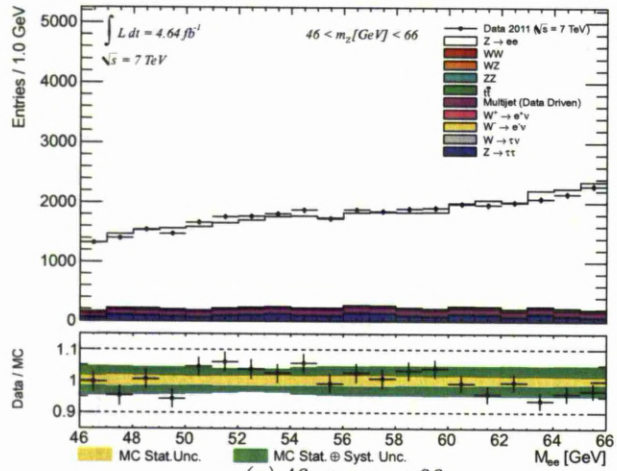

(a) $46 < m_Z < 66$

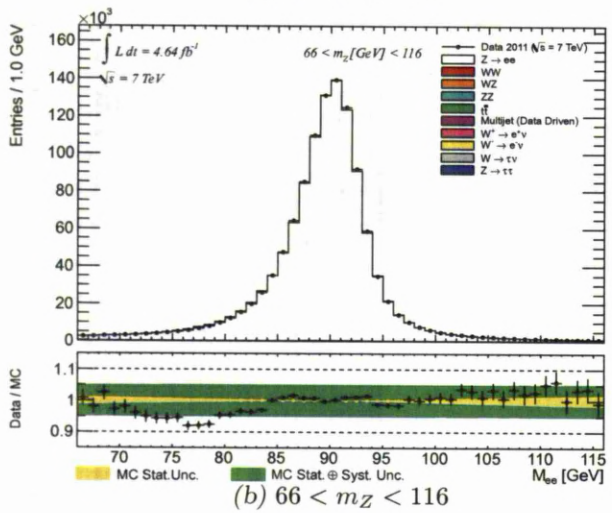

(b) $66 < m_Z < 116$

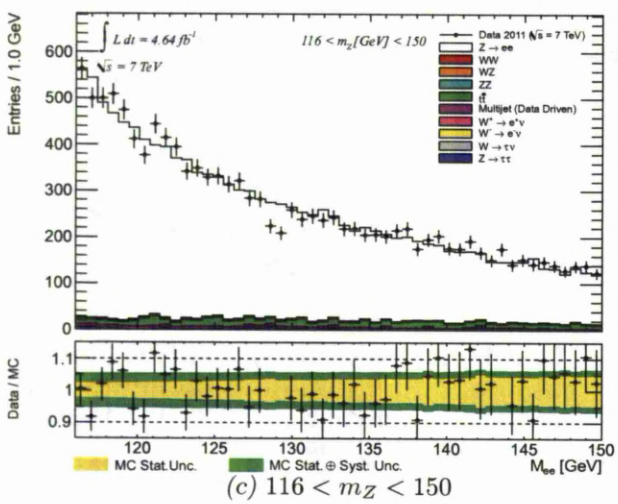

(c) $116 < m_Z < 150$

Figure 8.16: Distribution of the Z boson mass presented in the linear scale for the three m_Z ranges.

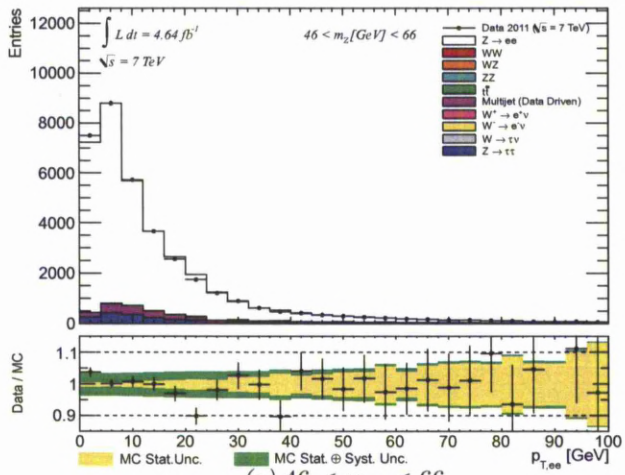

(a) $46 < m_Z < 66$

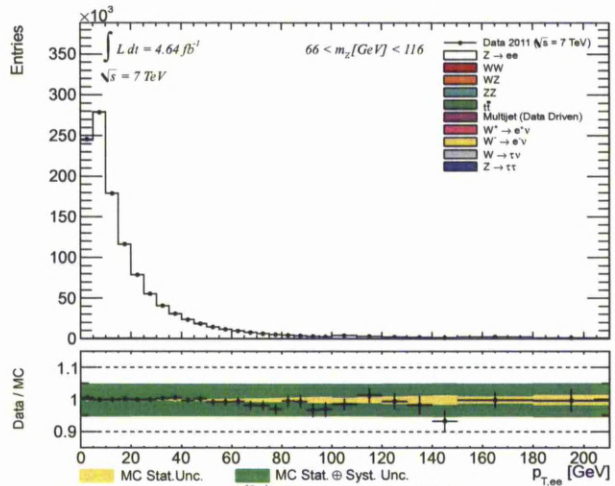

(b) $66 < m_Z < 116$

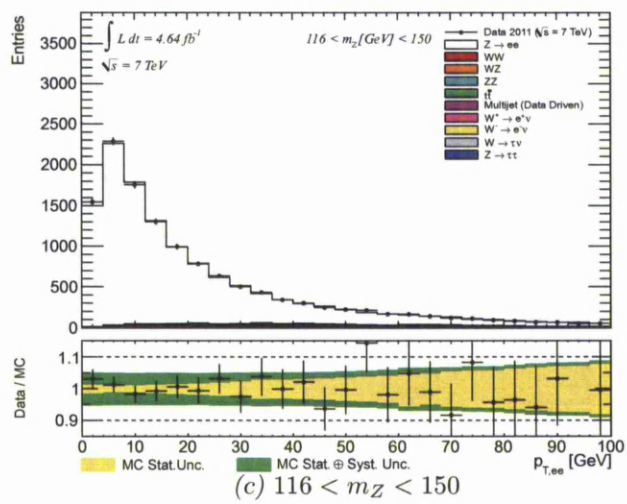

(c) $116 < m_Z < 150$

Figure 8.17: Distribution of the Z boson transverse momentum p_T presented in the linear scale for the three m_Z ranges.

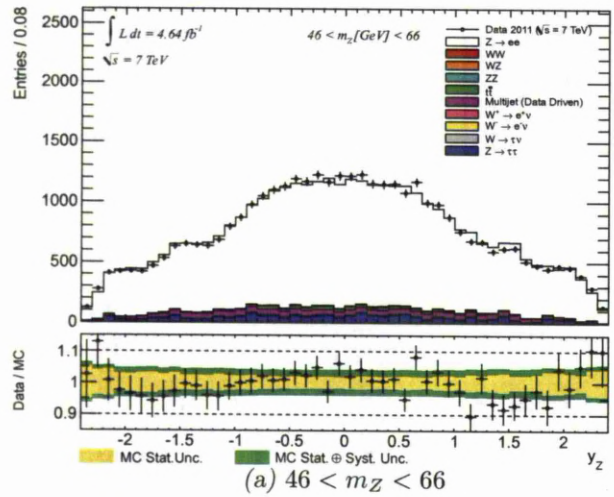

(a) $46 < m_Z < 66$

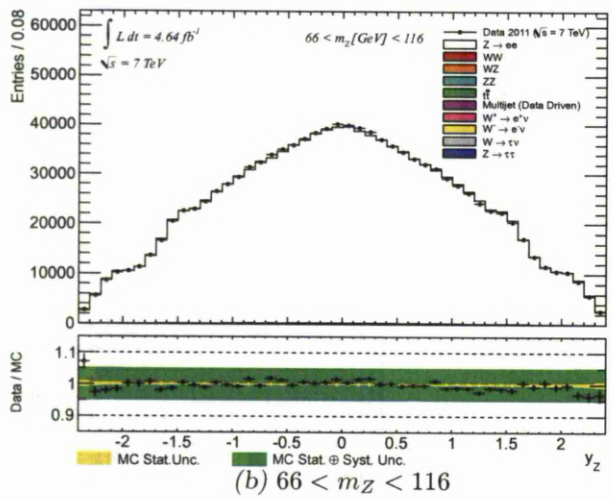

(b) $66 < m_Z < 116$

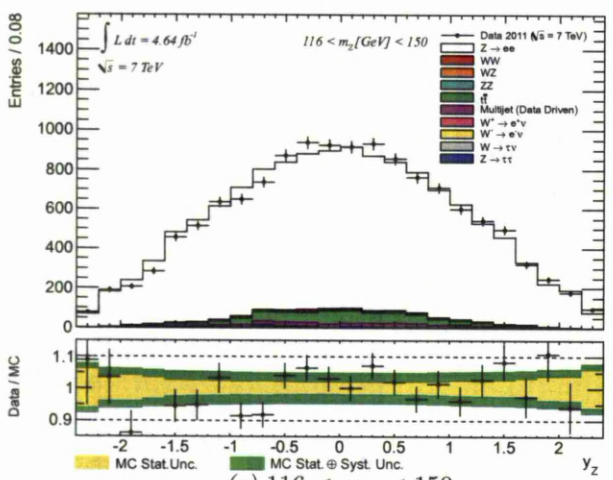

(c) $116 < m_Z < 150$

Figure 8.18: Distribution of the Z boson rapidity y presented in the linear scale for the three m_Z ranges.

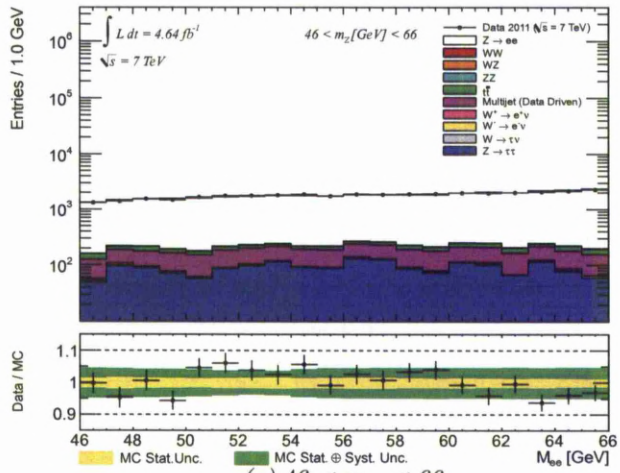

(a) $46 < m_Z < 66$

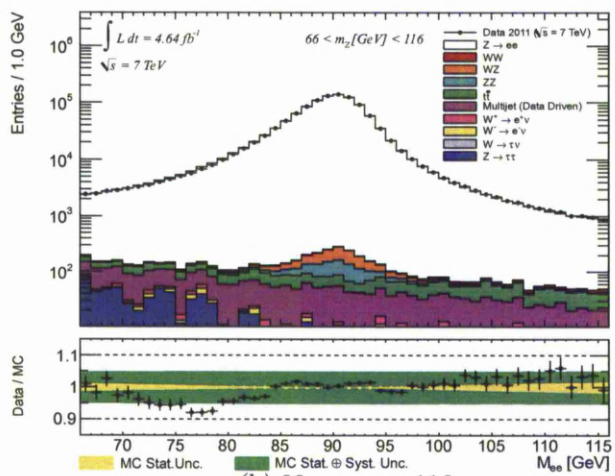

(b) $66 < m_Z < 116$

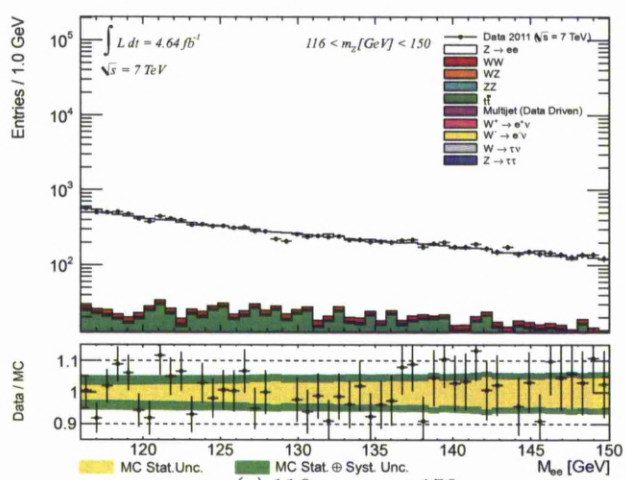

(c) $116 < m_Z < 150$

Figure 8.19: Distribution of the Z boson mass presented in the logarithmic scale for the three m_Z ranges.

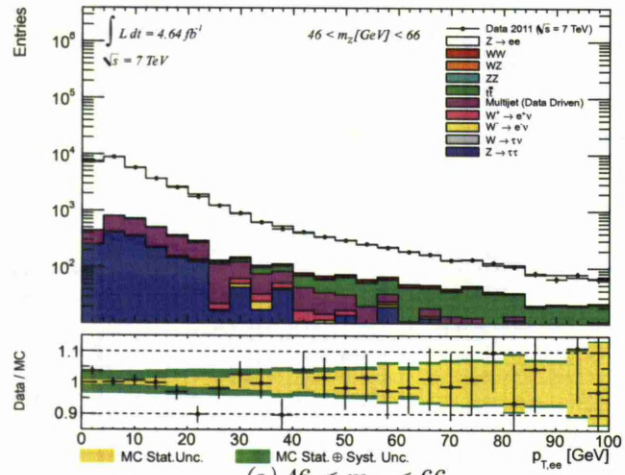

(a) $46 < m_Z < 66$

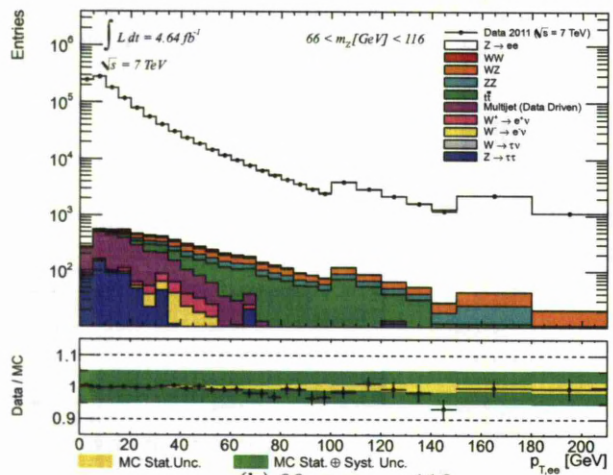

(b) $66 < m_Z < 116$

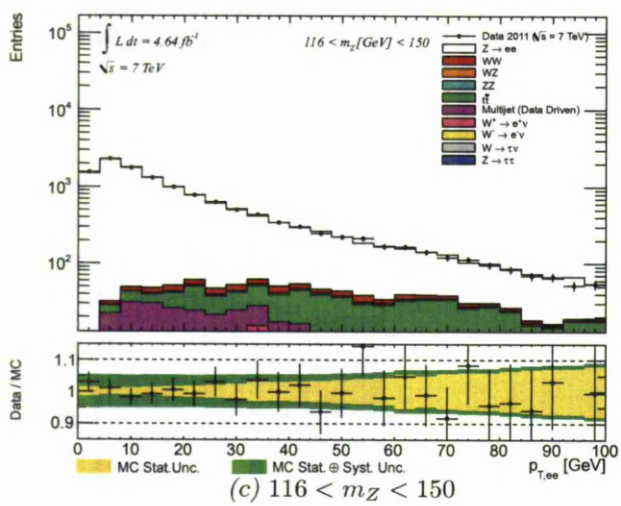

(c) $116 < m_Z < 150$

Figure 8.20: Distribution of the Z boson transverse momentum p_T presented in the logarithmic scale for the three m_Z ranges.

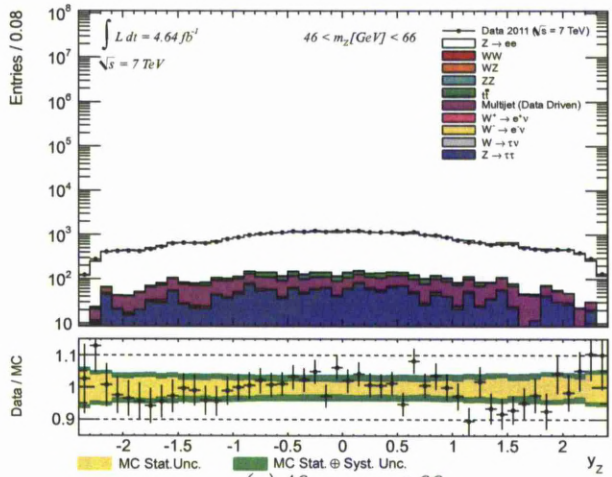

(a) $46 < m_Z < 66$

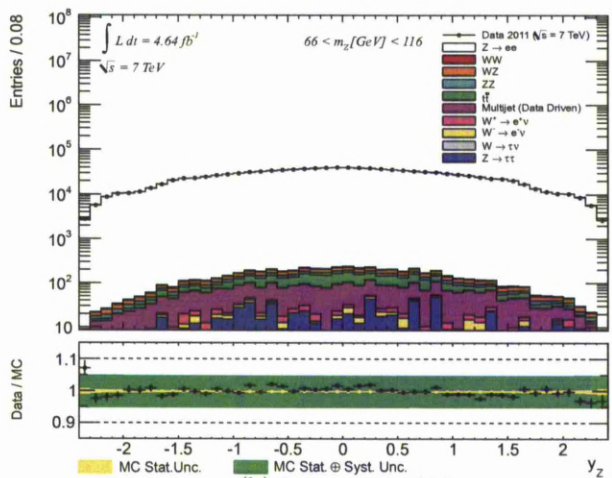

(b) $66 < m_Z < 116$

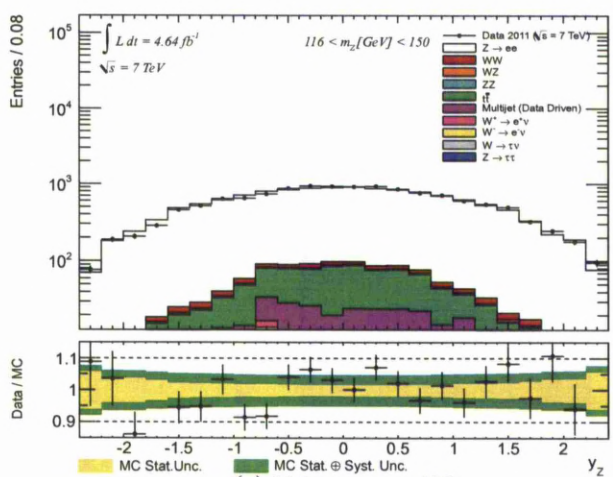

(c) $116 < m_Z < 150$

Figure 8.21: Distribution of the Z boson rapidity y presented in the logarithmic scale for the three m_Z ranges.

	$46-66$	$66-116$	$116-150$
$t\bar{t}$	$(1.58 \pm 0.05)^{+0.11}_{-0.16}$	$(0.12 \pm 0.00)^{+0.01}_{-0.01}$	$(4.55 \pm 0.14)^{+0.32}_{-0.46}$
$Z/\gamma^* \to \tau^+\tau^-$	$4.81 \pm 0.26 \pm 0.24$	$0.05 \pm 0.00 \pm 0.00$	$0.26 \pm 0.09 \pm 0.01$
$W^+ \to e^+\nu_e$	$0.22 \pm 0.03 \pm 0.01$	$0.01 \pm 0.00 \pm 0.00$	$0.21 \pm 0.05 \pm 0.01$
$W^- \to e^-\bar{\nu}_e$	$0.14 \pm 0.02 \pm 0.01$	$0.01 \pm 0.00 \pm 0.00$	$0.21 \pm 0.04 \pm 0.01$
WW	$0.31 \pm 0.01 \pm 0.02$	$0.03 \pm 0.00 \pm 0.00$	$0.95 \pm 0.02 \pm 0.07$
WZ	$0.06 \pm 0.00 \pm 0.00$	$0.08 \pm 0.00 \pm 0.01$	$0.23 \pm 0.01 \pm 0.02$
ZZ	$0.03 \pm 0.00 \pm 0.00$	$0.05 \pm 0.00 \pm 0.00$	$0.09 \pm 0.00 \pm 0.01$
$W \to \tau\nu_\tau$	$0.00 \pm 0.00 \pm 0.00$	$0.01 \pm 0.01 \pm 0.00$	$0.50 \pm 0.50 \pm 0.02$
EWK + $t\bar{t}$	$(7.15 \pm 0.27)^{+0.27}_{-0.29}$	$(0.36 \pm 0.01)^{+0.01}_{-0.01}$	$(7.00 \pm 0.53)^{+0.33}_{-0.46}$
Multi-jet	$5.60 \pm 0.29 \pm 0.82$	$0.14 \pm 0.01 \pm 0.05$	$2.05 \pm 0.31 \pm 0.72$
Total	$(12.75 \pm 0.40)^{+0.86}_{-0.87}$	$0.50 \pm 0.01 \pm 0.05$	$(9.05 \pm 0.61)^{+0.79}_{-0.85}$

Table 8.2: Fraction of background events in per cent for the different mass bins integrated over rapidity. Values are quoted with statistical and systematic uncertainties respectively.

8.4 Summary of Background Contributions

The individual contributions of different background processes are detailed in this section. The fraction of background events for the three different mass bins is summarised in Table 8.2. The fraction of background events in rapidity bins and for $46 < m_Z < 66$, $66 < m_Z < 116$ and $116 < m_Z < 150$ mass bins is presented in Table 8.3, Table 8.4 and Table 8.5 respectively. The values are quoted with statistical and systematic uncertainties. The systematic uncertainty on the number of predicted electroweak background events comes directly from the uncertainty on the theoretical NNLO cross-section values used to normalise MC predictions, and are typically within $5-7\%$, as described in Section 6.3.

	$0.00-0.40$	$0.40-0.80$	$0.80-1.20$	$1.20-1.60$	$1.60-2.00$	$2.00-2.40$
$t\bar{t}$	$(2.18 \pm 0.12)^{+0.15}_{-0.22}$	$(2.14 \pm 0.12)^{+0.15}_{-0.21}$	$(1.49 \pm 0.12)^{+0.10}_{-0.15}$	$(1.12 \pm 0.11)^{+0.08}_{-0.11}$	$(0.52 \pm 0.11)^{+0.04}_{-0.05}$	$(0.12 \pm 0.07)^{+0.01}_{-0.01}$
$Z/\gamma^* \to \tau^+\tau^-$	$4.66 \pm 0.49 \pm 0.23$	$4.53 \pm 0.52 \pm 0.23$	$5.22 \pm 0.64 \pm 0.26$	$4.98 \pm 0.72 \pm 0.25$	$4.77 \pm 0.80 \pm 0.24$	$5.09 \pm 0.96 \pm 0.25$
$W^+ \to e^+\nu_e$	$0.16 \pm 0.05 \pm 0.01$	$0.24 \pm 0.06 \pm 0.01$	$0.22 \pm 0.07 \pm 0.01$	$0.23 \pm 0.07 \pm 0.01$	$0.23 \pm 0.09 \pm 0.01$	$0.33 \pm 0.13 \pm 0.02$
$W^- \to e^-\bar{\nu}_e$	$0.11 \pm 0.04 \pm 0.01$	$0.11 \pm 0.04 \pm 0.01$	$0.25 \pm 0.07 \pm 0.01$	$0.12 \pm 0.05 \pm 0.01$	$0.12 \pm 0.06 \pm 0.01$	$0.18 \pm 0.09 \pm 0.01$
WW	$0.30 \pm 0.01 \pm 0.02$	$0.31 \pm 0.01 \pm 0.02$	$0.32 \pm 0.02 \pm 0.02$	$0.32 \pm 0.02 \pm 0.02$	$0.32 \pm 0.02 \pm 0.02$	$0.23 \pm 0.02 \pm 0.02$
WZ	$0.06 \pm 0.00 \pm 0.00$	$0.07 \pm 0.00 \pm 0.00$	$0.07 \pm 0.01 \pm 0.00$	$0.07 \pm 0.01 \pm 0.00$	$0.05 \pm 0.01 \pm 0.00$	$0.04 \pm 0.01 \pm 0.00$
ZZ	$0.02 \pm 0.00 \pm 0.00$	$0.03 \pm 0.00 \pm 0.00$	$0.03 \pm 0.00 \pm 0.00$	$0.03 \pm 0.00 \pm 0.00$	$0.03 \pm 0.00 \pm 0.00$	$0.01 \pm 0.00 \pm 0.00$
$W \to \tau\nu_\tau$	$0.00 \pm 0.00 \pm 0.00$	$0.00 \pm 0.00 \pm 0.00$	$0.00 \pm 0.00 \pm 0.00$	$0.00 \pm 0.00 \pm 0.00$	$0.00 \pm 0.00 \pm 0.00$	$0.00 \pm 0.00 \pm 0.00$
EWK + $t\bar{t}$	$(7.51 \pm 0.51)^{+0.28}_{-0.32}$	$(7.43 \pm 0.54)^{+0.27}_{-0.31}$	$(7.59 \pm 0.66)^{+0.28}_{-0.30}$	$(6.87 \pm 0.73)^{+0.26}_{-0.27}$	$(6.05 \pm 0.82)^{+0.24}_{-0.25}$	$(6.01 \pm 0.97)^{+0.26}_{-0.26}$
Multi-jet	$4.34 \pm 0.41 \pm 0.64$	$4.92 \pm 0.44 \pm 0.72$	$6.43 \pm 0.60 \pm 0.94$	$7.83 \pm 0.78 \pm 1.15$	$6.91 \pm 1.05 \pm 1.01$	$4.22 \pm 1.57 \pm 0.62$
Total	$(11.85 \pm 0.65)^{+0.70}_{-0.72}$	$(12.35 \pm 0.70)^{+0.77}_{-0.78}$	$(14.02 \pm 0.89)^{+0.98}_{-0.99}$	$14.7 \pm 1.07 \pm 1.18$	$12.96 \pm 1.33 \pm 1.04$	$10.23 \pm 1.85 \pm 0.67$

Table 8.3: Fraction of background events in per cent for $46 < m_Z < 66 GeV$. Values are quoted with statistical and systematic uncertainties respectively.

	0.00 – 0.20	0.20 – 0.40	0.40 – 0.60	0.60 – 0.80	0.80 – 1.00	1.00 – 1.20	1.20 – 1.40	1.40 – 1.60	1.60 – 1.80	1.80 – 2.00	2.00 – 2.20	2.20 – 2.40
$t\bar{t}$	$(0.18 \pm 0.01)^{+0.01}_{-0.02}$	$(0.16 \pm 0.01)^{+0.01}_{-0.02}$	$(0.15 \pm 0.01)^{+0.01}_{-0.02}$	$(0.16 \pm 0.01)^{+0.01}_{-0.02}$	$(0.12 \pm 0.01)^{+0.01}_{-0.01}$	$(0.09 \pm 0.01)^{+0.01}_{-0.01}$	$(0.08 \pm 0.01)^{+0.01}_{-0.01}$	$(0.06 \pm 0.01)^{+0.00}_{-0.01}$	$(0.08 \pm 0.01)^{+0.01}_{-0.01}$	$(0.05 \pm 0.01)^{+0.00}_{-0.00}$	$(0.02 \pm 0.01)^{+0.00}_{-0.00}$	$(0.03 \pm 0.01)^{+0.00}_{-0.00}$
$Z/\gamma^* \to \tau^+\tau^-$	$0.03 \pm 0.01 \pm 0.00$	$0.06 \pm 0.02 \pm 0.00$	$0.04 \pm 0.01 \pm 0.00$	$0.07 \pm 0.02 \pm 0.00$	$0.10 \pm 0.02 \pm 0.00$	$0.04 \pm 0.01 \pm 0.00$	$0.05 \pm 0.02 \pm 0.00$	$0.02 \pm 0.01 \pm 0.00$	$0.05 \pm 0.02 \pm 0.00$	$0.06 \pm 0.03 \pm 0.00$	$0.05 \pm 0.03 \pm 0.00$	$0.02 \pm 0.03 \pm 0.00$
$W^+ \to e^+\nu_e$	$0.01 \pm 0.00 \pm 0.00$	$0.01 \pm 0.00 \pm 0.00$	$0.01 \pm 0.00 \pm 0.00$	$0.01 \pm 0.00 \pm 0.00$	$0.01 \pm 0.00 \pm 0.00$	$0.02 \pm 0.01 \pm 0.00$	$0.02 \pm 0.00 \pm 0.00$	$0.01 \pm 0.00 \pm 0.00$	$0.01 \pm 0.01 \pm 0.00$	$0.01 \pm 0.01 \pm 0.00$	$0.03 \pm 0.01 \pm 0.00$	$0.02 \pm 0.01 \pm 0.00$
$W^- \to e^-\bar{\nu}_e$	$0.01 \pm 0.00 \pm 0.00$	$0.01 \pm 0.00 \pm 0.00$	$0.01 \pm 0.00 \pm 0.00$	$0.01 \pm 0.00 \pm 0.00$	$0.01 \pm 0.00 \pm 0.00$	$0.01 \pm 0.00 \pm 0.00$	$0.01 \pm 0.00 \pm 0.00$	$0.02 \pm 0.01 \pm 0.00$	$0.01 \pm 0.01 \pm 0.00$	$0.01 \pm 0.01 \pm 0.00$	$0.02 \pm 0.01 \pm 0.00$	$0.05 \pm 0.02 \pm 0.00$
WW	$0.03 \pm 0.00 \pm 0.00$	$0.03 \pm 0.00 \pm 0.00$	$0.03 \pm 0.00 \pm 0.00$	$0.03 \pm 0.00 \pm 0.00$	$0.03 \pm 0.00 \pm 0.00$	$0.03 \pm 0.00 \pm 0.00$	$0.03 \pm 0.00 \pm 0.00$	$0.03 \pm 0.00 \pm 0.00$	$0.02 \pm 0.00 \pm 0.00$	$0.02 \pm 0.00 \pm 0.00$	$0.02 \pm 0.00 \pm 0.00$	$0.02 \pm 0.00 \pm 0.00$
WZ	$0.08 \pm 0.00 \pm 0.01$	$0.08 \pm 0.00 \pm 0.01$	$0.08 \pm 0.00 \pm 0.01$	$0.08 \pm 0.00 \pm 0.01$	$0.07 \pm 0.00 \pm 0.00$	$0.07 \pm 0.00 \pm 0.00$	$0.07 \pm 0.00 \pm 0.00$	$0.07 \pm 0.00 \pm 0.00$	$0.07 \pm 0.00 \pm 0.01$	$0.07 \pm 0.00 \pm 0.00$	$0.07 \pm 0.00 \pm 0.00$	$0.06 \pm 0.00 \pm 0.00$
ZZ	$0.06 \pm 0.00 \pm 0.00$	$0.06 \pm 0.00 \pm 0.00$	$0.06 \pm 0.00 \pm 0.00$	$0.06 \pm 0.00 \pm 0.00$	$0.05 \pm 0.00 \pm 0.00$	$0.05 \pm 0.00 \pm 0.00$	$0.04 \pm 0.00 \pm 0.00$	$0.05 \pm 0.00 \pm 0.00$	$0.05 \pm 0.00 \pm 0.00$	$0.05 \pm 0.00 \pm 0.00$	$0.04 \pm 0.00 \pm 0.00$	$0.05 \pm 0.00 \pm 0.00$
$W \to \tau\nu_\tau$	$0.00 \pm 0.00 \pm 0.00$	$0.00 \pm 0.00 \pm 0.00$	$0.00 \pm 0.00 \pm 0.00$	$0.00 \pm 0.00 \pm 0.00$	$0.00 \pm 0.00 \pm 0.00$	$0.00 \pm 0.00 \pm 0.00$	$0.00 \pm 0.00 \pm 0.00$	$0.00 \pm 0.00 \pm 0.00$	$0.00 \pm 0.00 \pm 0.00$	$0.00 \pm 0.00 \pm 0.00$	$0.00 \pm 0.00 \pm 0.00$	$0.00 \pm 0.00 \pm 0.00$
EWK + $t\bar{t}$	$(0.39 \pm 0.01)^{+0.01}_{-0.02}$	$(0.41 \pm 0.02)^{+0.01}_{-0.02}$	$(0.38 \pm 0.02)^{+0.01}_{-0.02}$	$(0.42 \pm 0.02)^{+0.01}_{-0.02}$	$(0.43 \pm 0.04)^{+0.01}_{-0.02}$	$(0.36 \pm 0.06)^{+0.01}_{-0.01}$	$(0.31 \pm 0.02)^{+0.01}_{-0.01}$	$(0.25 \pm 0.01)^{+0.01}_{-0.01}$	$(0.30 \pm 0.02)^{+0.01}_{-0.01}$	$(0.29 \pm 0.03)^{+0.01}_{-0.01}$	$(0.26 \pm 0.03)^{+0.01}_{-0.01}$	$(0.25 \pm 0.04)^{+0.01}_{-0.01}$
Multi-jet	$0.15 \pm 0.03 \pm 0.05$	$0.14 \pm 0.03 \pm 0.05$	$0.14 \pm 0.03 \pm 0.05$	$0.15 \pm 0.03 \pm 0.05$	$0.15 \pm 0.04 \pm 0.05$	$0.16 \pm 0.04 \pm 0.05$	$0.15 \pm 0.06 \pm 0.05$	$0.15 \pm 0.05 \pm 0.05$	$0.14 \pm 0.07 \pm 0.05$	$0.13 \pm 0.10 \pm 0.04$	$0.09 \pm 0.11 \pm 0.03$	$0.09 \pm 0.25 \pm 0.03$
Total	$0.54 \pm 0.03 \pm 0.05$	$0.55 \pm 0.04 \pm 0.05$	$0.52 \pm 0.04 \pm 0.05$	$0.57 \pm 0.04 \pm 0.05$	$0.58 \pm 0.06 \pm 0.05$	$0.52 \pm 0.07 \pm 0.05$	$0.46 \pm 0.06 \pm 0.05$	$0.40 \pm 0.05 \pm 0.05$	$0.44 \pm 0.07 \pm 0.05$	$0.42 \pm 0.10 \pm 0.04$	$0.35 \pm 0.11 \pm 0.03$	$0.34 \pm 0.25 \pm 0.03$

Table 8.4: Fraction of background events in per cent for $66 < m_Z < 116 GeV$. Values are quoted with statistical and systematic uncertainties respectively.

	$0.00-0.40$	$0.40-0.80$	$0.80-1.20$	$1.20-1.60$	$1.60-2.00$	$2.00-2.40$
$t\bar{t}$	$(6.25 \pm 0.31)^{+0.44}_{-0.62}$	$(5.96 \pm 0.31)^{+0.42}_{-0.60}$	$(3.91 \pm 0.30)^{+0.27}_{-0.39}$	$(2.63 \pm 0.27)^{+0.18}_{-0.26}$	$(1.53 \pm 0.27)^{+0.11}_{-0.15}$	$(0.69 \pm 0.27)^{+0.05}_{-0.07}$
$Z/\gamma^* \to \tau^+\tau^-$	$0.11 \pm 0.11 \pm 0.01$	$0.47 \pm 0.24 \pm 0.02$	$0.19 \pm 0.19 \pm 0.01$	$0.00 \pm 0.00 \pm 0.00$	$0.92 \pm 0.65 \pm 0.05$	$0.00 \pm 0.00 \pm 0.00$
$W^+ \to e^+\nu_e$	$0.18 \pm 0.08 \pm 0.01$	$0.21 \pm 0.10 \pm 0.01$	$0.23 \pm 0.11 \pm 0.01$	$0.24 \pm 0.12 \pm 0.01$	$0.27 \pm 0.19 \pm 0.01$	$0.00 \pm 0.00 \pm 0.00$
$W^- \to e^-\bar{\nu}_e$	$0.17 \pm 0.08 \pm 0.01$	$0.33 \pm 0.11 \pm 0.02$	$0.14 \pm 0.08 \pm 0.01$	$0.11 \pm 0.08 \pm 0.01$	$0.48 \pm 0.24 \pm 0.02$	$0.00 \pm 0.00 \pm 0.00$
WW	$1.00 \pm 0.04 \pm 0.07$	$1.03 \pm 0.04 \pm 0.07$	$1.00 \pm 0.05 \pm 0.07$	$0.88 \pm 0.05 \pm 0.06$	$0.78 \pm 0.07 \pm 0.05$	$0.47 \pm 0.07 \pm 0.03$
WZ	$0.24 \pm 0.01 \pm 0.02$	$0.25 \pm 0.02 \pm 0.02$	$0.22 \pm 0.02 \pm 0.02$	$0.23 \pm 0.02 \pm 0.02$	$0.18 \pm 0.02 \pm 0.01$	$0.14 \pm 0.03 \pm 0.01$
ZZ	$0.09 \pm 0.01 \pm 0.01$	$0.11 \pm 0.01 \pm 0.01$	$0.11 \pm 0.01 \pm 0.01$	$0.09 \pm 0.01 \pm 0.01$	$0.07 \pm 0.01 \pm 0.01$	$0.05 \pm 0.02 \pm 0.00$
$W \to \tau\nu_\tau$	$0.00 \pm 0.00 \pm 0.00$	$0.00 \pm 0.00 \pm 0.00$	$0.00 \pm 0.00 \pm 0.00$	$0.31 \pm 0.27 \pm 0.02$	$0.00 \pm 0.00 \pm 0.00$	$0.00 \pm 0.00 \pm 0.00$
EWK + $t\bar{t}$	$(8.04 \pm 0.35)^{+0.44}_{-0.63}$	$(8.36 \pm 0.42)^{+0.43}_{-0.60}$	$(5.80 \pm 0.38)^{+0.28}_{-0.40}$	$(4.49 \pm 0.41)^{+0.20}_{-0.27}$	$(4.22 \pm 0.77)^{+0.13}_{-0.17}$	$(1.35 \pm 0.28)^{+0.06}_{-0.08}$
Multi-jet	$2.35 \pm 0.42 \pm 0.82$	$2.69 \pm 0.48 \pm 0.94$	$2.03 \pm 0.60 \pm 0.71$	$1.42 \pm 0.78 \pm 0.50$	$1.15 \pm 1.47 \pm 0.40$	$0.54 \pm 2.89 \pm 0.19$
Total	$(10.39 \pm 0.55)^{+0.93}_{-1.03}$	$(11.05 \pm 0.64)^{+1.03}_{-1.12}$	$(7.83 \pm 0.71)^{+0.76}_{-0.82}$	$(5.91 \pm 0.88)^{+0.54}_{-0.56}$	$(5.37 \pm 1.66)^{+0.42}_{-0.43}$	$(1.89 \pm 2.90)^{+0.20}_{-0.21}$

Table 8.5: Fraction of background events in per cent for $116 < m_Z < 150GeV$. Values are quoted with statistical and systematic uncertainties respectively.

Chapter 9

$Z/\gamma^* \rightarrow e^+e^-$ Cross Section Measurement

This chapter presents the summary of results of the $Z/\gamma^* \rightarrow e^+e^-$ cross section measurements. The first sections provide an introduction to the methodology for the cross section calculation, introduce binning definitions for a differential measurements, as well as related studies of the bin-migration effects. Details of the systematic uncertainties related to the cross section measurement, and comparison of results with respect to several theoretical predictions calculated at next-to-next-to leading order (NNLO) in QCD, using various PDF sets, are also included.

9.1 Method of Cross Section Extraction

To extract integrated and differential Z/γ^* production cross-section, the following formula is used:

$$\sigma_Z^{fid} = \frac{N^{sig} - N^{bkg}}{C_Z \cdot L_{int}} \tag{9.1}$$

where,

- N^{sig} is the number of Z/γ^* candidate events observed in data
- N^{bkg} is the number of estimated QCD and electroweak background events

- L_{int} is the integrated luminosity of the data set
- C_Z is the efficiency correction factor, defined as:

$$C_Z = \frac{N_{rec}^{MC}}{N_{gen,analysis\_cuts}^{MC}}, \tag{9.2}$$

and is estimated using information from MC simulation at the generated and reconstructed level, corrected for any variances from electron trigger, reconstruction and identification efficiencies between data and MC. This correction factor is defined as a ratio of the sum of event weights after the reconstruction and analysis selection (N_{rec}^{MC}) to the sum of event weights at the generated level, after analysis fiducial cuts ($N_{gen,analysis\_cuts}^{MC}$) have been applied. The analysis fiducial cuts define the experimental phase space as follows:

- Both Electron $p_T > 20GeV$
- Both Electron $|\eta| < 2.47$
- Excluding $1.37 < |\eta| < 1.52$ and $1.6 < |\eta| < 1.7$
- Di-electron invariant mass m_{ee} bins $[GeV]$:

$$46 < m_{ee} < 66, \qquad 66 < m_{ee} < 116, \qquad 116 < m_{ee} < 150$$

Calculation of the cross-section in the fiducial region provides minimal dependence on the theoretical models applied in the MC simulations, and which are used to derive efficiency-acceptance corrections. The experimental fiducial cross-section measurements are extrapolated to the common phase space, by introducing the extrapolation factor E_Z, defined as:

$$E_Z = \frac{N_{gen,analysis\_cuts}^{MC}}{N_{gen,fiducial\_cuts}^{MC}} \tag{9.3}$$

The E_Z is determined from the ratio of the sum of event weights at the generated level with analysis fiducial cuts applied ($N^{MC}_{gen,analysis\_cuts}$) to the sum of event weights at the generated level, after common fiducial cuts ($N^{MC}_{gen,fiducial\_cuts}$) applied. The common fiducial cuts define the phase space collective to electron and muon Z/γ^* decay channels in the central and forward regions of the detector. Despite the fact, that analysis presented here involves only electrons detected in the central region, this small theoretical extrapolation is performed, allowing comparison to the theoretical predictions. The common fiducial region is defined without setting any restriction with respect to the pseudo-rapidity of the electrons (η_e), but requiring transverse momentum (p_T) of both electrons to be grater than 20 GeV, with the invariant electron pair mass (m_{ee}) within one of the ranges $[GeV]$: $46 < m_{ee} < 66$, $66 < m_{ee} < 116$ or $116 < m_{ee} < 150$.

The total integrated Z/γ^* cross-section is calculated according to the formula:

$$\sigma_Z^{total} = \sigma_Z \times BR(Z/\gamma^* \to e^+e^-) = \frac{N^{sig} - N^{bkg}}{C_Z \cdot E_Z \cdot A_Z \cdot L_{int}} \tag{9.4}$$

The acceptance correction factor A_Z is introduced, which allows extrapolation to the total phase space, using MC generator level information and it is defined as:

$$A_Z = \frac{N^{MC}_{gen,fiducial\_cuts}}{N^{MC}_{all\_gen}}, \tag{9.5}$$

where the $N^{MC}_{all\_gen}$ is the sum of event weights of all events generated within the di-electron invariant mass range of $66 - 116$ GeV.

9.1.1 MC Truth Level Definitions

It is possible to calculate the cross-section at different reference points, determined with respect to the level of QED Final State Radiation (FSR) correction, according to different MC truth level definitions. The PHOTOS package (Sec-

tion 6.2.5), interfaced with the MC signal generators, provides simulation of the QED FSR, and the three points of reference can be distinguished:

Born At the Born level leptons are defined *before* QED FSR, i.e. corrected for all the QED FSR effects.

Bare The bare leptons are defined *after* QED FSR, i.e. no QED corrections applied.

Dressed The dressed leptons imply a partial QED FSR correction, by including the four-vectors of the bare lepton and all QED FSR photons in a cone $\Delta R < 0.1$ defined around the bare lepton's direction.

For the purpose of the following analysis, the efficiency-acceptance correction factors taken from the Monte Carlo generator level are evaluated using electrons extrapolated to the point before QED FSR (Born level), as provided by the PHOTOS algorithm. Consequently the measurements are fully corrected for QED FSR effects, allowing comparison to NNLO QCD calculations.

9.2 Definition of Binnning for the Differential Measurement

The differential $Z/\gamma^* \rightarrow e^+e^-$cross-section measurements are performed in the absolute rapidity $|y_Z|$ bins, defined with respect to the considered invariant mass range $[GeV]$ of the di-electron pair as follows:

$46 < m_{ee} < 66$: Six bins with boundaries at:

$|y_Z| = \{0, 0.4, 0.8, 1.2, 1.6, 2.0, 2.4\}$

$66 < m_{ee} < 116$: Twelve bins with boundaries at:

$|y_Z| = \{0, 0.2, 0.4, 0.6, 0.8, 1.0, 1.2, 1.4, 1.6, 1.8, 2.0, 2.2, 2.4\}$

$116 < m_{ee} < 150$: Six bins with boundaries at:

$|y_Z| = \{0, 0.4, 0.8, 1.2, 1.6, 2.0, 2.4\}$

Hence the Equation 9.1 can be explicitly re-written for the fiducial differential cross-section measured in the i-th rapidity bin, as:

$$\frac{d\sigma^i_{fid}}{dy^i_Z} = \frac{N^i_{sig} - N^i_{bkg}}{C^i_Z \cdot L_{int}} \cdot \frac{1}{dy^i_Z}, \tag{9.6}$$

where dy^i_Z is the bin width, N^i_{sig} is number of the selected candidates in the bin i, N^i_{bkg} is the number of background events in the i-th bin, and C^i_Z is defined as in Equation 9.2, but measured in a given bin i.

9.2.1 Purity and Stability

The chosen bin widths are optimised to provide minimal levels of migration and statistical uncertainties. For a differential cross-section measurement it is desirable, that sufficiently often reconstruction of the electron takes place in the same bin as it's generation. In order to quantify migration into and out of a given bin i, the purity (P) and stability (S) estimators can be defined as:

$$P^i = \frac{N^i_{gen\&rec(all\_cuts)}}{N^i_{rec(all\_cuts)}}; \qquad S^i = \frac{N^i_{gen\&rec(all\_cuts)}}{N^i_{gen(all\_cuts)}} \tag{9.7}$$

Purity and stability of an i-th bin is calculated from MC information at the generated and reconstructed level, after all relevant reconstruction cuts (Table 7.2) have been applied, where $N^i_{gen\&rec(all\_cuts)}$ is the sum of event weights, which were both generated and reconstructed within the same bin i, while $N^i_{gen(all\_cuts)}$ and $N^i_{rec(all\_cuts)}$ are the sum of event weights generated/reconstructed in the bin i respectively. According to the definitions in Equation 9.7, purity represents the fraction of events reconstructed in the bin i, that were also generated in this bin (i.e. migration into the bin), along with stability determining the fraction of events generated in the bin i that were also reconstructed in this bin (i.e. migration out of the bin). Figure 9.1 shows purity and stability for a binning defined in

Section 9.2. Values are close to one, representing pure and stable bins. Therefore the bin-to-bin migration effects are considered as small, and not expected to play a significant role in the differential measurement.

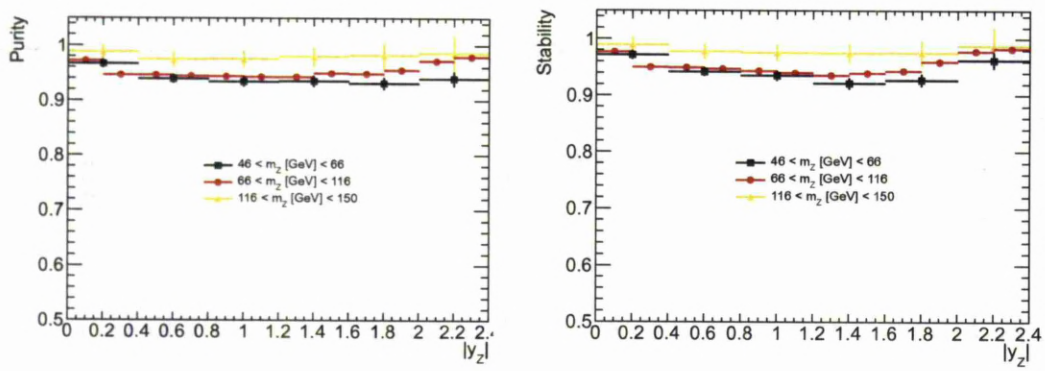

Figure 9.1: Purity and stability of the absolute rapidity $|y_Z|$ bins, as defined for the mass regions $46 < m_{ee} < 66$, $66 < m_{ee} < 116$, $116 < m_{ee} < 150$ GeV.

9.2.2 Statistical Uncertainty on the Correction Factor

The correction factor C_Z, defined in Equation 9.2 is calculated from the MC, and affected by a limited statistics of the sample used. The associated statistical uncertainty on the correction factor is estimated, using the binomial error approximation:

$$(\delta C_Z)_b^2 = \frac{(1-2C_Z)(\delta N_{rec})^2 + C_Z^2(\delta N_gen)^2}{N_{gen}^2}, \tag{9.8}$$

where $N = \sum_i w_i$ is the sum of events weights, and $(\delta N)^2 = \sum_i w_i^2$ is the corresponding uncertainty squared. When the unweighted case is considered, then $(\delta N)^2 = N$, and the Equation 9.8 can be rewritten as: $(\delta C_Z)^2 = \frac{C_Z(1-C_Z)}{N_{gen}}$. It is worth mentioning, that the proposed binomial estimate for the C_Z error is reasonable for the values far from the limits, i.e. $C_Z \neq 0, 1$. This is true in a considered case.

9.3 Fiducial Cross Section Measurement

9.3.1 Systematic Uncertainties

In this section the systematic uncertainties for the fiducial Z boson cross section measurement are presented. Since treatment of the systematic effects related to the modeling of the background to $Z/\gamma^* \rightarrow e^+e^-$ channel was discussed in Chapter 8, the reasoning will not be repeated here but only relevant results quoted.

The methodology of the uncertainty estimation assumes calculation of the nominal fiducial cross section value σ_Z^{fid} (according to Equation 9.1), which depends on various correction factors applied. Each correction factor used carries related uncertainties, which influence the cross section calculation. Then subsequently all parameters in question are varied within a given error limits to construct $\sigma_Z^{fid,up}$ and $\sigma_Z^{fid,down}$, allowing to determine the uncertainty on the cross section, via:

$$\delta\sigma_Z^{fid} = \frac{\sigma_Z^{fid,up} - \sigma_Z^{fid,down}}{2\sigma_Z^{fid}} \tag{9.9}$$

The sources of systematic uncertainties considered in this measurement are briefly discussed in this section.

- ***Trigger Efficiency***

  For details concerning electron trigger efficiency measurements, please refer to Chapter 5. For the purpose of this analysis a di-electron trigger was used. The corresponding scale factors, calculated in a two dimensional bins of η and p_T of the electron, are provided with statistical and systematic uncertainties, and are applied to each electron depending on its respective $\eta - p_T$ phase space. The effect on the cross-section measurement is small, typically below 0.16% for the central mass region.

- ***Reconstruction and Identification Efficiency***

  For details concerning electron reconstruction and identification efficiency measurements, please refer to Section 4.3. Both reconstruction and identification efficiency scale factors are calculated in two dimensional bins of η and p_T, and provided with statistical and systematical uncertainties, similarly to the trigger efficiency SF. The effect on the cross-section measurement is small, below 0.3% for the central mass region, except for the last rapidity bin.

- ***Charge Misidentification***

  For details concerning electron charge identification efficiency measurements, please refer to Section 4.5. The charge misidentification probability is well described in the MC, except for the forward region of $2.3 < |\eta| < 2.47$. The uncertainty on the charge misidentification SF increases with η. The effect on the cross-section measurement for the central mass region is dominant and reaches 0.8% for the last rapidity bin.

- ***Energy Scale and Resolution***

  For details concerning energy scale and resolution measurements, please refer to Section 4.4. The energy scale uncertainties are decomposed into several components: method uncertainty, choice of generator uncertainty, presampler scale uncertainty, material uncertainty and low p_T ($p_T < 20GeV$) uncertainty. The effect of the energy scale on the cross-section measurement is below 0.2% for the central mass region, while the contribution from energy resolution is below 0.1%.

The differences in cross section measurement arising from the choice of the Monte Carlo generator used (matrix element), are evaluated as a difference between the result obtained with MC@NLO and POWHEGHERWIG generators. Similarly, uncertainty related to the choice of parton shower modelling program

is evaluated by performing the calculations with POWHEGHERWIG instead of POWHEGPYTHIA6 and assigning the deviation as an uncertainty. The matrix element and the parton shower related uncertainties are taken from the *egamma* work [1].

The relative systematic uncertainties on the fiducial cross section measurement are summarised in Table 9.1, Table 9.2 and Table 9.3, for $46 < m_Z < 66$, $66 < m_Z < 116$ and $66 < m_Z < 116$ range, as well as represented graphically in Figure 9.2, Figure 9.3 and Figure 9.4.

Impact on the measurement precision for the low mass bin comes equally from the available statistics, as well as the systematics of the correction factors, and the multi-jet QCD background estimation. The center mass region suffers predominately from the electron charge misidentification corrections, as well as from the reconstruction, energy scale and trigger efficiency corrections. The high mass window suffers from statistical uncertainty, prominently from multi-jet background estimation, in particular towards high $|y_Z|$ bins.

	$0.00-0.40$	$0.40-0.80$	$0.80-1.20$	$1.20-1.60$	$1.60-2.00$	$2.00-2.40$
Trigger efficiency	0.249	0.225	0.265	0.277	0.365	0.502
Recon. efficiency	0.789	0.542	0.531	0.535	0.635	0.645
ID efficiency	0.281	0.243	0.258	0.227	0.307	0.416
Charge mis-ID	0.092	0.104	0.204	0.501	0.521	0.695
Electron resolution	0.100	0.237	0.087	0.403	0.571	0.128
Electron scale	0.581	0.671	0.663	0.856	0.813	0.691
$EW + t\bar{t}$ (syst.)	0.320	0.310	0.300	0.280	0.250	0.260
Multi-jet (syst.)	0.640	0.720	0.940	1.150	1.010	0.620
$EW + t\bar{t}$ (stat.)	0.510	0.540	0.660	0.730	0.820	0.970
Multi-jet (stat.)	0.410	0.440	0.600	0.780	1.050	1.570
Tot. Stat. Uncertainty (incl. corrections)	1.228	1.261	1.573	1.810	2.145	2.753
Matrix element[1]	0.173	0.173	0.173	0.173	0.173	0.173
PS and hadronization[1]	0.356	0.356	0.356	0.356	0.356	0.356
Tot. Syst. Uncertainty	1.338	1.301	1.428	1.766	1.769	1.558

Table 9.1: Summary of the uncertainties on the differential fiducial cross section measurement. Relative errors on σ_Z^{fid} for $46 < m_Z < 66$ GeV shown in per cent.

	0.00 − 0.20	0.20 − 0.40	0.40 − 0.60	0.60 − 0.80	0.80 − 1.00	1.00 − 1.20	1.20 − 1.40	1.40 − 1.60	1.60 − 1.80	1.80 − 2.00	2.00 − 2.20	2.20 − 2.40
Trigger efficiency	0.122	0.129	0.122	0.151	0.146	0.143	0.075	0.078	0.083	0.103	0.126	0.157
Recon. efficiency	0.218	0.193	0.285	0.289	0.211	0.242	0.315	0.246	0.220	0.265	0.288	0.432
ID efficiency	0.109	0.106	0.097	0.071	0.090	0.117	0.113	0.103	0.117	0.233	0.261	0.312
Charge mis-ID	0.139	0.162	0.237	0.234	0.292	0.341	0.335	0.435	0.612	0.573	0.661	0.805
Electron resolution	0.005	0.034	0.084	0.009	0.057	0.019	0.038	0.035	0.053	0.026	0.028	0.096
Electron scale	0.110	0.174	0.193	0.196	0.180	0.146	0.158	0.166	0.112	0.043	0.137	0.072
$EW + t\bar{t}$ (syst.)	0.020	0.020	0.020	0.020	0.020	0.010	0.010	0.010	0.010	0.010	0.010	0.010
Multi-jet (syst.)	0.050	0.050	0.050	0.050	0.050	0.050	0.050	0.050	0.050	0.040	0.030	0.030
$EW + t\bar{t}$ (stat.)	0.010	0.020	0.020	0.020	0.040	0.060	0.020	0.010	0.020	0.030	0.030	0.040
Multi-jet (stat.)	0.030	0.030	0.030	0.030	0.040	0.040	0.050	0.050	0.070	0.100	0.110	0.250
Tot. Stat. Uncertainty (incl. corrections)	0.238	0.242	0.253	0.263	0.279	0.288	0.310	0.324	0.383	0.459	0.498	0.751
Matrix element[1]	0.156	0.156	0.156	0.156	0.156	0.156	0.156	0.156	0.156	0.156	0.156	0.156
PS and hadronization[1]	0.171	0.171	0.171	0.171	0.171	0.171	0.171	0.171	0.171	0.171	0.171	0.171
Tot. Syst. Uncertainty	0.402	0.423	0.512	0.511	0.502	0.535	0.559	0.592	0.718	0.722	0.823	1.013

Table 9.2: Summary of the uncertainties on the differential fiducial cross section measurement. Relative errors on σ_Z^{fid} for $66 < m_Z < 116$ GeV shown in per cent.

	$0.00-0.40$	$0.40-0.80$	$0.80-1.20$	$1.20-1.60$	$1.60-2.00$	$2.00-2.40$
Trigger efficiency	0.118	0.145	0.136	0.223	0.279	0.493
Recon. efficiency	0.167	0.140	0.187	0.176	0.256	0.381
ID efficiency	0.168	0.271	0.236	0.342	0.613	0.561
Charge mis-ID	0.159	0.332	0.299	0.448	0.581	0.645
Electron resolution	0.234	0.193	0.205	0.515	1.263	1.134
Electron scale	0.358	0.417	0.694	1.071	0.832	2.106
$EW + t\bar{t}$ (syst.)	0.630	0.600	0.400	0.270	0.170	0.080
Multi-jet (syst.)	0.820	0.940	0.710	0.500	0.400	0.190
$EW + t\bar{t}$ (stat.)	0.350	0.420	0.380	0.410	0.770	0.280
Multi-jet (stat.)	0.420	0.480	0.600	0.780	1.470	2.890
Tot. Stat. Uncertainty (incl. corrections)	1.795	1.941	2.185	2.011	3.536	5.472
Matrix element[1]	0.382	0.382	0.382	0.382	0.382	0.382
PS and hadronization[1]	0.359	0.359	0.359	0.359	0.359	0.359
Tot. Syst. Uncertainty	1.274	1.398	1.289	1.552	1.899	2.675

Table 9.3: Summary of the uncertainties on the differential fiducial cross section measurement. Relative errors on σ_Z^{fid} for $116 < m_Z < 150$ GeV shown in per cent.

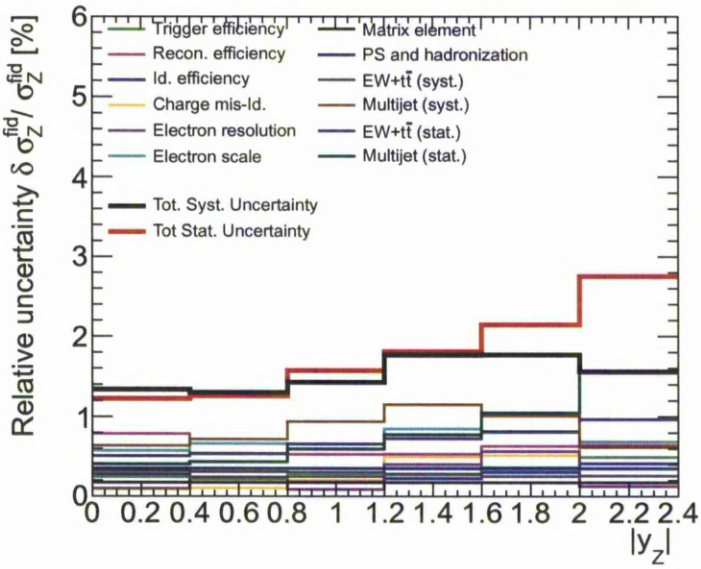

Figure 9.2: Summary of the systematic uncertainties on the fiducial cross section measurement. Shown are the relative uncertainties in per cent for the mass region $46 < m_Z < 66$.

9.3.2 Fiducial Cross Section Results

Normalised differential fiducial cross sections in the $Z/\gamma^* \to e^+e^-$ channel are shown in Figure 9.7 for the different Z boson mass ranges. Comparison between different Monte Carlo generators (PowhegPythia6, PowhegHerwig and Mc@Nlo), using the same PDF set $CT10$, show small dependance on the choice of the model implemented by a given generator, predominantly in the high and low mass intervals.

The differential fiducial cross sections in the $Z/\gamma^* \to e^+e^-$ channel are shown in Figure 9.6 for the different Z boson mass ranges. The blue band accounts for the full experimental uncertainty, including 1.8% from the luminosity measurement. The result is compared with most recent predictions derived by the MSTW, ABM, HERAPDF, NNPDF and WZ2010 groups, where available. Measured y_Z dependencies are broadly described by the predictions of the PDF

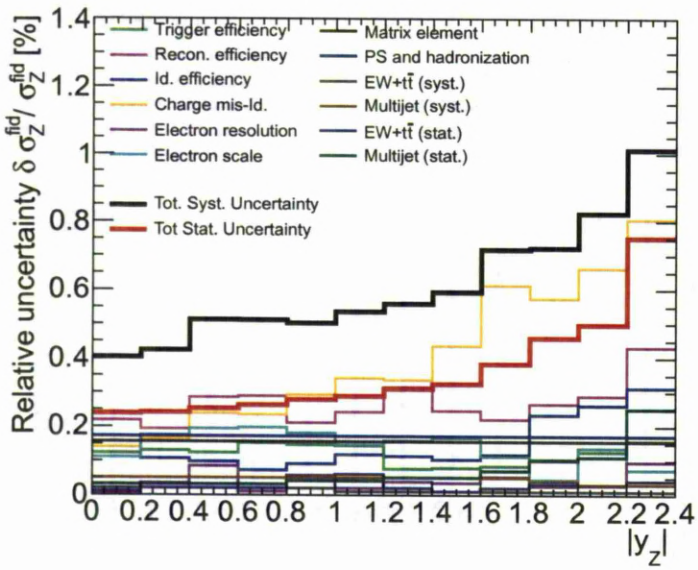

Figure 9.3: Summary of the systematic uncertainties on the fiducial cross section measurement. Shown are the relative uncertainties in per cent for the mass region $66 < m_Z < 116$.

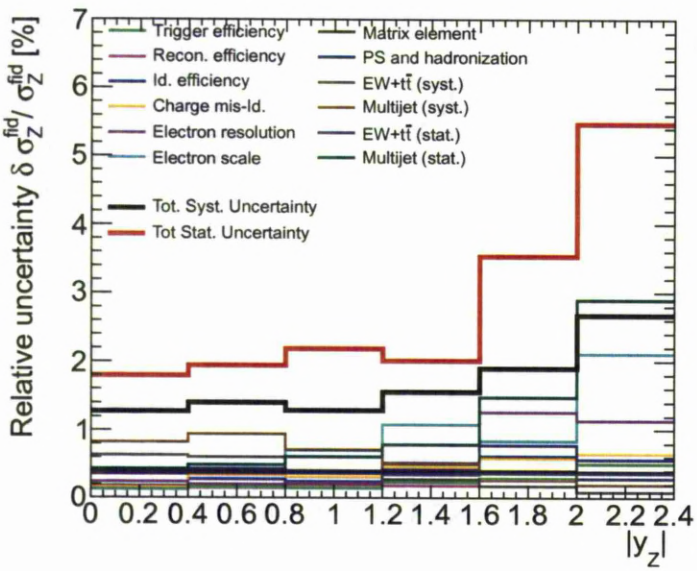

Figure 9.4: Summary of the systematic uncertainties on the fiducial cross section measurement. Shown are the relative uncertainties in per cent for the mass region $116 < m_Z < 150$.

	N^{sig}	$N^{bkg} \pm \delta N^{bkg}$	$C_Z \pm \delta C_Z$
$46 < \|y_Z\| < 66$	36364	4636.8 ± 136.8	0.564 ± 0.002
$66 < \|y_Z\| < 116$	1152247	5756.2 ± 175.5	0.605 ± 0.0004
$116 < \|y_Z\| < 150$	13145	1124.4 ± 81.0	0.602 ± 0.003

Table 9.4: Parameters for the integrated fiducial cross section measurement. N^{sig} is the number of Z/γ^* candidate events observed in data, N^{bkg} is the number of estimated background events and C_Z is the efficiency corrector factor.

	N^{sig}	$N^{bck} \pm \delta N^{bck}$	$C_Z \pm \delta C_Z$
$0.0< \|y_Z\| <0.4$	9517	1127.0 ± 62.4	0.618 ± 0.004
$0.4< \|y_Z\| <0.8$	8857	1093.5 ± 61.6	0.613 ± 0.004
$0.8< \|y_Z\| <1.2$	6618	928.3 ± 58.8	0.591 ± 0.005
$1.2< \|y_Z\| <1.6$	5061	744.2 ± 54.0	0.527 ± 0.005
$1.6< \|y_Z\| <2.0$	3749	485.9 ± 49.9	0.485 ± 0.005
$2.0< \|y_Z\| <2.4$	2502	255.8 ± 46.3	0.430 ± 0.005

Table 9.5: Parameters for the differential fiducial cross section in $46 < m_Z < 66$ GeV range. N^{sig} is the number of Z/γ^* candidate events observed in data, N^{bkg} is the number of estimated background events and C_Z is the efficiency corrector factor.

sets examined. Small excess observed in the bin by bin comparison, notably for the central rapidity bin, do not exceed overall differences between the theory values, with $ABM11$ being most compatible with the data.

Parameters used for the $Z/\gamma^* \to e^+e^-$ cross-section measurement are listed in Table 9.4. The parameters for the differential fiducial cross section measurements are listed in Table 9.5, Table 9.6 and Table 9.7, for the Z mass bin $46 < m_Z < 66$, $66 < m_Z < 116$ and $116 < m_Z < 150$, respectively. The fiducial cross section values are included in Table 9.9, Table 9.10, Table 9.11 for the differential measurement and in Table 9.8 for the integrated measurement.

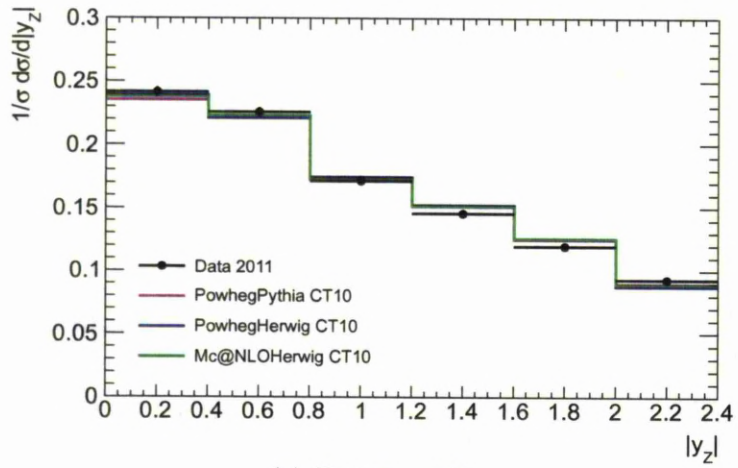

(a) $46 < m_Z < 66$

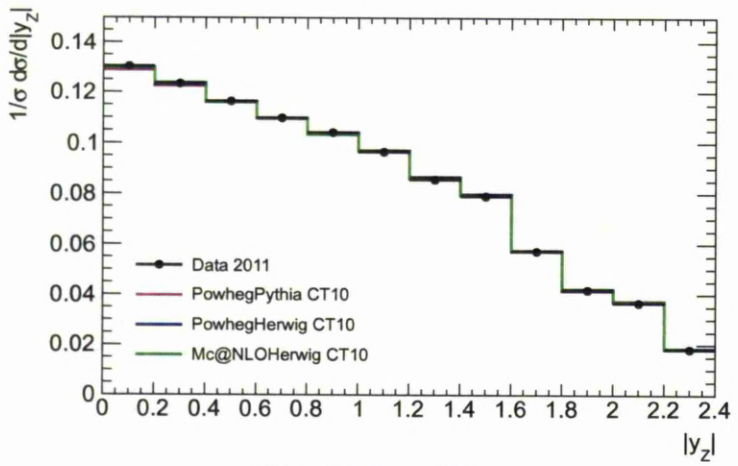

(b) $66 < m_Z < 116$

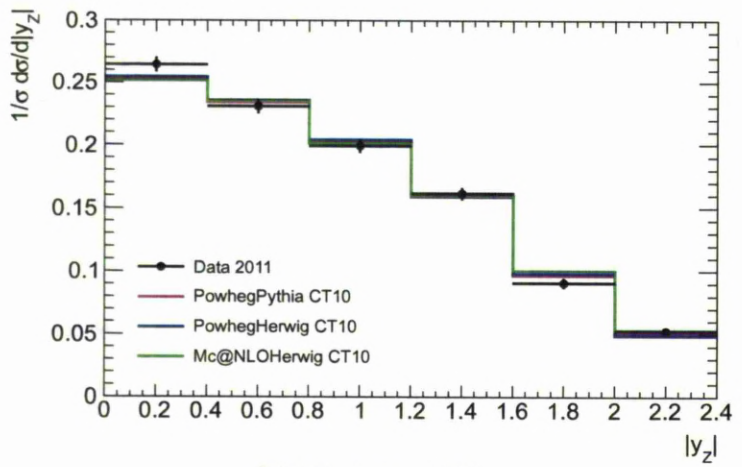

(c) $116 < m_Z < 150$

Figure 9.5: Normalised differential $Z/\gamma^* \rightarrow e^+e^-$ cross-section as a function of $|y_Z|$ in the Z boson mass ranges. Error bars represent statistical uncertainty.

	N^{sig}	$N^{bck} \pm \delta N^{bck}$	$C_Z \pm \delta C_Z$
0.0< $\|y_Z\|$ <0.2	158764	858.1 ± 47.7	0.640 ± 0.001
0.2< $\|y_Z\|$ <0.4	151190	836.3 ± 50.1	0.643 ± 0.001
0.4< $\|y_Z\|$ <0.6	141196	735.8 ± 47.5	0.637 ± 0.001
0.6< $\|y_Z\|$ <0.8	131466	740.8 ± 49.6	0.628 ± 0.001
0.8< $\|y_Z\|$ <1.0	121088	672.3 ± 50.6	0.610 ± 0.001
1.0< $\|y_Z\|$ <1.2	108333	500.2 ± 46.1	0.590 ± 0.001
1.2< $\|y_Z\|$ <1.4	94211	435.7 ± 46.1	0.578 ± 0.001
1.4< $\|y_Z\|$ <1.6	85679	337.7 ± 44.3	0.570 ± 0.001
1.6< $\|y_Z\|$ <1.8	60760	269.1 ± 45.1	0.557 ± 0.001
1.8< $\|y_Z\|$ <2.0	43948	181.4 ± 44.7	0.552 ± 0.002
2.0< $\|y_Z\|$ <2.2	37870	130.3 ± 44.0	0.542 ± 0.002
2.2< $\|y_Z\|$ <2.4	16760	56.8 ± 43.0	0.487 ± 0.002

Table 9.6: Parameters for the differential fiducial cross section in $66 < m_Z < 116$ GeV range. N^{sig} is the number of Z/γ^* candidate events observed in data, N^{bkg} is the number of estimated background events and C_Z is the efficiency corrector factor.

	N^{sig}	$N^{bck} \pm \delta N^{bck}$	$C_Z \pm \delta C_Z$
0.0< $\|y_Z\|$ <0.4	3709	385.4 ± 20.2	0.630 ± 0.007
0.4< $\|y_Z\|$ <0.8	3228	356.7 ± 20.8	0.623 ± 0.008
0.8< $\|y_Z\|$ <1.2	2594	203.0 ± 18.5	0.602 ± 0.008
1.2< $\|y_Z\|$ <1.6	2009	112.3 ± 16.8	0.588 ± 0.009
1.6< $\|y_Z\|$ <2.0	1058	56.8 ± 17.6	0.553 ± 0.011
2.0< $\|y_Z\|$ <2.4	539	10.2 ± 15.7	0.506 ± 0.014

Table 9.7: Parameters for the differential fiducial cross section in $116 < m_Z < 150$ GeV range. N^{sig} is the number of Z/γ^* candidate events observed in data, N^{bkg} is the number of estimated background events and C_Z is the efficiency corrector factor.

$46 < \|m_Z\| < 66$	$12.120 \pm 0.197_{(stat)} \pm 0.179_{(syst)} \pm 0.218_{(lum)}[pb]$
$66 < \|m_Z\| < 116$	$408.628 \pm 1.230_{(stat)} \pm 2.201_{(syst)} \pm 7.355_{(lum)}[pb]$
$116 < \|m_Z\| < 150$	$4.304 \pm 0.099_{(stat)} \pm 0.064_{(syst)} \pm 0.077_{(lum)}[pb]$

Table 9.8: Fiducial cross section integrated over $|y_Z|$.

0.0< $\|y_Z\|$ <0.4	$3.656 \pm 0.045_{(stat)} \pm 0.049_{(syst)} \pm 0.066_{(lum)}$ [pb]
0.4< $\|y_Z\|$ <0.8	$3.414 \pm 0.043_{(stat)} \pm 0.044_{(syst)} \pm 0.061_{(lum)}$ [pb]
0.8< $\|y_Z\|$ <1.2	$2.594 \pm 0.041_{(stat)} \pm 0.037_{(syst)} \pm 0.047_{(lum)}$ [pb]
1.2< $\|y_Z\|$ <1.6	$2.205 \pm 0.040_{(stat)} \pm 0.039_{(syst)} \pm 0.040_{(lum)}$ [pb]
1.6< $\|y_Z\|$ <2.0	$1.812 \pm 0.039_{(stat)} \pm 0.032_{(syst)} \pm 0.033_{(lum)}$ [pb]
2.0< $\|y_Z\|$ <2.4	$1.408 \pm 0.039_{(stat)} \pm 0.022_{(syst)} \pm 0.025_{(lum)}$ [pb]

Table 9.9: Fiducial cross section for $46 < m_Z < 66$ GeV range.

0.0< $\|y_Z\|$ <0.2	$132.955 \pm 0.317_{(stat)} \pm 0.535_{(syst)} \pm 2.393_{(lum)}$ [pb]
0.2< $\|y_Z\|$ <0.4	$125.939 \pm 0.304_{(stat)} \pm 0.533_{(syst)} \pm 2.267_{(lum)}$ [pb]
0.4< $\|y_Z\|$ <0.6	$118.774 \pm 0.300_{(stat)} \pm 0.609_{(syst)} \pm 2.138_{(lum)}$ [pb]
0.6< $\|y_Z\|$ <0.8	$112.099 \pm 0.295_{(stat)} \pm 0.573_{(syst)} \pm 2.018_{(lum)}$ [pb]
0.8< $\|y_Z\|$ <1.0	$106.279 \pm 0.296_{(stat)} \pm 0.533_{(syst)} \pm 1.913_{(lum)}$ [pb]
1.0< $\|y_Z\|$ <1.2	$98.532 \pm 0.284_{(stat)} \pm 0.528_{(syst)} \pm 1.774_{(lum)}$ [pb]
1.2< $\|y_Z\|$ <1.4	$87.376 \pm 0.271_{(stat)} \pm 0.489_{(syst)} \pm 1.573_{(lum)}$ [pb]
1.4< $\|y_Z\|$ <1.6	$80.662 \pm 0.262_{(stat)} \pm 0.478_{(syst)} \pm 1.452_{(lum)}$ [pb]
1.6< $\|y_Z\|$ <1.8	$58.465 \pm 0.224_{(stat)} \pm 0.420_{(syst)} \pm 1.052_{(lum)}$ [pb]
1.8< $\|y_Z\|$ <2.0	$42.731 \pm 0.196_{(stat)} \pm 0.309_{(syst)} \pm 0.769_{(lum)}$ [pb]
2.0< $\|y_Z\|$ <2.2	$37.488 \pm 0.187_{(stat)} \pm 0.309_{(syst)} \pm 0.675_{(lum)}$ [pb]
2.2< $\|y_Z\|$ <2.4	$18.497 \pm 0.139_{(stat)} \pm 0.187_{(syst)} \pm 0.333_{(lum)}$ [pb]

Table 9.10: Fiducial cross section for $66 < m_Z < 116$ GeV range.

0.0< $\|y_Z\|$ <0.4	$1.421 \pm 0.026_{(stat)} \pm 0.018_{(syst)} \pm 0.026_{(lum)}$ [pb]
0.4< $\|y_Z\|$ <0.8	$1.241 \pm 0.024_{(stat)} \pm 0.017_{(syst)} \pm 0.022_{(lum)}$ [pb]
0.8< $\|y_Z\|$ <1.2	$1.070 \pm 0.023_{(stat)} \pm 0.014_{(syst)} \pm 0.019_{(lum)}$ [pb]
1.2< $\|y_Z\|$ <1.6	$0.869 \pm 0.017_{(stat)} \pm 0.013_{(syst)} \pm 0.016_{(lum)}$ [pb]
1.6< $\|y_Z\|$ <2.0	$0.488 \pm 0.017_{(stat)} \pm 0.009_{(syst)} \pm 0.009_{(lum)}$ [pb]
2.0< $\|y_Z\|$ <2.4	$0.281 \pm 0.015_{(stat)} \pm 0.008_{(syst)} \pm 0.005_{(lum)}$ [pb]

Table 9.11: Fiducial cross section for $116 < m_Z < 150$ GeV range.

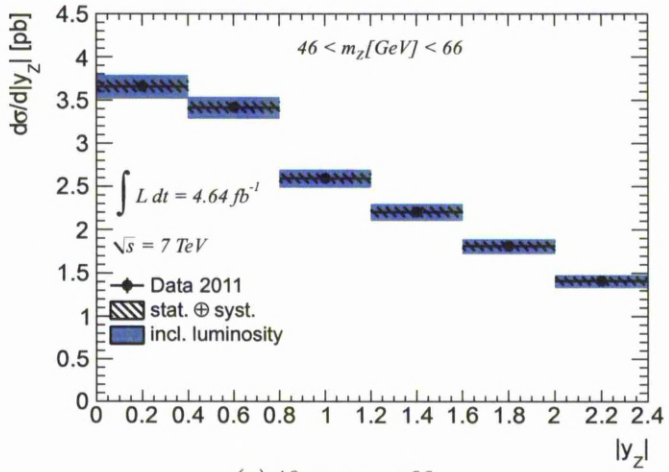

(a) $46 < m_Z < 66$

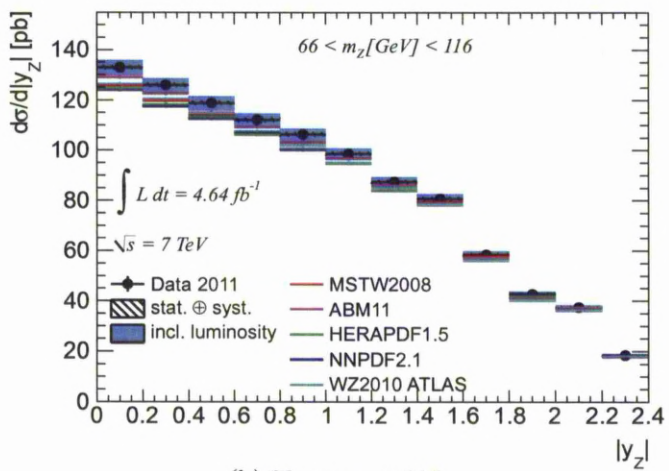

(b) $66 < m_Z < 116$

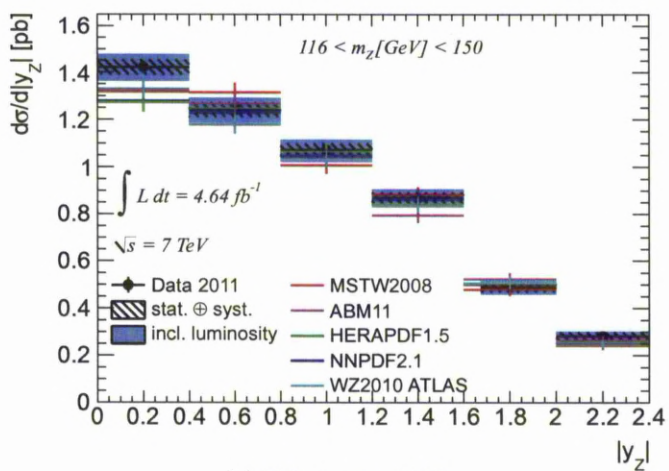

(c) $116 < m_Z < 150$

Figure 9.6: Differential fiducial $Z/\gamma^* \to e^+e^-$ cross-section as a function of $|y_Z|$ in the Z boson mass ranges.

9.3.3 Common Fiducial Cross Section

The experimental fiducial cross section measurements can be extrapolated to the common phase space (Equation 9.3). As an exercise this procedure was performed, allowing comparison to various theoretical predictions calculated to NLO and NNLO QCD using the programs FEWZ[103], [104] and DYNNLO [105]. The theoretical predictions are taken from the *egamma* group [1].

The common fiducial cross sections have been calculated at NNLO QCD using the NNLO PDF sets: CT10 [23], ABM11 [24], HERAPDF 1.5 [25], MSTW2008 [26], NNPDF2.3 [27] and JR09 [28].

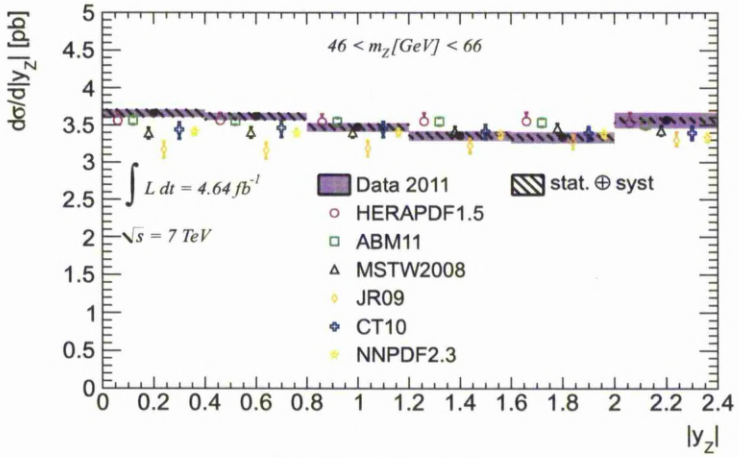

(a) $46 < m_Z < 66$

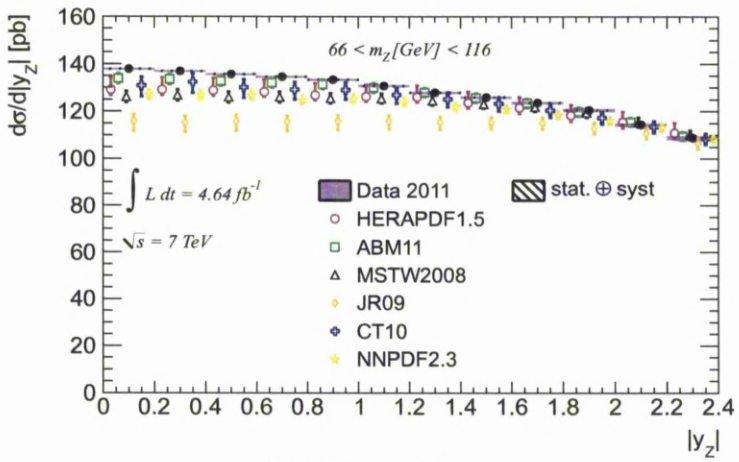

(b) $66 < m_Z < 116$

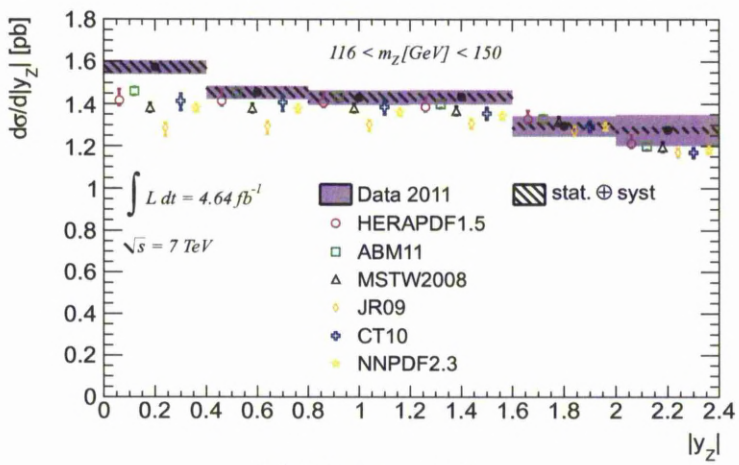

(c) $116 < m_Z < 150$

Figure 9.7: Differential common fiducial $Z/\gamma^* \to e^+e^-$ cross-section as a function of $|y_Z|$ in the Z boson mass ranges.

Chapter 10

Summary

This thesis presents a study of the 2011 LHC data at centre-of-mass energy of $7TeV$, recorded by the ATLAS Detector, on inclusive Z/γ^* production cross section. The data set corresponds to an integrated luminosity of $4.64fb^{-1}$. The measurements have been performed in the electron decay channel. This analysis has been pursued as a complementary cross-check to the newest ATLAS results [1], however the event selection method include different criteria. The electron trigger, identification and reconstruction in the ATLAS Detector is presented, and the data driven method, central for the estimate of the measurement efficiencies is exemplified by the electron trigger efficiency evaluation. A special attention was given to understand the background contribution from QCD sources, and the shape of the QCD background was studied using a data-driven technique. Several sources of the cross section systematic uncertainties were studied, including effects of electron performance measurements and background determination methods. The cross section in the fiducial region of the experiment is presented differentially as a function of the Z/γ^* boson rapidity, and integrated over $|y_Z|$, in three boson mass ranges: $46 < m_Z < 66$, $66 < m_Z < 116$ and $66 < m_Z < 116$ $[GeV]$.

Appendix A

Appendix

A.1 χ^2 p-value

Comparison of compatibility between two distributions is frequently used technique in data analysis. First suggested by Pearson [100] the χ^2 test of homogeneity is used widely for comparing histograms. To compare histograms with the same binning and the number of bins, r, we denote events in the $i-th$ bin in the first histogram as n_i and as m_i in the second one. The total number of events in the first histogram is $N = \sum_{i=1}^{r} n_i$ and in similarly second $M = \sum_{i=1}^{r} m_i$. The hypothesis of identity (homogeneity) [102] is that the two histograms represent random values with identical distributions. It is equivalent that there exist r constants $p1, ..., pr$, such that $\sum_{i=1}^{r} p_i = 1$. What follows the probability of belonging to $i-th$ bin for a measured value is the same for both distributions. Since the number of events in the $i-th$ bin is a random variable with a distribution approximated by a Poisson probability distribution $\frac{e^{-Np_i}(Np_i)^{n_i}}{n_i!}$ for the first and likewise $\frac{e^{-Mp_i}(Mp_i)^{m_i}}{m_i!}$ for the second distribution. If the hypothesis of homogeneity is valid, then the maximum likelihood estimator of p_i, $i = 1, ..., r$ is

$$\hat{p}_i = \frac{n_i + m_i}{N + M} \tag{A.1}$$

As a result

$$\chi^2 = \sum_{i=1}^{r} \frac{(n_i - N\hat{p}_i)^2}{N\hat{p}_i} + \sum_{i=1}^{r} \frac{(m_i - M\hat{p}_i)^2}{M\hat{p}_i} = \frac{1}{MN} \sum_{i=1}^{r} \frac{(Mn_i - Nm_i)^2}{n_i + m_i} \tag{A.2}$$

will approximate χ^2_{r-1} distribution [102].

Bibliography

[1] K Bachas et al. Measurement and qcd analysis of differential inclusive $w^{\pm} \to l\nu$ and $z/gamma^* \to ll$ production and leptonic decay cross sections with atlas: Analysis stdm-2012-20: W and z inclusive cross section with 2011 data. Technical Report ATL-COM-PHYS-2013-217, CERN, Geneva, Feb 2012.

[2] Georges Aad et al. Measurement of the inclusive $W^{\pm}$ and Z/gamma cross sections in the electron and muon decay channels in pp collisions at $\sqrt{s} = 7$ TeV with the ATLAS detector. *Phys.Rev.*, D85:072004, 2012.

[3] M Aharrouche et al. Total and differential $W \to \ell\nu$ and $Z \to \ell\ell$ cross-sections measurements in proton-proton collisions at $\sqrt{s} = 7$ tev with the atlas detector. Technical Report ATL-COM-PHYS-2011-751, CERN, Geneva, Jun 2011.

[4] Serguei Chatrchyan et al. Measurement of the Inclusive W and Z Production Cross Sections in pp Collisions at $\sqrt{s} = 7$ TeV. *JHEP*, 1110:132, 2011.

[5] Measurement of the differential and double-differential drell-yan cross section in proton-proton collisions at 7 tev. Technical Report CMS-PAS-EWK-11-007, CERN, Geneva, 2012.

[6] R Aaij et al. Measurement of the cross-section for $Z \to e^+e^-$ production in pp collisions at $\sqrt{s} = 7$ TeV. *JHEP*, 1302:106, 2013.

[7] M. Gell-Mann. A schematic model of baryons and mesons. *Phys. Lett.*, 8:214–215, 1964.

[8] D.J. Gross and Frank Wilczek. Asymptotically Free Gauge Theories. 1. *Phys.Rev.*, D8:3633–3652, 1973.

[9] S. L. Glashow. Partial symmetries of weak interactions. *Nucl. Phys.*, 22:579–588, 1961.

[10] Abdus Salam. Weak and Electromagnetic Interactions. *Conf.Proc.*, C680519:367–377, 1968.

[11] S. Weinberg. A model of leptons. *Phys. Rev. Lett.*, 19:1264–1266, 1967.

[12] Peter W. Higgs. Broken symmetries, massless particles and gauge fields. *Phys.Lett.*, 12:132–133, 1964.

[13] F. Englert and R. Brout. Broken Symmetry and the Mass of Gauge Vector Mesons. *Phys.Rev.Lett.*, 13:321–323, 1964.

[14] G.S. Guralnik, C.R. Hagen, and T.W.B. Kibble. Global Conservation Laws and Massless Particles. *Phys.Rev.Lett.*, 13:585–587, 1964.

[15] Georges Aad et al. Observation of a new particle in the search for the Standard Model Higgs boson with the ATLAS detector at the LHC. *Phys.Lett.*, B716:1–29, 2012.

[16] Serguei Chatrchyan et al. Observation of a new boson at a mass of 125 GeV with the CMS experiment at the LHC. *Phys.Lett.*, B716:30–61, 2012.

[17] CERN Press Release. New results indicate that particle discovered at cern is a higgs boson. `http://press.web.cern.ch/press-releases/2013/03/`

new-results-indicate-particle-discovered-cern-higgs-boson., 14 March 2013.

[18] Richard P. Feynman. Very high-energy collisions of hadrons. *Phys. Rev. Lett.*, 23:1415–1417, Dec 1969.

[19] Martin Breidenbach, Jerome I. Friedman, Henry W. Kendall, Elliott D. Bloom, D.H. Coward, et al. Observed Behavior of Highly Inelastic electron-Proton Scattering. *Phys.Rev.Lett.*, 23:935–939, 1969.

[20] Elliott D. Bloom, D.H. Coward, H.C. DeStaebler, J. Drees, Guthrie Miller, et al. High-Energy Inelastic e p Scattering at 6-Degrees and 10-Degrees. *Phys.Rev.Lett.*, 23:930–934, 1969.

[21] W.J. Stirling J.M. Campbell, J.W. Huston. Title: Hard Interactions of Quarks and Gluons: a Primer for LHC Physics.

[22] G. Altarelli and G. Parisi. Asymptotic freedom in parton language. *Nucl. Phys. B*, 126:298, 1977.

[23] Hung-Liang Lai, Marco Guzzi, Joey Huston, Zhao Li, Pavel M. Nadolsky, et al. New parton distributions for collider physics. *Phys.Rev.*, D82:074024, 2010.

[24] S. Alekhin, J. Blumlein, and S. Moch. Parton Distribution Functions and Benchmark Cross Sections at NNLO. *Phys.Rev.*, D86:054009, 2012.

[25] F.D. Aaron et al. Combined Measurement and QCD Analysis of the Inclusive e+- p Scattering Cross Sections at HERA. *JHEP*, 1001:109, 2010.

[26] A.D. Martin, W.J. Stirling, R.S. Thorne, and G. Watt. Parton distributions for the LHC. *Eur.Phys.J.*, C63:189–285, 2009.

[27] Richard D. Ball, Valerio Bertone, Stefano Carrazza, Christopher S. Deans, Luigi Del Debbio, et al. Parton distributions with LHC data. *Nucl.Phys.*, B867:244–289, 2013.

[28] P. Jimenez-Delgado and E. Reya. Dynamical NNLO parton distributions. *Phys.Rev.*, D79:074023, 2009.

[29] M Aharrouche, A Arbuzov, D Bardin, M Bendel, S Bondarenko, A Cooper-Sarkar, F Ellinghaus, M Flowerdew, S Glazov, C Goeringer, J Haller, C Handel, G Hoerentrup, L Kalinovskaya, M Karnevskiy, M Klein, U Klein, T Kluge, K Koeneke, S Koenig, V Kolesnikov, J Kretzschmar, S Mahmoud, S Migas, A Nikiforov, D Petschull, R Placakyte, V Radescu, R Sadykov, A Sapronov, G Siragusa, S Tapprogge, J Vossebeld, S Wollstadt, and B Wrona. Double differential z,w cross sections and their ratios in the electron channels. Technical Report ATL-COM-PHYS-2010-325, CERN, Geneva, Jun 2010.

[30] S. D. Drell and Tung-Mow Yan. Massive Lepton Pair Production in Hadron-Hadron Collisions at High-Energies. *Phys. Rev. Lett.*, 25:316–320, 1970.

[31] G. Altarelli, R. Keith Ellis, and G. Martinelli. Large Perturbative Corrections to the Drell-Yan Process in QCD. *Nucl. Phys.*, B157:461, 1979.

[32] J. Kubar-Andre and Frank E. Paige. Gluon corrections to the drell-yan model. *Phys. Rev. D*, 19:221–229, Jan 1979.

[33] R. Hamberg, W. L. van Neerven, and T. Matsuura. A Complete calculation of the order α_s^2 correction to the Drell-Yan K factor. *Nucl. Phys.*, B359:343–405, 1991.

[34] P. J. Rijken and W. L. van Neerven. Order α_s^2 contributions to the Drell-Yan cross- section at fixed target energies. *Phys. Rev.*, D51:44–63, 1995.

[35] W. L. van Neerven and E. B. Zijlstra. The $\mathcal{O}(\alpha_s^2)$ corrected Drell-Yan K factor in the DIS and MS scheme. *Nucl. Phys.*, B382:11–62, 1992.

[36] Charalampos Anastasiou, Lance J. Dixon, Kirill Melnikov, and Frank Petriello. High precision QCD at hadron colliders: Electroweak gauge boson rapidity distributions at NNLO. *Phys. Rev.*, D69:094008, 2004.

[37] W. J. Stirling R. K. Ellis and B. R. Webber. Qcd and collider physics cambridge monographs on particle physics. *Nucl.Phys. and Grav.Cosmol.*, 2003. Photography by.S. Vascotto.

[38] K. Nakamura et al. Review of particle physics. *J.Phys.*, G37:075021, 2010.

[39] Lyndon Evans and Philip Bryant. LHC Machine. *JINST*, 3:S08001, 2008.

[40] M. Benedikt, P. Collier, V. Mertens, J. Poole, and K. Schindl. LHC Design Report. 3. The LHC injector chain. 2004.

[41] Christiane Lefvre. The cern accelerator complex. complexe des acclrateurs du cern. Dec 2008.

[42] Oliver S. Bruning, P. Collier, P. Lebrun, S. Myers, R. Ostojic, et al. LHC Design Report. 1. The LHC Main Ring. 2004.

[43] S. van der Meer. Calibration of the Effective Beam Height in the ISR. 1968.

[44] G. Aad et al. Atlas public results. `https://twiki.cern.ch/twiki/bin/view/AtlasPublic/WebHome`.

[45] S. Chatrchyan et al. The CMS experiment at the CERN LHC. *JINST*, 3:S08004, 2008.

[46] K. Aamodt et al. The ALICE experiment at the CERN LHC. *JINST*, 3:S08002, 2008.

[47] Jr. Alves, A. Augusto et al. The LHCb Detector at the LHC. *JINST*, 3:S08005, 2008.

[48] G. Aad et al. The ATLAS Experiment at the CERN Large Hadron Collider. *JINST*, 3:S08003, 2008.

[49] G. Aad et al. Expected Performance of the ATLAS Experiment - Detector, Trigger and Physics. 2009.

[50] ATLAS: Detector and physics performance technical design report. Volume 1. 1999.

[51] ATLAS: Detector and physics performance technical design report. Volume 2. 1999.

[52] G. Aad, M. Ackers, F.A. Alberti, M. Aleppo, G. Alimonti, et al. ATLAS pixel detector electronics and sensors. *JINST*, 3:P07007, 2008.

[53] A. Ahmad, Z. Albrechtskirchinger, P.P. Allport, J. Alonso, L. Andricek, et al. The Silicon microstrip sensors of the ATLAS semiconductor tracker. *Nucl.Instrum.Meth.*, A578:98–118, 2007.

[54] E. Abat et al. The ATLAS Transition Radiation Tracker (TRT) proportional drift tube: Design and performance. *JINST*, 3:P02013, 2008.

[55] G. Aad et al. Readiness of the ATLAS Liquid Argon Calorimeter for LHC Collisions. *Eur.Phys.J.*, C70:723–753, 2010.

[56] G. Aad et al. Readiness of the ATLAS Tile Calorimeter for LHC collisions. *Eur.Phys.J.*, C70:1193–1236, 2010.

[57] ATLAS muon spectrometer: Technical design report. 1997.

[58] Performance of the atlas electron and photon trigger in p-p collisions at sqrts = 7 tev in 2011. Technical Report ATLAS-CONF-2012-048, CERN, Geneva, May 2012.

[59] G. Duckeck et al. ATLAS computing: Technical design report. 2005.

[60] Georges Aad et al. Electron performance measurements with the ATLAS detector using the 2010 LHC proton-proton collision data. *Eur.Phys.J.*, C72:1909, 2012.

[61] Expected electron performance in the ATLAS experiment. 2011.

[62] J Kretzschmar and L Iconomidou-Fayard. Supporting document on electron performance measurements using the 2011 lhc proton-proton collisions. Technical Report ATL-COM-PHYS-2012-1023, CERN, Geneva, Jul 2012. This is the Draft of the supporting document for the CONF note.

[63] J Kretzschmar and L Iconomidou-Fayard. Electron performances measurements using the 2011 lhc proton-proton collisions. Technical Report ATL-COM-PHYS-2012-1024, CERN, Geneva, Jul 2012. This is a draft of the CONF Note.

[64] A Collaboration. Supporting note for the 2011 em calibration analysis. Technical Report ATL-COM-PHYS-2012-1473, CERN, Geneva, Oct 2012.

[65] Egamma group. *Official electron energy scale and resolution corrections recommendation.* `https://twiki.cern.ch/twiki/bin/view/AtlasProtected/EnergyScaleResolutionRecommendations`.

[66] M. Aharrouche et al. Energy linearity and resolution of the ATLAS electromagnetic barrel calorimeter in an electron test-beam. *Nucl.Instrum.Meth.*, A568:601–623, 2006.

[67] M. Aharrouche, C. Adam-Bourdarios, M. Aleksa, D. Banfi, D. Benchekroun, et al. Measurement of the response of the ATLAS liquid argon barrel calorimeter to electrons at the 2004 combined test-beam. *Nucl.Instrum.Meth.*, A614:400–432, 2010.

[68] J. Colas, L. Di Ciaccio, M. Gouanere, R. Lafaye, S. Laplace, et al. Response Uniformity of the ATLAS Liquid Argon Electromagnetic Calorimeter. *Nucl.Instrum.Meth.*, A582:429–455, 2007.

[69] T. Skwarnicki. A study of the radiative cascade transitions between the upsilon-prime and upsilon resonances,. *DESY F31-86-02, Ph.D Thesis, Appendix E*, 1986.

[70] Egamma group. Reconstructed $z \to e^+e^-$ invariant mass after electron energy calibration. Technical Report ATL-COM-PHYS-2011-1637, CERN, Geneva, Dec 2011.

[71] Egamma group. *LAr Cleaning And Object Quality TWiki.* `https://twiki.cern.ch/twiki/bin/viewauth/AtlasProtected/LArCleaningAndObjectQuality`.

[72] Improved luminosity determination in pp collisions at $\sqrt{s} = 7$ tev using the atlas detector at the lhc. Technical Report arXiv:1302.4393. CERN-PH-EP-2013-026, CERN, Geneva, Feb 2013.

[73] Improved luminosity determination in **pp** collisions at $\sqrt{\mathbf{s}} = \mathbf{7}$ tev using the atlas detector at the lhc. Technical Report ATLAS-CONF-2012-080, CERN, Geneva, Jul 2012.

[74] Torbjorn Sjostrand. Monte Carlo Generators. pages 51–74, 2006.

[75] M.A. Dobbs, S. Frixione, Eric Laenen, K. Tollefson, H. Baer, et al. Les Houches guidebook to Monte Carlo generators for hadron collider physics. pages 411–459, 2004.

[76] Torbjorn Sjostrand, Stephen Mrenna, and Peter Z. Skands. PYTHIA 6.4 Physics and Manual. *JHEP*, 05:026, 2006. `http://projects.hepforge.org/pythia6/`.

[77] Bo Andersson, G. Gustafson, G. Ingelman, and T. Sjostrand. Parton Fragmentation and String Dynamics. *Phys.Rept.*, 97:31–145, 1983.

[78] G. Corcella et al. HERWIG 6.5: an event generator for Hadron Emission Reactions With Interfering Gluons (including supersymmetric processes). *JHEP*, 01:010, 2001.

[79] Thomas D. Gottschalk. AN IMPROVED DESCRIPTION OF HADRONIZATION IN THE QCD CLUSTER MODEL FOR e+ e- ANNIHILATION. *Nucl.Phys.*, B239:349, 1984.

[80] J. M. Butterworth, J. R. Forshaw, and M. H. Seymour. Multiparton interactions in photoproduction at HERA. *Z. Phys.*, C72:637–646, 1996. See `http://projects.hepforge.org/jimmy/`.

[81] Paolo Nason. A new method for combining NLO QCD with shower Monte Carlo algorithms. *JHEP*, 11:040, 2004.

[82] Simone Alioli, Paolo Nason, Carlo Oleari, and Emanuele Re. NLO vector-boson production matched with shower in POWHEG. *JHEP*, 07:060, 2008.

[83] Stefano Frixione, Paolo Nason, and Carlo Oleari. Matching NLO QCD computations with Parton Shower simulations: the POWHEG method. *JHEP*, 11:070, 2007.

[84] Simone Alioli, Paolo Nason, Carlo Oleari, and Emanuele Re. A general framework for implementing NLO calculations in shower Monte Carlo programs: the POWHEG BOX. *JHEP*, 06:043, 2010.

[85] Stefano Frixione and Bryan R. Webber. Matching NLO QCD computations and parton shower simulations. *JHEP*, 06:029, 2002.

[86] Piotr Golonka and Zbigniew Was. PHOTOS Monte Carlo: A Precision tool for QED corrections in Z and W decays. *Eur.Phys.J.*, C45:97–107, 2006.

[87] B. P. Kersevan and E. R. Was. Processing generated events with tauola and photos using the athena interface:. `http://atlas-sw.cern.ch/cgi-bin/viewcvs-atlas.cgi/offline/Generators/Tauola_i/doc/athena_TauolaPhotos.ps?revision=1.4`.

[88] S. Jadach, J. H. Kuhn, and Z. Was. TAUOLA: A library of Monte Carlo programs to simulate decays of polarized tau leptons. *Comput. Phys. Commun.*, 64:275–299, 1990.

[89] S. Agostinelli et al. GEANT4: A Simulation toolkit. *Nucl.Instrum.Meth.*, A506:250–303, 2003.

[90] A. Sherstnev and R.S. Thorne. Parton Distributions for LO Generators. *Eur.Phys.J.*, C55:553–575, 2008.

[91] J Butterworth, E Dobson, U Klein, B Mellado Garcia, T Nunnemann, J Qian, D Rebuzzi, and R Tanaka. Single boson and diboson production cross sections in pp collisions at sqrts=7 tev. Technical Report ATL-COM-PHYS-2010-695, CERN, Geneva, Aug 2010.

[92] S. Moch and P. Uwer. Heavy-quark pair production at two loops in QCD. *Nucl.Phys.Proc.Suppl.*, 183:75–80, 2008.

[93] U. Langenfeld, S. Moch, and P. Uwer. New results for t anti-t production at hadron colliders. 2009.

[94] Georges Aad et al. Measurement of the top quark pair production cross section in pp collisions at $\sqrt{s} = 7$ TeV in dilepton final states with ATLAS. *Phys.Lett.*, B707:459–477, 2012.

[95] Egamma group. *Extended Pileup Reweighting TWiki.* `https://twiki.cern.ch/twiki/bin/viewauth/AtlasProtected/ExtendedPileupReweighting`.

[96] ATLAS Collaboration. Measurement of the transverse momentum distribution of Z/γ^* bosons in proton-proton collisions at $\sqrt{s} = 7$ TeV with the ATLAS detector. 2011. submitted to PLB.

[97] A. Vicini M. Boonekamp et al. *Improved LO electroweak approximations for Z and W Generators.* `https://twiki.cern.ch/twiki/pub/AtlasProtected/WZElectroweakCommonTopics2011/IBA.pdf`
See also `https://indico.cern.ch/getFile.py/access?contribId=18&sessionId=2&resId=0&materialId=slides&confId=203748`
and `https://indico.cern.ch/getFile.py/access?contribId=38&sessionId=2&resId=0&materialId=slides&confId=203748`, Oct 2012.

[98] Egamma group. *Electrons Energy Direction TWiki.* `https://twiki.cern.ch/twiki/bin/viewauth/AtlasProtected/ElectronsEnergyDirection`.

[99] E. Richter-Was N. Lorenzo, D. Fournier and D. Froidevaux. *Various Reports on electron efficiency loss for* $1.65 < |\eta| < 1.70$. `http://indico.cern.ch/getFile.py/access?contribId=1&resId=0&materialId=slides&confId=205024`, 2011-2012.

[100] K. Pearson. On the theory of contingency and its relation to association and normal correlation. *Drapers' Co. Memoirs, Biometric Series No. 1, London.*, 1904.

[101] N.D. Gagunashvili. Chi-Square Tests for Comparison Weighted Histograms. *Nucl.Instrum.Meth.*, A614:287–296, 2010.

[102] H. Cramer. Mathematical methods of statistics. *Princeton University Press, Princeton.*, 1946.

[103] Ryan Gavin, Ye Li, Frank Petriello, and Seth Quackenbush. FEWZ 2.0: A code for hadronic Z production at next-to-next-to-leading order. *Comput.Phys.Commun.*, 182:2388–2403, 2011. FEWZ pre-released V2.1.

[104] Ye Li and Frank Petriello. Combining QCD and electroweak corrections to dilepton production in FEWZ. *Phys.Rev.*, D86:094034, 2012.

[105] Stefano Catani, Leandro Cieri, Giancarlo Ferrera, Daniel de Florian, and Massimiliano Grazzini. Vector boson production at hadron colliders: A Fully exclusive QCD calculation at NNLO. *PRLTA*, 103:082001, 2009. DYNNLO version 1.1.

List of Figures

List of Tables